Computational Modeling of Indentation of Thin Films and Flow Through Porous Media

A Dissertation Presented

by

Zheng Zhi

to

The Graduate School

in Partial Fulfillment of the

Requirements

for the Degree of

Doctor of Philosophy

in

Materials Science and Engineering

Stony Brook University

August 2017

Stony Brook University

The Graduate School

Zheng Zhi

We, the dissertation committee for the above candidate for the

Doctor of Philosophy degree, hereby recommend

acceptance of this dissertation.

T. A. Venkatesh – Dissertation Advisor
Associate Professor, Materials Science and Chemical Engineering

Tad Koga - Chairperson of Defense
Associate Professor, Materials Science and Chemical Engineering

Balaji Raghothamachar – Third Inside Member
Assistant Research Professor, Materials Science and Chemical Engineering

David Hwang – Outside Member
Associate Professor, Mechanical Engineering

This dissertation is accepted by the Graduate School

Charles Taber

Dean of the Graduate School

Abstract of the Dissertation

Computational Modeling of Indentation of Thin Films and Flow Through Porous Media

by

Zheng Zhi

Doctor of Philosophy

in

Materials Science and Engineering

Stony Brook University

2017

A finite element model that captures the indentation force-depth response of a thin film system that exhibits isotropic elastic behavior and transversely isotropic plastic behavior on a substrate material that exhibits isotropic elastic behavior, indented by a sharp conical indenter was developed. Using dimensional analysis and a large number of finite element simulations, the relationships between the indentation response and the fundamental elastic and plastic properties of the substrate and the thin film were captured. It is demonstrated that both the forward analysis that predicts the indentation response from known material properties and the reverse analysis that predicts the material properties from known indentation responses were captured accurately. It is also demonstrated that the substrate's elastic property could also be simultaneously obtained along with the elastic and plastic properties of the indented thin film from the indentation analysis. Under conditions where the experimental results are very reliable with small errors, and within the range of material systems investigated in this study, the indentation method is expected to provide unique, robust and reliable predictions for the elastic and plastic properties of the thin film system.

A hybrid finite element/volume model that captures the flow and pressure drop characteristics in highly porous woven matrix media is developed. It is demonstrated that the geometric characteristics of a real woven matrix comprised of circular cross-section fibers and curvature due to fiber bending is captured well with an equivalent model system comprised of fibers with square cross-section. A comprehensive study of the effects of changes in the finite element model size and defects in lay-up of the woven matrix layers on the predictions of the pressure drops was carried out. Changes in the in-plane size of the finite element model, lateral to the fluid flow direction, had relatively minor effects on the pressure drops predicted by the models. However, changes in the thickness of the finite element model in the fluid flow direction had significant effects on the pressure drops. In simulations with very thin models, the boundary effects had a greater influence on the overall flow behavior and caused the predicted pressure drops to increase proportionately. On the other hand, simulations with thick models indicated that the flows were fully developed and the boundary effects were minimized, resulting in relatively smaller pressure drops. Furthermore, defects in the lay-up of the woven matrix layers were also shown to have a significant impact on the pressure drops predicted by the simulations. Higher defect densities resulted in greater pressure drops as they disrupted the steady flow of fluid in the through-thickness direction. The pressure drops obtained in the finite element model simulations of thick models that contained some defective layers matched very well with experimental observations.

This dissertation is dedicated to my mother, my grandfather, my wife, and, who I care and who care me, of course.

Table of Contents

List of Figures

List of Tables

Acknowledgments

Graduate studying at Stony Brook University is the most special and unforgettable experiences of my life, and going to become one of the most precious wealth of my life. Here, I have met a lot of enthusiasm and talented students, knowledgeable and high-minded professors and scholars. They gave me a tremendous help in the growth of my life, thought and academic.

First, I would like to thank my advisor, Prof. T.A. Venkatesh for giving me the great chance to come into contact with the field of finite element method, and letting me to join in the program of Thermolift company. Well worth mentioning that during this period, he, with great patience and carefulness, gave me lots of guidance and encouragement.

Next, I would like to thank Dr. Guang Cheng for guiding me patiently how to use the software of ABAQUS. Without his help, it's almost impossible for me to get so many desired results in such a short period. Dr. Hongxu Liu also gave me great help in my research. From the discussions with him, I have gotten a deeper understanding of some important theories and models.

In addition, I would like to thank my partner, Hanfei Chen, a doctoral candidate, who did excellent experimental work for our fluid program.

Also, I would like to thank my roommates and classmates like, Xiongfei Wei, Lizhou Nie, Peng Li, Fengzhou He, Yuhao Fei, Yu Yang, Wenxiang Ding, Zhiqiang He and so on. I'm sorry that I cannot mention the name of each person, but I sincerely appreciate every single help from every single person, and will keep it in my mind forever.

Additionally, I would like to thank my boyhood friends. Whenever I am lost or homesick, it's their encouragement and backing made me to persevere.

Finally, I would like to thank my wife, Fei Wang and my family members for trusting and supporting me all the way.

Give my best wishes to all the people I care about above.

Chapter 1: Computational Modeling of Indentation of Thin Films

1.1 Introduction

With the development of science and technology, as well due to the needs of human life, materials from macro to micro, even to nano scales, have been applied widely. The performance of these materials varies significantly while their size changes. In order to characterize material properties in small scales, i.e., mechanical or piezoelectric properties, instrumented indentation method, which was developed from the traditional hardness testing method, emerged to provide people an easy, convenient and accurate technique. In recent decades, instrumented indentation based methods for determining mechanical properties of bulk specimen or thin film have received considerable and continue growing attention, due to its operability, potential applications and nondestructive features [1-3].

Rely on instrumented indentation method, numerous studies have successfully predicted material properties for the isotropic bulk sample [3, 4] and thin film [5], and even transversely isotropic bulk material [6]. Yet, most of those studies were focused on systems with a small number of unknown properties (less or equal to three), while fewer works tried to apply instrumented indentation method on a system with many variables, let alone serious discussions about the robustness, sensitivity or uniqueness in that case. Meanwhile, most studies about thin films assumed that the properties of the substrate were already known in advance, or they could be obtained through an alternative method. Moreover, fewer papers talked about if it was possible to extract the elastic or plastic properties of the substrate in a thin film system, even to get the properties of both the thin film and the substrate at the same time, i.e., from a single set of instrument indentation tests. In the end, although some works have been done for transversely isotropic bulk material [6], this property is obviously more important and popular for the thin film system. Nevertheless, almost no relevant literature could be found.

Based on the descriptions above, the three main purposes of the present study are:

1. To check the feasibility, together with the robustness, sensitivity, and uniqueness of

instrumented indentation method on a thin film system with a large number of variables;

2. To check the possibility of predicting the properties of the substrate and thin film simultaneously using instrumented indentation method;

3. To check the accuracy of using instrumented indentation method for extracting the transverse properties of thin film system.

The structure of this chapter is organized as follows. Background information and a summary of prior work done in predicting mechanical properties of bulk and thin film system in Section 1.2. The details of the numerical model developed in the present study are highlighted in Section 1.3. The results obtained from the present study are discussed in Section 1.4 and key conclusions from the present work are summarized in Section 1.5.

1.2 Background

1.2.1 Introduction to instrumented indentation method

$P-h$ curve, as shown in figure 1, captures the indentation force-depth response of the specimen. The main idea of instrumented indentation method is to create a relationship between $P-h$ curves, and mechanical properties of the corresponding material system. In other words, in instrumented indentation method, mechanical properties of a bulk or a thin film system are obtained by collecting enough information from $P-h$ curve(s), which are obtained through indenting experiments.

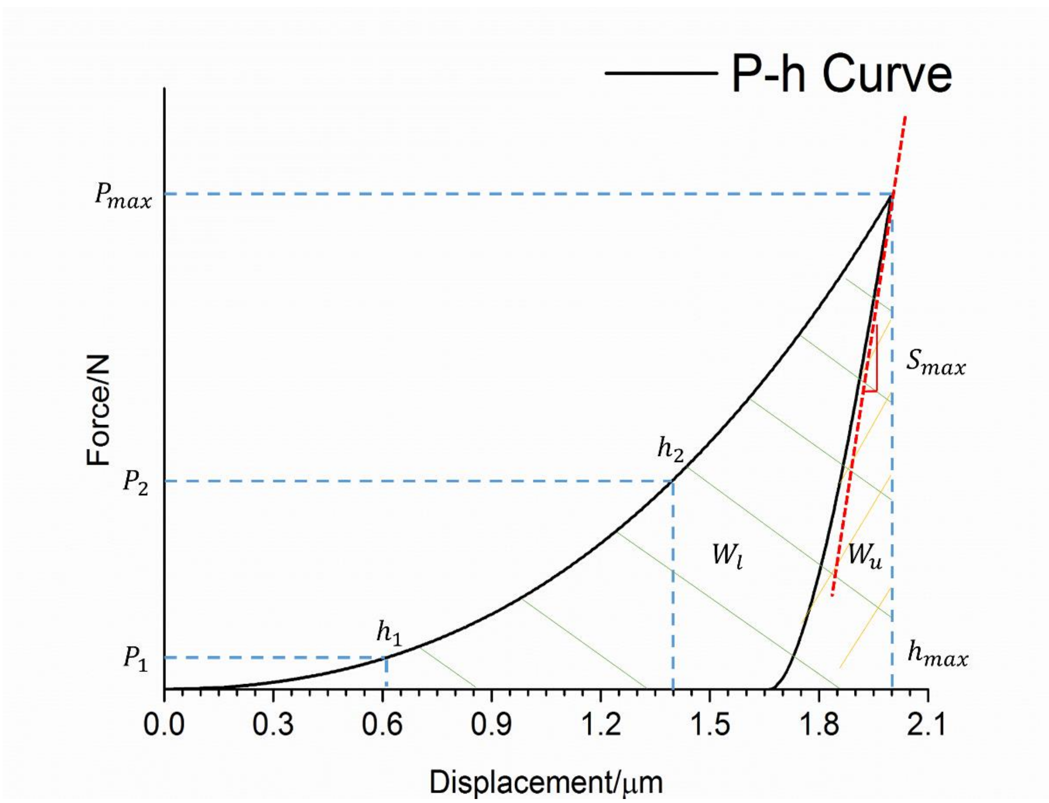

Figure 1. Schematic illustrating a $P-h$ curve in instrumented indentation method.

In figure 1, there are two solid curves and the left one is referred to as loading curve while the right one is referred to as unloading curve, both represent the relationship between 'P' and 'h'. Here, 'h' represents the displacement of indenter, therefore, h_1, h_2 and h_{max} correspond to indenter displacement as it at position 1, position 2 and maximum displacement, respectively. 'P'

represents the force acted on the indenter, therefore, P_1, P_2 and P_{max} stand for the value of force as indenter at position 1, position 2 and maximum displacement. Moreover, 'S', in figure 1, is the slope of the unloading curve, as S_{mas} represents the slope at the very initial point of unloading curve when indenter is infinitely close to maximum displacement. 'W' is the work done as indenter moves, therefore, W_l and W_u represents the work done in loading and unloading process, i.e., the area under loading and unloading curves, respectively.

Sneddon derived a general equation for the indenter displacement, h, and the loading load, P, as a solid indenter that could be described as revolution of a smooth function forced into a bulk material, as [7]:

$$P = Ch^m \qquad \text{Eq (1)}$$

where constant C is the loading curvature which is decided by the properties of both indenter and specimen, and m is a constant for a certain kind geometric of the indenter, i.e., $m = 2$ for conical indenters, $m = 1.5$ for sphere and paraboloids of revolution tip indenters, and $m = 1$ for flat cylinder indenters. Equation 1 was valid only when material deformations were limited to elastic.

With advanced studies, Oliver and Pharr found that when plastic deformation was included in consideration, above relationships would still work for cone indenter [8], however, the value of m was no longer a fixed value for sphere punches with different radius [9]. Oliver and Pharr [8], based on Sneddon's analysis [7], proposed that the elastic property of bulk materials can be obtained, if $P - h$ curve was accessible, from the equation as:

$$S_{max} = 2E_r r = \frac{2}{\sqrt{\pi}} E_r \sqrt{A_c} \qquad \text{Eq (2)}$$

where, r is the contact radius, A_c is the contact area, and the effective elastic modulus E_r could be expressed as:

$$\frac{1}{E_r} = \frac{1 - v^2}{E} + \frac{1 - v_i^2}{E_i} \qquad \text{Eq (3)}$$

where the subscripts 'i' represents the indenter. Therefore, E_i and v_i are the elastic modulus and Poisson's ratio of indenter, respectively, while E and v stand for the elastic modulus and Poisson's ratio of material of interest. They also got good results for determining the hardness of bulk specimen with above method [10]. Nevertheless, above analysis is restricted to the condition when contact edge, under the indenter, is sink-in, while for lots kinds of materials, contact edge is pile-up [11]. In equation 2, the estimation of contact area A_c between indenter and sample, which was usually inaccurate due to pile-up or sink in phenomena, has a direct influence on the calculation of material elastic modulus.

Dao [12], Cheng and Cheng [13, 14] were the pioneers of introducing the scaling laws and dimensionless analysis for developing relationships between the characteristic value on $P - h$ curves and material properties. By applying dimensionless analysis, the procedure of estimating contact area, A_c, could be avoided, firstly, and plastic properties of the specimen could also be obtained from $P - h$ curves through dimensionless equations. During this period, Venkatesh et al [2] proposed the idea of forward and reverse analysis, which extended the extent of instrumented indentation method, as shown in figure 2. It was not only possible to predict the properties of materials, but also possible to forecast $P - h$ curves if material properties were known in advance. Dimensionless analysis and forward and reverse analysis have almost become a fixed process of instrument indentation method today, *esp.*, for the complex material systems.

Although based on the work of Oliver and Pharr [8], lots of improved empirical and semi-empirical formulae have been proposed from both experimental observations and numerical simulations [9, 12, 15], there are many limitations when applying them. They either only work for the bulk system or only consider a simple system with a small number of variables. On the other hand, the intricate stress and strain status under indenters (in samples) during indenting is still poorly understood even as instrumented indentation method was widely accepted. So as to use instrumented indentation method on increasingly complex and practical problems, more studies would be expected on a more general material system, and also on the explanations for the stories happening inside it.

Thanks to the speedy development of computational technics, numerical methods today (finite element method, dimensionless analysis and forward and reverse analysis), can provide people a hands-on experience of understanding the relationship between material properties and $P - h$ curves (dimensionless analysis, forward and reverse analysis), and also enable people to visualize the indentation processes and responses inside the materials which are with flexible property combinations (finite element method).

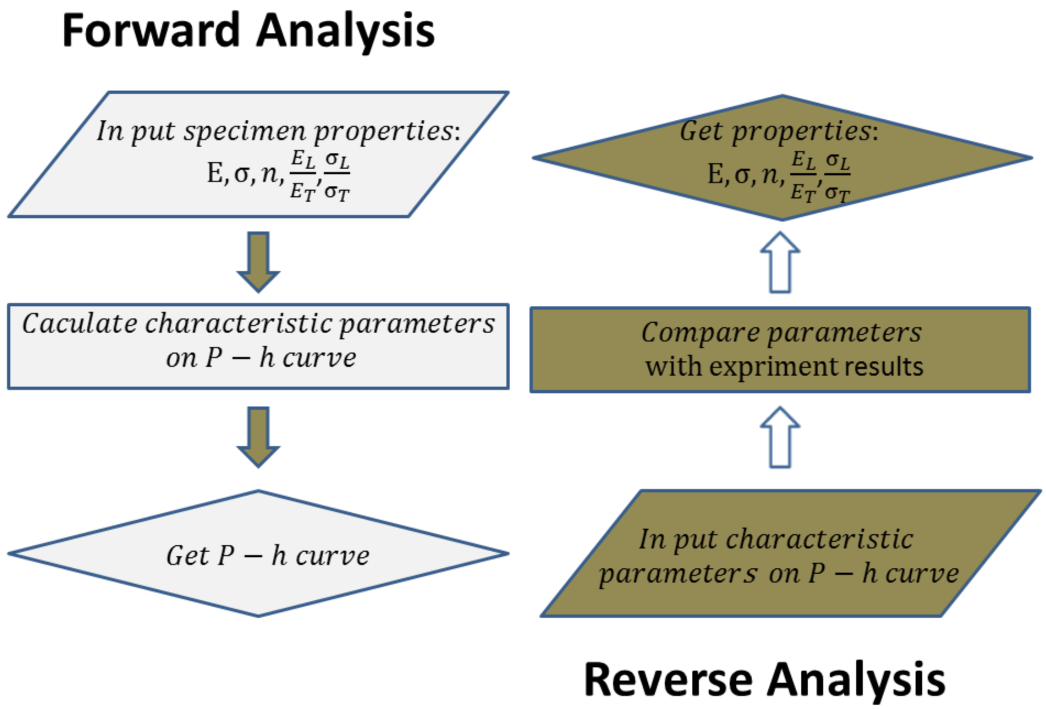

Figure 2. Schematic illustrating the idea of forward and reverse analysis.

Finite element method has been widely used for simulating instrumented indentation tests today [6]. Yet, in order to obtain a correct simulation outcome, the phenomenon of scale dependent effect (SDE) requires particular attention. When indentation happens in a significant small region, e.g., smaller than a micron, the phenomenon of scale dependent effect (SDE) becomes nonnegligible [16-18]. Several factors, such as friction between the indenter and the sample [19], strain gradient hardening [20] and surface free energy effect [21] could be helpful in explaining SDE. A pure Finite element method is difficult to take into account the influence of SDE since the classic continuum plasticity theory does not have a constituent internal length as a parameter for deformation [22]. In another word, the indentation depth should not be less than a micron [22], if conventional plasticity theories were used to describe the mechanic behaviors of a bulk specimen or a perfect connected thin film on a substrate.

Chen [23] proposes a method of using the impact of the substrate, i.e., introducing a characteristic length, to analyze the indentation process in a thin film system. They further put forward that P_1, P_2 and W_u could be three independent characteristic responses on the $P-h$ curve. Bhat and Venkatesh [6] introduced a ratio between the plastic work, W_p, and total work done in the loading procedure, W_l, to interpret P-h curves for transversely isotropic bulk materials.

Except predicting elastic and plastic properties from $P-h$ curves of indenting specimens [24, 25], instrument indentation method can also help to learn the deformation, fatigue, creep, fail behaviors of materials [26-31]. Moreover, this method is not restricted in the area of engineering, it has been adopted in many fields like geology [32], biomedicine [33], marine biology [34] etc. In a word, instrumented indentation method is a potential but powerful technology which can be widely applied.

1.2.2 Introduction to transversely isotropic materials

A transversely isotropic material is one with physical properties symmetric about an axis normal to a plane of isotropy, which means within this plane, all properties of this material are the regardless of directions. In the present paper, the direction perpendicular to the plane of isotropy is defined as the longitudinal direction, as directions being parallel to this plane is defined as the transverse directions.

Many thin films and coating might exhibit transversely isotropic property due to their fabrication process and the resulting microstructures[35-37]. Nakamura et al[35] proposed that for a transversely isotropic material, there were five independent constants to describe the elastic properties. The compliance matrix of a transversely material can be represented as:

$$\begin{bmatrix} \varepsilon_{11} \\ \varepsilon_{22} \\ \varepsilon_{33} \\ \gamma_{12} \\ \gamma_{23} \\ \gamma_{13} \end{bmatrix} = \begin{bmatrix} 1/E_T & -\nu_{LT}/E_L & -\nu_T/E_T & 0 & 0 & 0 \\ -\nu_{TL}/E_T & 1/E_L & -\nu_{TL}/E_T & 0 & 0 & 0 \\ -\nu_T/E_T & -\nu_{LT}/E_L & 1/E_T & 0 & 0 & 0 \\ 0 & 0 & 0 & 1/G_L & 0 & 0 \\ 0 & 0 & 0 & 0 & 1/G_L & 0 \\ 0 & 0 & 0 & 0 & 0 & 1/G_T \end{bmatrix} \begin{bmatrix} \sigma_{11} \\ \sigma_{22} \\ \sigma_{33} \\ \sigma_{12} \\ \sigma_{23} \\ \sigma_{13} \end{bmatrix} \quad \text{Eq (4)}$$

where, the subscripts 'L' and 'T' are, respectively, denoted to directions of longitudinal and transverse. Similarly, subscripts '1' and '3' represent the directions within the transverse plane, while subscript '2' represents the direction of longitudinal. The Poisson's ratio ν_T, ν_{LT} and ν_{TL} are defined as $-\frac{\varepsilon_{33}}{\varepsilon_{11}}$, $-\frac{\varepsilon_{11}}{\varepsilon_{22}}$ and $-\frac{\varepsilon_{22}}{\varepsilon_{33}}$, respectively. Meanwhile, the ratio between E_L and E_T and the ratio between ν_{LT} and ν_{TL} should be the same, as following:

$$\frac{E_L}{E_T} = \frac{\nu_{LT}}{\nu_{TL}} \quad \text{Eq (5)}$$

The in-plane shear modulus, G_T could be expressed as:

$$G_T = \frac{E_T}{2(1+\nu_T)} \quad \text{Eq (6)}$$

In order to reduce the variable numbers of elastic properties, two assumptions were made here [6]. First, the sum of ν_{LT} and ν_{TL} is defined as twice the value of ν_T, i.e., $2\nu_T = \nu_{LT} + \nu_{TL}$. Second, the out-of-plane shear modulus, G_L could be expressed as:

$$G_L = \frac{E_0}{2(1+\nu_T)} \quad \text{Eq (7)}$$

where, E_0 is the averaged elastic modulus of longitudinal and transverse direction of the thin film or the reference elastic modulus, i.e., $(E_L + E_T)/2$. So far, the elastic properties of a transversely isotropic material might be defined by only 3 parameters, i.e., E_0, E_L/E_T and ν_T.

For the plastic properties, Hill's [38] developed a yield criterion for anisotropic plastic deformation as:

$$F(\sigma_{22}-\sigma_{33})^2 + G(\sigma_{33}-\sigma_{11})^2 + H(\sigma_{11}-\sigma_{22})^2 + 2L{\sigma_{23}}^2 + 2M{\sigma_{31}}^2 + 2N{\sigma_{12}}^2 = 1 \quad \text{Eq (8)}$$

where, F, G, H, L, M and N, are constants that should be determined experimentally. Equation 8 can be modified for transversely isotropic materials as [35]:

$$f(\sigma) = \sqrt{P(\sigma_{22}-\sigma_{33})^2 + P(\sigma_{22}-\sigma_{11})^2 + Q(\sigma_{11}-\sigma_{33})^2 + 2R{\sigma_{23}}^2 + 2R{\sigma_{12}}^2 + 2S{\sigma_{13}}^2} - \sigma_0$$

$$and\ f(\sigma) = 0 \quad \text{Eq (9)}$$

where, P, Q, R and S are the dimensionless constants that related to σ_0 as:

$$\begin{cases} P = \frac{1}{2}(\frac{\sigma_0}{\sigma_L})^2 \\ Q = \frac{1}{2}\left(2\frac{{\sigma_0}^2}{{\sigma_T}^2} - \frac{{\sigma_0}^2}{{\sigma_L}^2}\right) \\ R = \frac{1}{2}(\frac{\sigma_0}{\tau_L})^2 \\ S = \frac{1}{2}(\frac{\sigma_0}{\tau_T})^2 \end{cases} \quad \text{Eq (10)}$$

where, σ_0 is the reference yield stress equal to $(\sigma_L + \sigma_T)/2$, and σ_L, σ_T, τ_L and τ_L are yield stress along different directions, respectively. Lan *et al.* [3] described stress-strain and elastoplastic behavior of bulk materials as:

$$\sigma = \begin{cases} E\varepsilon, (\sigma \leq \sigma_Y) \\ R\varepsilon^n = \sigma_Y \left(1 + \dfrac{E}{\sigma_Y}\varepsilon_n\right)^n, (\sigma \geq \sigma_Y) \end{cases} \qquad \text{Eq (11)}$$

where n is the strain hardening exponent, σ_Y is the yield stress at initial, and ε_n is the non-linear strain. In order to reduce the variable numbers of plastic properties, three assumptions for plastic properties were made in present work [6]. First, so as to extend the isotropic power law hardening to transversely isotropic materials, the post yield behavior for both longitudinal and transverse directions would be assumed to follow the same rules as bulk materials. Second, longitudinal and transverse directions would share the same constant work hardening exponent. After introducing these two assumptions, elastoplastic behavior of transversely isotropic materials could be described as in equation 12 and equation 13, for longitudinal and transverse direction, respectively:

$$\sigma_L = \begin{cases} E_L\varepsilon_L, (\sigma_L \leq \sigma_{YL}) \\ R\varepsilon_L^n = \sigma_{YL} \left(1 + \dfrac{E_L}{\sigma_{YL}}\varepsilon_{nL}\right)^n, (\sigma_L \geq \sigma_{YL}) \end{cases} \qquad \text{Eq (12)}$$

and

$$\sigma_T = \begin{cases} E_T\varepsilon_T, (\sigma_T \leq \sigma_{YT}) \\ R\varepsilon_T^n = \sigma_{YT} \left(1 + \dfrac{E_T}{\sigma_{YT}}\varepsilon_{nT}\right)^n, (\sigma_T \geq \sigma_{YT}) \end{cases} \qquad \text{Eq (13)}$$

Third, shear yield stress of longitudinal and transverse directions follows the von Mises criterion, i.e., τ_L and τ_T can be approximately expressed as:

$$\begin{cases} \tau_L = \dfrac{\sigma_0}{\sqrt{3}}\sqrt{\dfrac{\sigma_L}{\sigma_T}} \\ \tau_T = \dfrac{\sigma_0}{\sqrt{3}} \end{cases} \qquad \text{Eq (14)}$$

It can be seen, now the plastic properties of transversely isotropic materials may also be defined by 3 parameters, i.e., σ_0, σ_L/σ_T and n.

In summary, totally six parameters (E_0, E_L/E_T, ν_T, σ_0, σ_L/σ_T and n) are required to fully describe the mechanic behavior of transversely isotropic materials.

1.2.3 Introduction to dimensionless analysis

Two geometric objects are described as geometric similar as their lengths are all proportional to each other with the same proportional constant, and all angles are identical [39]. For instrumented indentation, sphere and flat cylinder indenters, which by themselves possess characteristic lengths, are not geometric similar, due to that there is another length parameter, i.e., displacement of the indenter. However, all cone indenters are geometric similar if they have an equal half angle, θ, at the tip.

The dimensionless analysis is the elementary idea helping to create the relationships between $P-h$ curve and material properties which could be, then, applied for further forward and reverse analysis. The so-called Π-theorem, proposed by Buckingham [40], is the basic law of dimensionless analysis. Buckingham emphasized that physical laws do not depend on arbitrarily chosen basic units of measurement, or all terms that are added together must have the same unit. In instrumented indentation, there are two basic dimensions, i.e., length and mass. Therefore, an unknown quantity, y, could be, without loss of generality, written as:

$$y = f(x_1, x_2, \cdots, x_n) \quad \text{Eq (15)}$$

then assume that x_1 and x_2 have independent dimensions, so equation 15 might be modified as:

$$\frac{y}{{x_1}^{c_1} \times {x_2}^{c_2}} = f(x_1, x_2, \frac{x_3}{{x_1}^{c_{31}} \times {x_2}^{c_{32}}} \cdots, \frac{x_n}{{x_1}^{c_{n1}} \times {x_2}^{c_{n2}}}) \quad \text{Eq (16)}$$

where, c_1, c_2, c_{n1} and c_{n2} are all constants which make $\frac{y}{{x_1}^{c_1} \times {x_2}^{c_2}}$ and $\frac{x_n}{{x_1}^{c_{n1}} \times {x_2}^{c_{n2}}}$ dimensionless terms. Since in a physical law, all terms must have the same unit, here in equation 16, all terms should be dimensionless. Therefore, equation 16 can be simplified as:

$$\frac{y}{{x_1}^{c_1} \times {x_2}^{c_2}} = \Pi(\frac{x_3}{{x_1}^{c_{31}} \times {x_2}^{c_{32}}} \cdots, \frac{x_n}{{x_1}^{c_{n1}} \times {x_2}^{c_{n2}}}) \quad \text{Eq (17)}$$

It’s obviously by applying Π-theorem, number of variables for describing an unknown quantity was reduced by two.

1.3 Finite element models

The transversely isotropic thin film system of interest in present work is shown in figure Figure 3.

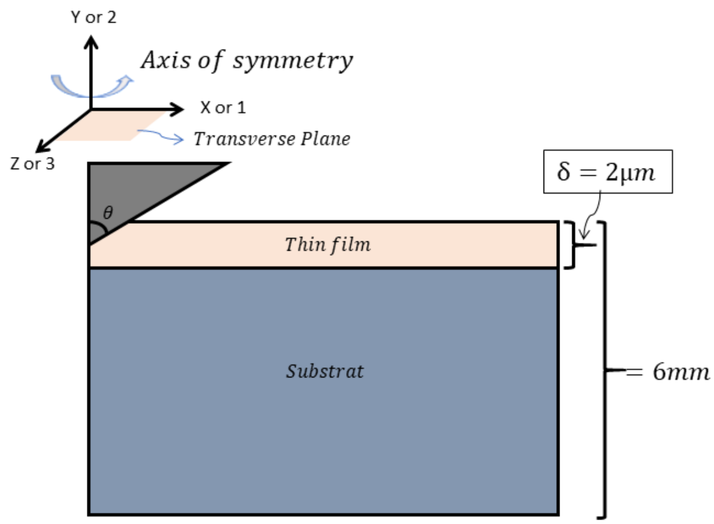

Figure 3. Schematic illustrating the transversely isotropic thin film system of interesting in present study.

As shown in section 1.2.2, there are at least six variables for depicting a transversely isotropic material. Therefore, there should be more than twelve variables for a totally transversely isotropic thin film system. As an exploratory research, only transversely isotropic plasticities were assigned to the top thin film, with its elastic properties still being isotropic. Later on, it will be shown that transversely isotropic elasticities have little influence on $P - h$ curves, which means it might ask for other assistant methods if transversely isotropic elasticities are wanted. Meanwhile, the bottom substrate was simplified to possessed an unknown isotropic elastic modulus only. The indentation happened along the longitudinal direction with conical indenters. The half angle of the conical indenter, θ, was set equivalent to 60°, 70.3° or 80°. The substrate thickness was as large as 3,000 times the thickness of thin film, δ, which enabled the assumption that all far boundary conditions had ignorable effect on simulation results [41]. In the present study, for the purpose of direct explanations of simulation results, the film thickness was assigned to be 2 μm, which, of course, is not necessary. Therefore, substrate thickness would equal to 6 mm according to previous discussion. The maximum displacement of indenters was also assigned to be 2 μm for all simulations, i.e., 100% 'penetration ratio' (not really to pierce through the thin film). Since there was no constituent internal length in current models (or say there was no internal unit system in Abaqus), simulation results could be easily transferred to represent the indentation for such thin film system with any thin film thickness, while the only requirement was that the maximum indenter penetration ratio, h/δ, should equal to 100%.

All material property combinations for the transversely isotropic thin film system are shown in figure 4.

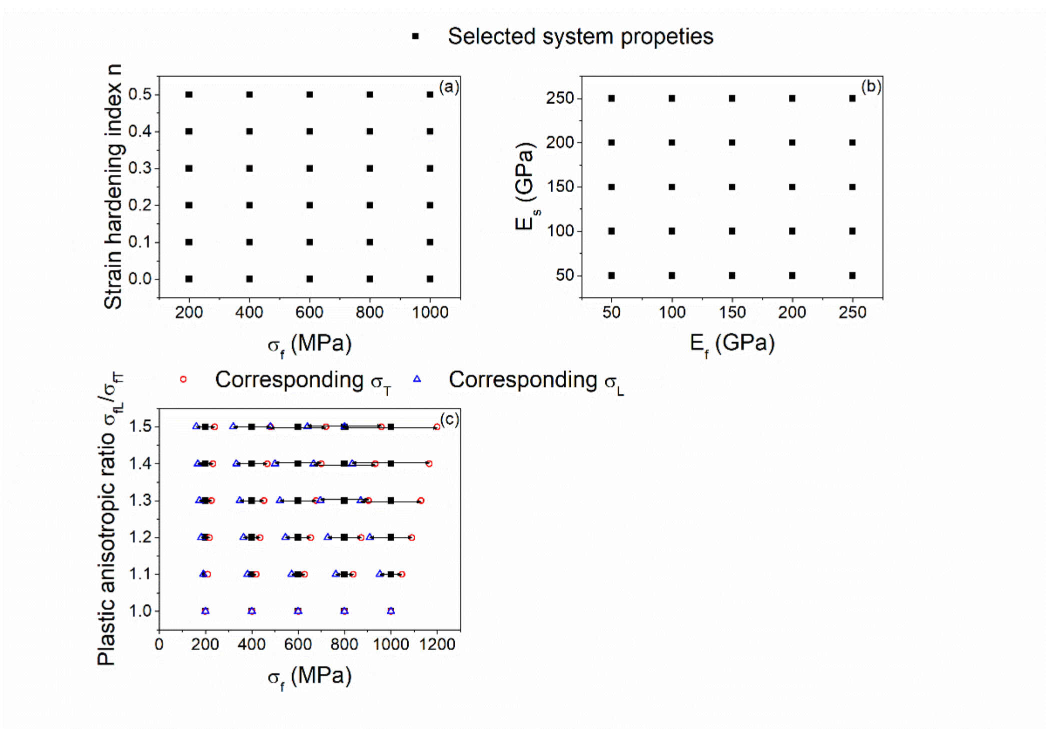

Figure 4. Plots displaying selected transversely isotropic thin film system properties: (a) σ_f vs n; (b) E_f vs E_s; (c) σ_f vs σ_{fL}/σ_{fT}.

In figure 4, each black square represents a property combination of the models. In general, the initial yield stress of most metal or alloy falls within the range of 30 MPa to 1100 Mpa, with elastic modulus within the range of 40 GPa to 210 GPa, while work hardening is about 0 to 0.5

[42]. In present work, the value of film elastic modulus, E_f, ranged from 50 to 250 GPa, reference yield strength, σ_f, from 200 to 1000 MPa, strain hardening index, n, ranged from 0 to 0.5, transversely isotropic ratio of plasticity, σ_{fL}/σ_{fT}, ranged from 1.0 to 1.5, while the substrate elastic modulus, E_s, ranged from 50 to 250 GPa. ν_T and ν_s was set to be 0.3 for all situations since this approximation value falls close to most metal. Moreover, effect of Poisson's ratio could be ignored when simulating an instrumented indentation.

Detailed information of the possible combination of thin film system properties can also be found in table 1. From table 1, and be aware of that there are three different half angle conical indenters, about 13500 ($5 \times 5 \times 6 \times 6 \times 5 \times 3 = 13500$) simulations need to be carried out in the present study. So many finite element models were included so as to exclude the impacts, due to insufficient data support, on the analysis of the feasibility, robustness, and sensitivity of instrumented indentation method later.

Table 1. Range of Material Properties

Properties	**Min**					**Max**
$\boldsymbol{E_f}$	50 GPa	100 GPa	150 GPa	200 GPa	250 GPa	
$\boldsymbol{\sigma_f}$	200 MPa	400 Mpa	600 MPa	800 MPa	1000 MPa	
$\boldsymbol{n}$	0	0.1	0.2	0.3	0.4	0.5
$\boldsymbol{\frac{\sigma_L}{\sigma_T}}$	1.0	1.1	1.2	1.3	1.4	1.5
$\boldsymbol{E_s}$	50 GPa	100 GPa	150 GPa	200 GPa	250 GPa	

All simulations of the instrumented indentation in the present study were conducted by using two-dimensional (2D) axisymmetric models included in Abaqus 6.14. Although three-dimensional models are preferred in recent studies, due to a lot of simulations need to be carried out, only 2D models were created in the present work. Moreover, 2D models can fully meet the requirement of describing the transversely isotropic properties of the system with features of conical indenters. Thirdly, 2D models show excellent agreement with experimental results and simulation outcomes based on 3D models [43-45].

Roller boundary condition was assigned to the axis of in-plane symmetric. The displacement of nodes at bottom along the out-of-plane direction was fixed to zero while all nodes at other boundary sides unrestrained. Bucaille et al. [46] found that the friction coefficient between slave and master surfaces was very small for the large value semi-angle (60° and 70.3°) conical indenters. Antunes et al. [47] further pointed it out that the influence of friction coefficient could be neglected. No friction between the surface of indenters and samples was considered in present work. Moreover, indenters were with perfect sharp tip and rigid body in all simulations. And the thin film was designed to be completely flat at the top so as to possess perfect connections to the substrate.

For each model, there were more than 18,000 elements, mixed of CAX4R and CAX3 types, as shown in figure 5. The element size was designed to be fine enough to make sure there were more than 100 elements to describe the interaction between slave and master surfaces from samples and indenters, respectively, as maximum displacement reached. Element size became increasingly coarse when near the far away boundary on considering of time consumed. All simulations are carried out by using general purpose finite element package of ABAQUS on DELL workstation T7500 with up to 8 cores.

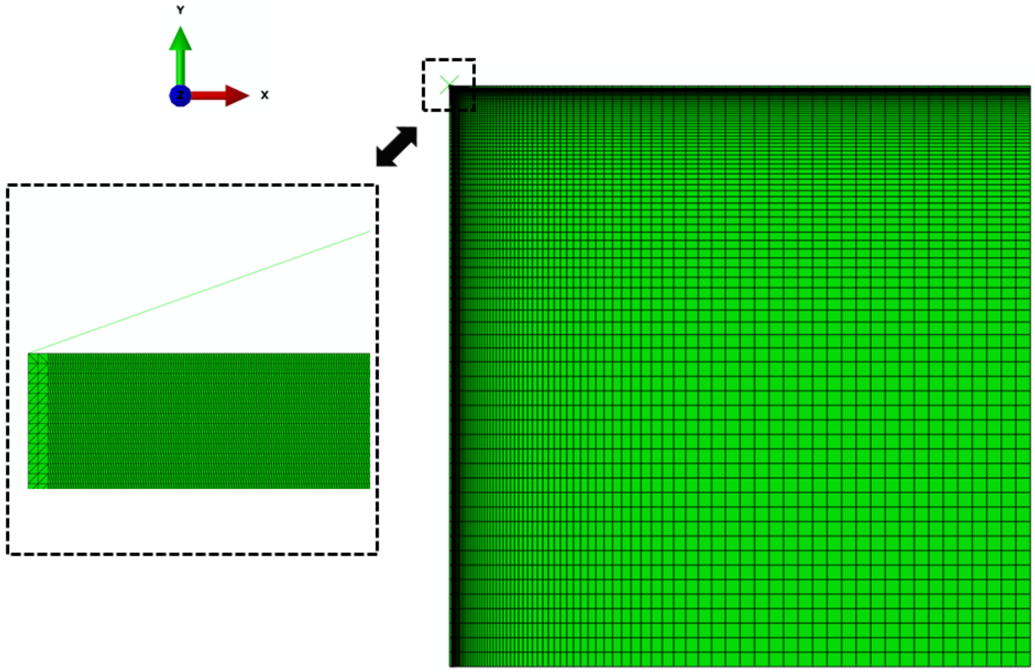

Figure 5. Diagram displaying mesh details of a transversely isotropic thin film model.

1.4 Discussion

1.4.1 Influences of transversely isotropic elastic properties of thin films on $P-h$ curves

Before analyzing the results from the systematical simulations, the influences from transversely isotropic properties of the thin film were first studied. The reference elastic modulus of the thin film was fixed as 800 MPa, while reference yield strength of the thin film fixed as 200 GPa, and strain hardening index fixed as 0.2. In figure 6(a) and (c), substrates was only assigned with isotropic elasticity as 150 GPa, while in figure 6(b) and (d), substrates possess properties like silicon, i.e., E_s as 190 GPa, σ_s as 7 GPa [48] and ν_s as 0.17 [49]. In figure 6(a) and (b), the plastic properties were isotropic for the thin film while its elastic anisotropic ratio varied from 1.0 to 1.5. At the same time, in figure 6(c) and (d), the plastic anisotropic ratio of the thin film could change from 1.0 to 1.5 as its elastic anisotropic ratio was fixed at 1.0.

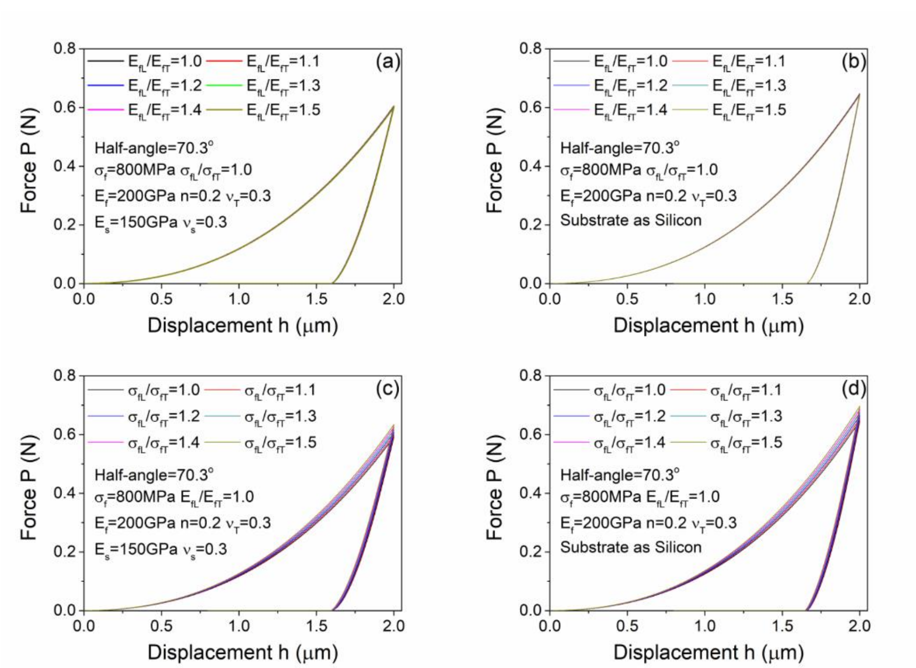

Figure 6. Plots illustrating how $P-h$ curves change with transversely anisotropic ratio of E_{fL}/E_{fT} and σ_{fL}/σ_{fT} on different substrate: (a) and (c) elastic only substrate, (b) and (d) single crystal silicon.

It's very clear that the impact from transversely isotropic elasticity of thin film on the $P-h$ curves is very slight regardless the type of substrate materials, as shown in figure 6(a) and (b).

When the value of E_{fL}/E_{fT} grows from 1.0 to 1.5, the maximum force applied on the indenter only decreased by 0.7%. Even while the substrate is a real material i.e., single crystal silicon, which has a pretty similar property to present system, the impact is still unnoticed. Yet, it can be noticed in figure 6(c) and (d) transversely isotropic plasticity has a significant influence on the results of instrumented indentation, either for pure elastic substrate or single crystal silicon substrate. The force need for a 100% penetration of indenter increased by about 7.5% when the transversely isotropic ratio of plasticity, σ_{fL}/σ_{fT} is raised from 1.0 to 1.5. Such phenomenon can be understood as a value of 1.5 for σ_{fL}/σ_{fT} means higher yield strength in the direction of longitudinal, i.e. opposite to the moving direction of the indenter.

By carefully considering the three main purposes of present work, and assess the trade-off between time consumed and the completeness of simulation results, transversely isotropic plasticity would not be considered more in following sections.

1.4.2 Dimensionless analysis for current transversely isotropic thin film system

According to the discussion above, any unknown quantity in such system can decided by the variables as: indenter displacement, h, half angle of indenter, θ, thin film thickness, δ, together with the mechanical properties of the transversely isotropic system as: E_f, ν_T, σ_f, σ_{fL}/σ_{fT}, n, E_s, ν_s. Moreover, as ν_{T} and ν_s were set to the value of 0.3, and θ were already known in advance, then the unknown quantity, Y, can be expressed as:

$$Y = F\left(h, \delta, E_f, \sigma_f, \frac{\sigma_{fL}}{\sigma_{fT}}, n, E_s\right) \qquad \text{Eq (18)}$$

Choosing δ and σ_f as two quantities with independent dimensions, and applying the Π-theorem, equation 18 can be modified as:

$$Y_\pi = \Pi\left(\frac{h}{\delta}, \frac{E_f}{\sigma_f}, \frac{E_f}{E_s}, \frac{\sigma_{fL}}{\sigma_{fT}}, n\right) \qquad \text{Eq (19)}$$

where Y_π is the dimensionless term of Y.

Theoretically, there are total 5 undetermined properties of the transversely isotropic thin film system of interest. It's almost impossible to get an analytical solution for such a complicated system with single instrumented indentation as a single $P-h$ might not be enough to figure out so many properties [50]. This was why, conical indenters with three different semi-angle degrees, i.e., $60°$, $70.3°$ and $80°$ were used in the present study. Thus, for each thin film system, there were three $P-h$ curves and on each $P-h$ curve, five characteristic responses were collected. They were P_1 ($h_1 = 0.6$ µm, i.e., penetration ratio at 30%), P_2 ($h_1 = 0.4$ µm, i.e., penetration ratio at 70%), W_l (work done by loading, i.e., penetration ratio reached 100%), W_u (work done by unloading, i.e., penetration ratio reached 100%), S_{max} (the slope at the very initial point of unloading curve, i.e., penetration ratio reached 100%). Therefore, a total of 15 characteristic responses needs to be recorded for complete instrumented indentation method. Without a doubt, the penetration ratio, h/δ, in P_1 and P_2 can be adjusted as required or for convenience in a practical use. The only restriction here is that penetration ratio should be the same for all three indenters. Since the penetration ratio, h/δ, for each characteristic response was already known before any analysis, equation 19 can be further simplified here as:

$$Y_\pi = \Pi\left(\frac{E_f}{\sigma_f}, \frac{E_f}{E_s}, \frac{\sigma_{fL}}{\sigma_{fT}}, n\right) \qquad \text{Eq (20)}$$

After applying Π-theorem on all five characteristic responses from a single $P - h$ curve, a group of Π functions which would be widely referred later was obtained:

$$\begin{cases} \dfrac{P_1}{\sigma_f {h_1}^2} = \Pi_{i1}\left(\dfrac{E_f}{\sigma_f}, \dfrac{E_f}{E_s}, \dfrac{\sigma_{fL}}{\sigma_{fT}}, n\right) \\ \dfrac{P_2}{\sigma_f {h_2}^2} = \Pi_{i2}\left(\dfrac{E_f}{\sigma_f}, \dfrac{E_f}{E_s}, \dfrac{\sigma_{fL}}{\sigma_{fT}}, n\right) \\ \dfrac{W_l}{\sigma_f {h_{max}}^3} = \Pi_{i3}\left(\dfrac{E_f}{\sigma_f}, \dfrac{E_f}{E_s}, \dfrac{\sigma_{fL}}{\sigma_{fT}}, n\right) \\ \dfrac{W_u}{\sigma_f {h_{max}}^3} = \Pi_{i4}\left(\dfrac{E_f}{\sigma_f}, \dfrac{E_f}{E_s}, \dfrac{\sigma_{fL}}{\sigma_{fT}}, n\right) \\ \dfrac{S_{max}}{\sigma_f h_{max}} = \Pi_{i5}\left(\dfrac{E_f}{\sigma_f}, \dfrac{E_f}{E_s}, \dfrac{\sigma_{fL}}{\sigma_{fT}}, n\right) \end{cases} \qquad \text{Eq (21)}$$

where, subscript i equals to 1, 2 or 3, represents the indenter with half angel of $60°, 70.3°$ and $80°$ respectively.

For efficient and convenient purposes, hereafter, $\frac{P_1}{\sigma_f {h_1}^2}$, $\frac{P_2}{\sigma_f {h_2}^2}$, $\frac{W_l}{\sigma_f {h_{max}}^3}$, $\frac{W_u}{\sigma_f {h_{max}}^3}$ and $\frac{S_{max}}{\sigma_f h_{max}}$ are referred to y_{i1}, y_{i2}, y_{i3}, y_{i4} and y_{i5}, respectively. And the terms of $\frac{E_f}{\sigma_f}$, $\frac{E_f}{E_s}$, $\frac{\sigma_{fL}}{\sigma_{fT}}$, n are referred to x_1, x_2, x_3 and x_4, respectively. Thus, equation 21 could be condensed as:

$$y_{\mathrm{ij}} = \Pi_{ij}(x_1, x_2, x_3, x_4) \qquad \text{Eq (22)}$$

where subscript *j* equals a value from 1 to 5, stands for the 5 characteristic responses of $\frac{P_1}{\sigma_f {h_1}^2}$, $\frac{P_2}{\sigma_f {h_2}^2}$, $\frac{W_l}{\sigma_f {h_{max}}^3}$, $\frac{W_u}{\sigma_f {h_{max}}^3}$ and $\frac{S_{max}}{\sigma_f h_{max}}$, respectively.

Thus, the major responsibility of present study became into definding a precise expression of Π_{ij}, which is the basis of forward and reverse analysis.

1.4.3 Verification of dimensionless analysis on current system

In equation 21, if σ_{fL}/σ_{fT} and n are unchanged, characteristic responses, y_{ij}, becomes dependent on only the ratios of σ_{fL}/σ_{fT} and E_{fL}/E_{fT}. That is to say, even when the values of E_f, σ_f and E_s are totally different for systems, characteristic responses, y_{ij}, could be totally the same as long as two systems possess equal value for σ_{fL}/σ_{fT} and E_{fL}/E_{fT}.

In table 2, there were 5 transversely isotropic thin film systems. They shared the same value of σ_{fL}/σ_{fT} and n, yet, totally different values for E_f, σ_f and E_s. Five thin film systems with different property combination were, then, indented by the $70°$ conical indenter which leads into 5 distinguishable $P - h$ curves just as shown in figure 7.

Table 2. Five transversely isotropic thin film systems having diverse properties for both thin and substrate.

System Number	$\boldsymbol{E_f}$**/GPa**	$\boldsymbol{\sigma_f}$**/MPa**	$\boldsymbol{E_s}$**/GPa**	$\boldsymbol{\frac{\sigma_{fL}}{\sigma_{fT}}}$	$\boldsymbol{n}$
1	50	200	50	1.2	0.2
2	100	400	100	1.2	0.2
3	150	600	150	1.2	0.2
4	200	800	200	1.2	0.2
5	250	1000	250	1.2	0.2

The five characteristic responses were collected from each of the curves in figure 7. The Π values of characteristic responses, were included in table 3. Obviously, five systems possessed the same values (with the maximum deviation less than 0.03%) for all characteristic responses. In summary, dimensionless analysis works well on transversely isotropic thin film systems and can be greatly helpful for forward and reverse analysis.

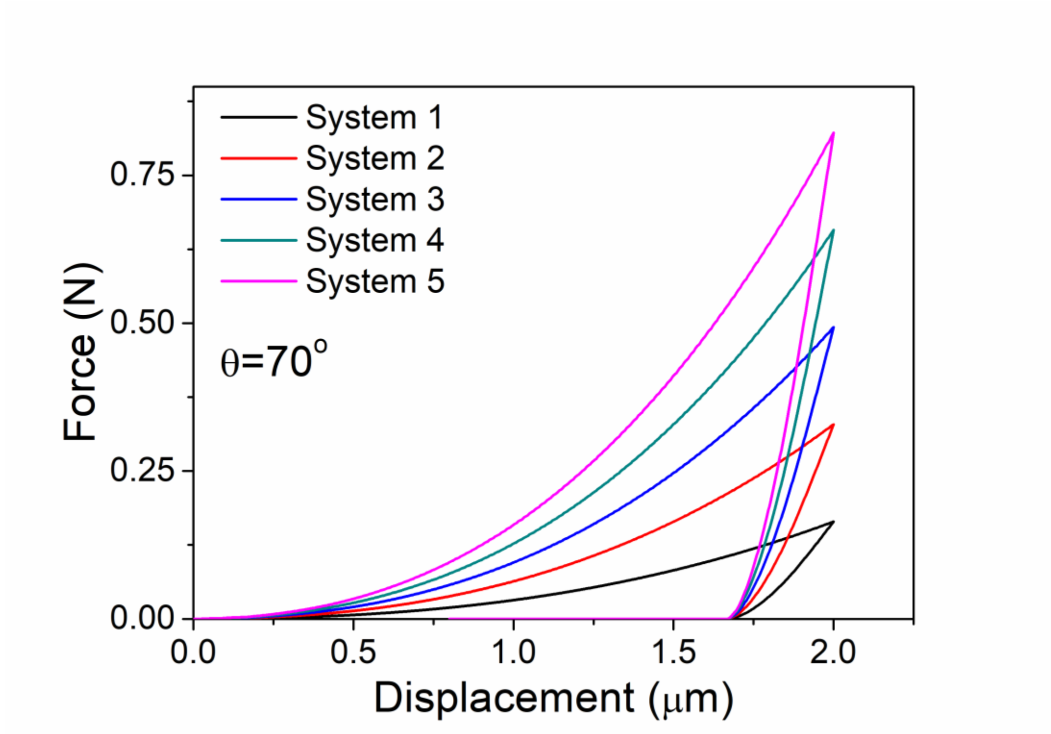

Figure 7. Five thin film systems with different properties show clearly distinguishable $P-h$ curves.

Table 3. Five transversely isotropic thin film systems with diverse properties for both thin and substrate show the same value for Π_{21} to Π_{25}

System Number	$\frac{P_1}{\sigma_f h_1^2}$	$\frac{P_2}{\sigma_f h_2^2}$	$\frac{W_l}{\sigma_f h_{max}^3}$	$\frac{W_u}{\sigma_f h_{max}^3}$	$\frac{S_{max}}{\sigma_f h_{max}}$
1	140.2778	177.6786	60.78125	13.7875	1761.125
2	140.2778	177.6658	60.78125	13.7875	1761.125
3	140.2778	177.6701	60.78125	13.78958	1760.833
4	140.2778	177.6722	60.78125	13.78906	1760.625
5	140.2778	177.6735	60.78125	13.78875	1760.75

1.4.4 Expression creating based on dimensionless analysis

According to figure 2, the forward analysis means to predict the characteristic responses on $P-h$ given that properties of thin film system were already known, and *vice-versa* for the reverse analysis. But, before the discussing of details about the forward and reverse analysis, it's better to be aware of the truth there would a huge amount of data need to be explained and the range for any single property, elastic or plastic, isotropic or anisotropic, is very wide. Therefore, it could be very hard to find an individual relationship which can describe all related data very well. In order to improve the efficiency and accuracy, grouping, divide the database into smaller clusters, is suggested. Bhat[6] performed grouping by dividing materials into smaller groups according to their property. This method works well but does bring users a little trouble when doing the reverse analysis later. It requires the knowledge of material properties in advance, then a user can decide which group the sample belongs to. And reverse analysis is more likely to be used for practical problems which means, in the process of reverse analysis, people might know nothing about the sample at the very beginning. Certainly, alternative methods could be applied so as to learn something about the samples beforehand, which definitely would increase the cost of both money and time.

In the present study, a change was made based on work of Bhat[6]. All data were divided into smaller groups according to corresponding indentation outcomes (the value of two characteristic responses). A detailed grouping strategy is given in figure 8. Since there were three indenters, i.e., three $P-h$ curves, for a certain thin film system, data for this system might belong to different a group for different indenters. The critical values of y_{i4} and y_{i5} for grouping in present study, i.e., b_{i1} and b_{i2}, and c_{i1}, c_{i2} and c_{i3}, can be found in Appendix A. Of course, the value of $b_{i1}$and b_{i2}, and c_{i1}, c_{i2} and c_{i3} could be adjusted so as to serve the analysis better.

In order to distinguish y_{ij} or $\Pi_{ij}(x_1, x_2, x_3, x_4)$ after grouping and highlight its group number, the number of digits of subscript was increased from two, ij, to three, ijk, where k can take the value from 1 to 6, standing for the number of groups, as i and j with unchanged meanings.

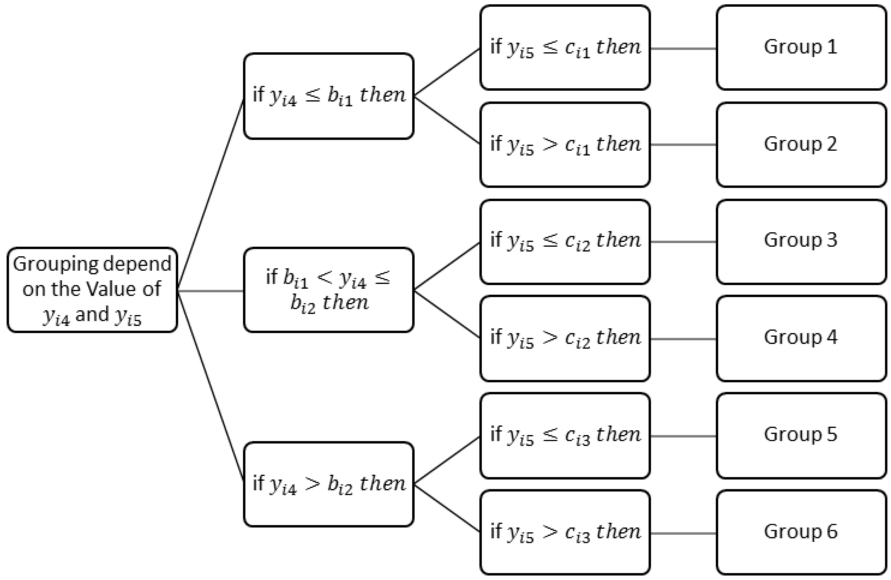

Figure 8. Schemitcs illustrating the strategy of grouping according to the value of y_{i4} and y_{i5}. b_{i1}, b_{i2} and b_{i3}, and c_{i1}, c_{i2} and c_{i3} are critical values of y_{i4} and y_{i5}, respectively, where i = 1, 2 or 3, presents the indenter with 60°, 70.3° and 80°, respectively.

Technically, there are various methods and types of function that could be used for fitting y_{ijk}, with x_1, x_2, x_3 and x_4, so as to relate the properties were input for simulation and the calculation outcomes from the 13,500 models. y_{ijk} may or may not share the same expression style for different characteristic responses. To make the analysis here more general, only polynomial expression were applied and all characteristic responses were required to share the same form of polynomial expression, as:

$$y_{ijk} = \sum_{l} a_{ijkl} x_1^m x_2^n x_3^p x_4^q \qquad \text{Eq (23)}$$

where a_{ijkl} is the parameter in front of any term of polynomial, as subscript 'l' represents the sequence number of the terms in the polynomial. m, n, p and q are exponents.

In order to find the appropriate expression of y_{ijk} and control the degrees of polynomial function so as to control the scale of polynomial, some limitation must be acted on the value of m, n, p and q, although most of the time, larger the polynomial scale, better the fitting results. Two limits are as:

$$\begin{gathered} |m|, |n|, |p|, |q| \leq 3 \\ |m| + |n| + |p| + |q| \leq 4 \end{gathered} \quad \text{Eq (24)}$$

In actual operation, one term might be removed as it cannot contribute to improving the fitting results at all. At last, there were 75 terms left. The specific expression of y_{ijk}, together with the tables for a_{ijkl} were included in Appendix B.

In table 4, the coefficient of determinations, R^2, for all y_{ijk}, were included. All the values of the coefficient of determination, R^2, are almost equal to 1 for all characteristic responses, y_{ijk}, indicated good fitting results in all groups with all indenters, which verifies the strategies of creating polynomial and grouping.

After the determination of both expression and parameters in the polynomial which could be used to describe the relationship between thin film system properties and characteristic responses on $P-h$ curves, forward and reverse analysis now can be performed based on it.

Table 4. Coefficient of determination, R^2, for fitting y_{ijk} with x_1, x_2, x_3 and x_4.

Group #	$\boldsymbol{y_{11}}$	$\boldsymbol{y_{12}}$	$\boldsymbol{y_{13}}$	$\boldsymbol{y_{14}}$	$\boldsymbol{y_{15}}$
1	1	1	1	0.9999	0.9999
2	1	1	1	0.9999	1
3	1	1	1	1	1
4	1	1	1	1	1
5	1	1	1	1	1
6	1	1	1	1	1

Group #	y_{21}	y_{22}	y_{23}	y_{24}	y_{25}
1	0.9999	1	1	0.9999	1
2	0.9999	1	1	1	1
3	1	1	1	0.9999	1
4	1	1	1	1	1
5	1	1	1	1	1
6	1	1	1	1	1
Group #	y_{31}	y_{32}	y_{33}	y_{34}	y_{35}
1	0.9999	0.9999	0.9999	0.9998	0.9999
2	0.9999	1	1	1	1
3	1	0.9999	0.9999	0.9999	1
4	1	1	1	1	1
5	1	1	1	1	1
6	1	1	1	1	1

1.4.5 Forward analysis for current transversely isotropic thin film system

A combination of total 100 simulation samples was used to verify the forward and reverse analysis results for present studies. 70 samples are with new system properties which are not included in the 13,500 models. The simulation outcomes of these 70 samples were then compared to the calculation results through equation 23 with suitable values of a_{ijkl}. The left 30 were selected from the 13,500 models so as to see if these two groups of test samples show a significant difference in accuracy. Complete information about system properties for all 100 test samples can be found in appendix C.

The strategy of the forward analysis is quite straightforward now and is shown in figure 9. As mentioned above, the flow path is independent for three indenters, which means the process needs to be carried for three indenters independently.

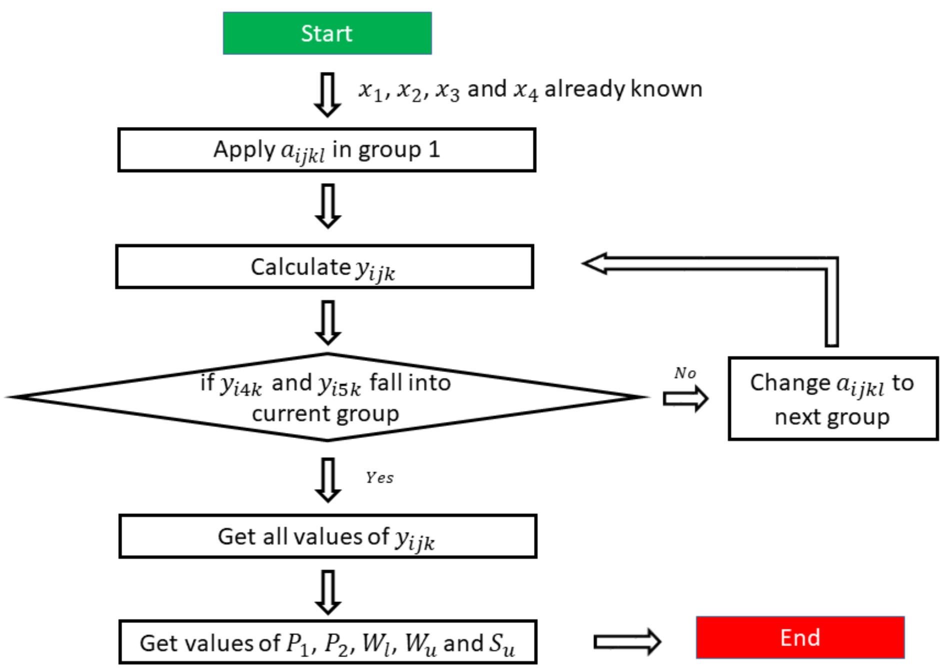

Figure 9. Sehcmetic illustrating forward analysis flow path.

In table 5, a comprehensive error information (in percentage) of the forward analysis of all y_{ijk} was included. The average errors for the predictions all 15 characteristic responses (5 for each indenter) are fairly low, less than 0.77%. Even the maximum errors of 100 test samples are all below 5.88% which is acceptable when considering such a complicated thin film system. As the standard deviation values are also pretty low for all cases, it's clear that most samples have comparable error level. That is to say, the expression obtained in section 1.4.4 is stable and precise in relating thin film system properties and characteristic responses on $P-h$ curves. y_{i4}, in another word, S_{max}, the slope of initial unloading curve, exposes the highest error level for all three indenters which might due to the method how this value extracted from $P-h$ curves or an unstable status at the very beginning of unloading simulations. Moreover, it can be found that predicting of y_{ij} for smaller half angle indenter is more accurate than for larger one.

Table 5. Percentage errors of forward analysis results for all y_{ijk}.

$\boldsymbol{\theta = 60°}$	$\boldsymbol{y_{11}}$	$\boldsymbol{y_{12}}$	$\boldsymbol{y_{13}}$	$\boldsymbol{y_{14}}$	$\boldsymbol{y_{15}}$
Maximum error	1.22%	1.27%	1.33%	5.88%	1.97%
Minimum error	0.00%	0.00%	0.00%	0.00%	0.01%
Average error	0.20%	0.12%	0.12%	0.77%	0.26%
Standard deviation	0.21%	0.15%	0.16%	1.06%	0.30%
$\boldsymbol{\theta = 70.3°}$	y_{21}	y_{22}	y_{23}	y_{24}	y_{25}
Maximum error	1.45%	1.67%	1.74%	5.13%	1.17%
Minimum error	0.00%	0.01%	0.00%	0.01%	0.00%

Average error	0.28%	0.17%	0.15%	0.55%	0.19%
Standard deviation	0.29%	0.20%	0.20%	0.87%	0.20%
$\boldsymbol{\theta = 80°}$	y_{31}	y_{32}	y_{33}	y_{34}	y_{35}
Maximum error	2.49%	4.33%	4.21%	4.55%	2.79%
Minimum error	0.00%	0.00%	0.00%	0.00%	0.01%
Average error	0.27%	0.39%	0.38%	0.57%	0.30%
Standard deviation	0.35%	0.63%	0.62%	0.83%	0.39%

In summary, the forward analysis of the present study is quite successful on transversely isotropic thin film systems.

1.4.6 Reverse analysis for current transversely isotropic thin film system

There are various strategies of reverse analysis. Most of them emphasized on finding thin film system properties which give global minimum mismatch between f_{ijk} and y_{ijk}, where the values of y_{ijk} are already known in advance (usually from experiments), and values of f_{ijk} are obtained through polynomial functions been created in the present study. However, few discussed much about how they achieved this objective.

In the present work, given there are 15 polynomial functions, each with 75 terms, that need to be analyzed at the same time, Nelder-Mead Simplex Algorithm was applied to help to find the property combinations with local minimum error, instead of global minimum. Since the obtained polynomial is expected to be close to the analytical solution, blinding pursuit of global minimum is not necessary and inefficient, sometimes may even result in the missing of correct answers. As all solutions with local minimum error have a chance to be the final solution, it's better to find them all. Moreover, this tactic could be helpful when checking the uniqueness of reverse analysis results. A complete reverse analysis flow chart is shown in figure 10.

In table 6, the detailed reverse analysis results were shown for test sample #19. There were total three distinguishable solutions. Apparently, in output II and III, there is some property value exceeding the range greatly, based on which, all analysis was performed, e.g., σ_{fL}/σ_{fT} for output II, E_f, σ_{fL}/σ_{fT} and n for output III. Therefore, output II and III would be eliminated automatically by the reverse analysis steps.

Table 6. Detailed reverse analysis results for test sample with number 19.

#19 Sample	$\boldsymbol{E_f/GPa}$	$\boldsymbol{\sigma_f/MPa}$	$\boldsymbol{E_s/GPa}$	$\boldsymbol{\sigma_{fL}/\sigma_{fT}}$	$\boldsymbol{n}$
Input	225	300	75	1.35	0.05
Output I	241	301	75	1.45	0.04
Output II	167	353	77	*0.57*	0.05
Output III	*407*	437	71	*0.71*	*-0.01*

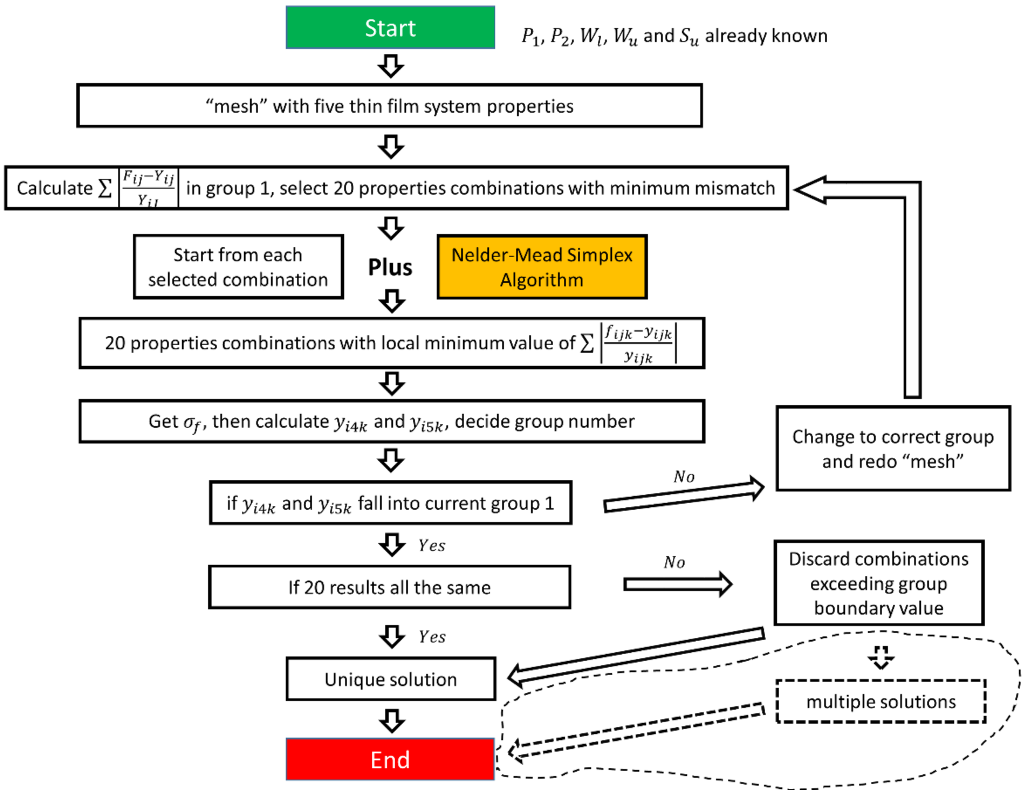

Figure 10. Sehcmetic illustrating reverse analysis flow path.

Obviously, according to the discussions above, the reverse analysis strategy in the present work can save multiple solutions if they do exist. But, by following the steps in the reverse analysis flow chart, all 100 test samples give only one solution at last, that's why the lower right corner part of figure 10 was surrounded by dash lines, which might indicate a very good uniqueness of the relationship between transversely isotropic thin film system properties and characteristic responses on $P-h$ curves, at least in property range of interesting here. The detailed output of all 100 test samples are included in Appendix D. Statistics for all 100 test samples are shown in table 7 and 8. A more intuitive view can be found in figure 11. Evidently, points closer to x axis in figure 11 represent a better predicting result of corresponding property. Most points fall between two dash lines representing positive 10% and negative 10% error respectively, indicated acceptable results of the current reverse analysis method.

Table 7. Statistics absolute errors of reverse analysis results for 100 test samples.

	E_f/GPa	σ_f/MPa	E_s/GPa	σ_{fL}/σ_{fT}	n
Maximum error	19	277	2	0.53	0.09
Minimum error	0	0	0	0	0
Average error	5	8	1	0.07	0.01
Standard deviation	4	42	0	0.09	0.01

Table 8. Statistics percentage errors of reverse analysis results for 100 test samples.

	E_f	σ_f	E_s	σ_{fL}/σ_{fT}	n
Maximum error	19.29%	29.14%	1.70%	45.71%	72.99%
Minimum error	0.01%	0.01%	0.00%	0.32%	0.05%
Average error	2.63%	1.91%	0.33%	6.22%	2.94%
Standard deviation	2.83%	6.10%	0.36%	7.41%	9.16%

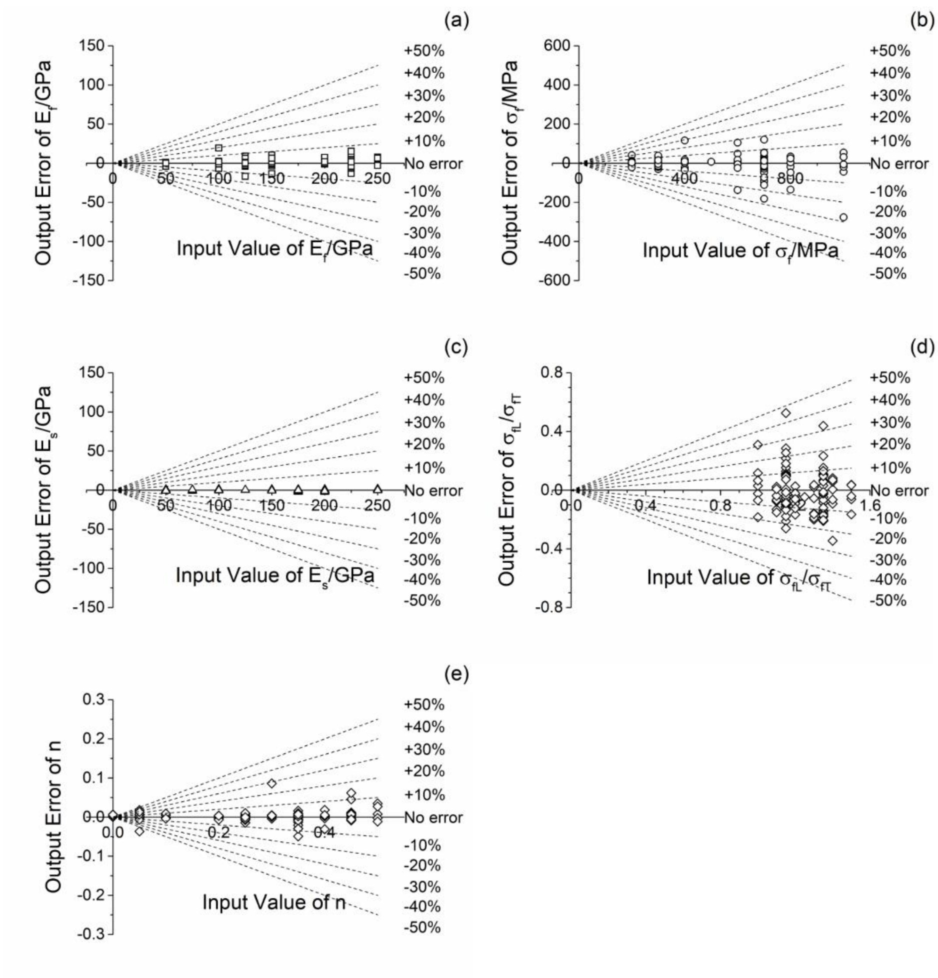

Figure 11. Percentage and absolute errors of reverse analysis results of five properties of all 100 test samples: (a) E_f; (b) σ_f; (c) E_s; (d) σ_{fL}/σ_{fT}; (e) n.

It's also clear from table 8, the average error level for all test samples is below 6.22%. For E_s, the average percentage error is even as small as 0.33% with the average absolute error less than 1 Gpa (Table 7) verified the ability of instrumented indentation method of detecting the properties of the substrate, although indenter would not interact with the substrate directly. The high precision of prediction of E_s might be due to the deep penetration ratio in the present study. Although in table 8, it shows that the maximum percentage error of n is about 73%, it's very clear that all points in figure 11(e) are quite close to the x axis. Such contradiction can be explained with the original input and output data. This phenomenon happened on sample #33, in which, the input value of n was 0.05, and the reverse output value is 0.0135. Even though the absolute error is as small as

0.0365, due to the extremely low input value, the percentage error seems quite significant. The forecasting of anisotropic ratio, σ_{fL}/σ_{fT}, is good for most testing samples, with only 7 of them falling outside $\pm 20\%$ dash lines. Since the indentations were only, and could only be carried out in the out-of-plane direction, results are still acceptable.

1.4.7 Sensitivity of reverse analysis in present study

Artificial $\pm 1\%, \pm 3\%$ and $\pm 5\%$ input error had been imposed to each characteristic response on $P - h$ curves to check the sensitivity of the reverse analysis in the present study. Figure 12 (a) to (c) displays how input errors affect the predicting of E_f. Figure 12 (d) to (f) shows the influence of input errors on σ_f. Figure 12 (g) to (i) shows the influence of input errors on property E_s. Figure 12 (j) to (l) shows the influence of input errors on σ_{fL}/σ_{fT}, while (m) to (o) shows the influence of input errors on n.

Obviously, when input error is less than $\pm 1\%$, reverse analysis outcomes are still very good, which means reverse analysis is still reliable at this stage. When input errors increase to $\pm 3\%$, the average error of reverse analysis grows by about 10%. As continued increasing the input error to $\pm 5\%$, the error of the prediction of σ_f reaches a level of 40%, while the result of predicting E_f and E_s is still acceptable. σ_{fL}/σ_{fT} is most sensitive to input errors while E_s is almost not sensitive to input errors. Figure 12 (g) to (i) shows that even when input errors are as large as $\pm 5\%$, the reverse analysis error of E_s is always less than 8%. Meanwhile, it's very clear that Y_{i5}, i.e. S_{max}, has the most dominant influence on the predicting of all properties. Forces responses, Y_{i1} and Y_{i2} have stronger effect than work responses Y_{i3} and Y_{i4}. Additionally, responses of indenter $80°$ can affect the reverse analysis more intensively than indenter $60°$ and $70.3°$

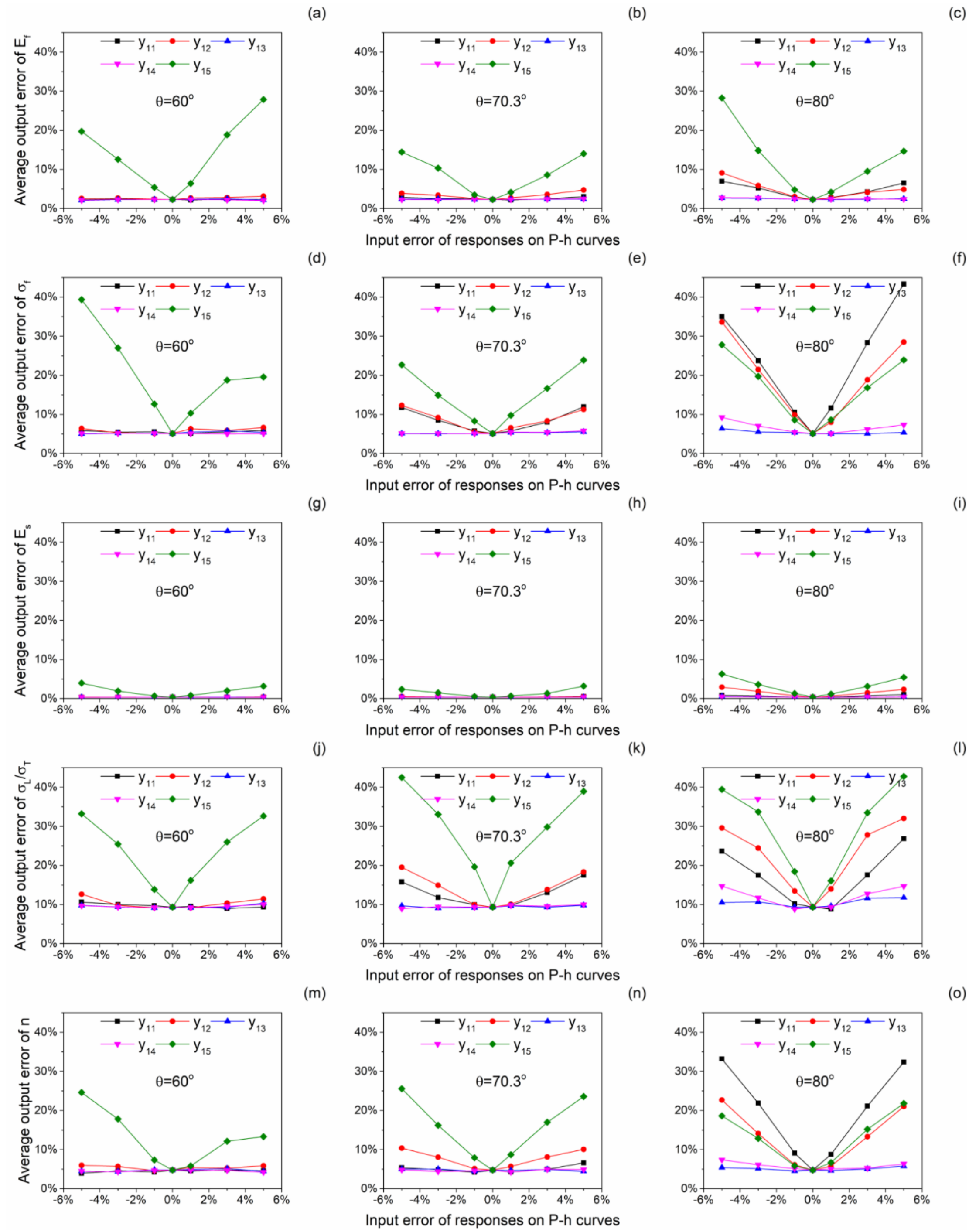

Figure 12. Sensitivity of system properties for the reverse analysis in present study. (a)-(c) E_f; (d)-(f) σ_f; (g)-(i) E_s; (j)-(l) σ_{fL}/σ_{fT}; (m)-(o) n.

1.5 Conclusions

Due to the increasing applications of instrumented indentation method for solving complex and practical problems, here is a strong motivation for improving its scope, from bulk to thin film, from isotropic to anisotropic. Due to the complexity of stress status under indenter tips and operability of experiments, numerous studies have focused on developing numerical models. Due to the computational cost considerations, many of the numerical studies reported thus far have been able to model only material systems with small number of properties. Little information about the robustness, sensitivity or uniqueness of instrumented indentation method on material systems with large number of properties was at present available. Hence, present study focused on developing numerical models that capture the $P-h$ curves for transversely isotropic material systems with large number of properties. Optimized forward and reverse analysis methods were carried out on explaining simulation results. The determination of substrate properties through instrumented indentation method was also discussed. The main conclusions obtained from the present study are given below.

1. The influence from transversely isotropic elasticity of thin film on $P-h$ curves can be ignored.

2. Dimensionless relationships between a large number of material properties and a larger number of characteristic responses on $P-h$ curves were created. Forward and reverse analysis were carried out based on above relationships. The accuracy of both forward and reverse analysis are acceptable.

3. Reverse analysis results are still acceptable as input error is less than $\pm 3\%$.

4. Unique solution was found for all 100 test samples indicate a possible uniqueness of instrumented indentation method when material properties were restricted in the range of interesting.

5. Instrumented indentation method can be applied to predicate thin film properties precisely if penetration ratio is high enough.

Chapter 2: Computational Modeling of Flow Through Porous Media

2.1 Introduction

Porous media are widely found in nature word and modern industry [51-54]. Understanding flow characteristics through porous media is important for several practical applications from water filtration [55, 56], and chemical separation [57] to heat exchangers [58-60] and biological systems [61-63]. For example, within the context of heat exchangers, it is well known that the porous regenerator, is one of the most essential and important parts in Sterling cycle machines and cogeneration systems. Therefore, considerable research work has been done in order to understand the pressure losses and heat transfer characteristics of the regenerator which directly impact the efficiency of the heat engine [54, 64-68].

The nature of the material used and the geometry of the porosity present in the regenerator play important roles in determining the efficiency with which heat is transferred from the working fluid to the regenerator and the *vice-versa* [54]. Experimental, theoretical and numerical studies have been carried out on a variety of porous regenerators such as metal-felt matrix, sponge metal and fiber woven screen matrices in order to identify a regenerator that would provide the ideal combination of characteristics, i.e., maximizing heat transfer while minimizing pressure losses, as a working fluid flows across the porous medium. Kays and London [54] emphasized that for low-density fluid, like gas, the mechanical energy expended in overcoming friction power could have the same magnitude as the transferred heat. However, it’s well known the mechanical energy is more valuable than it’s in heat. Thus, within the context of Stirling engines with the gaseous fluid, there is a strong motivation to understand the pressure drop characteristics as a working gas flows through the porous media.

A porous medium comprised of a fiber mesh in a woven screen format, hereafter referred to as a woven medium, is the most popular configuration of the Sterling engine regenerator [69]. A single layer of woven screen or woven matrix is as shown in figure 13. It consists of two groups of fibers which are perpendicular to each other, and are interwoven, namely the warp and weft, respectively [70]. The approximately square-shaped flow channel that is surrounded by fibers is referred to an "open-pore" as shown in figure 13, while the entire structure (that is comprised of one set of warp and weft fibers) is designated as a single-layered, woven matrix with a 4 x 4 open-pores porous structure.

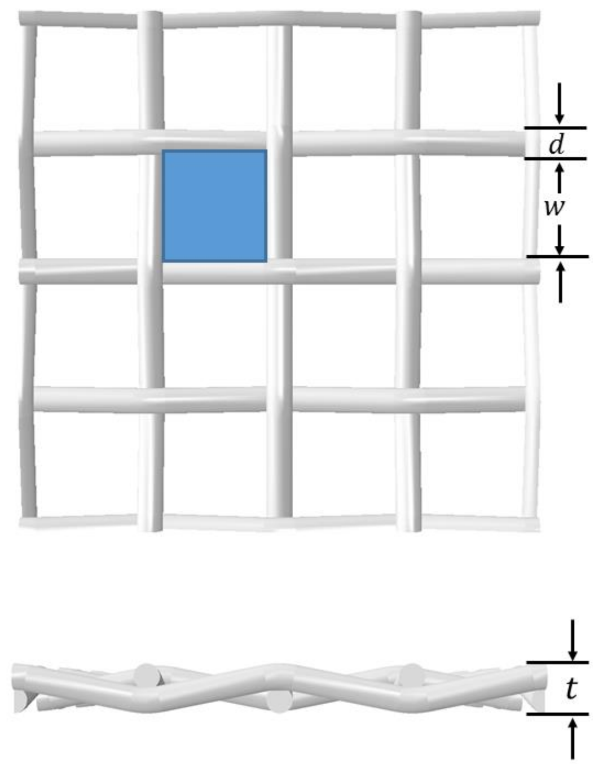

Figure 13. Schematic illustrating a 4 x 4 open porous section in a single layer woven matrix structure where d, w and t represent the fiber diameter, open pore size and the layer thickness, respectively, where $t = 2d$.

Fibers are not necessarily well arranged in a porous medium. A porous medium with randomly stacked fibers, as shown in figure 14, hereafter referred to as a random stacked medium, is also of interest and were carefully studied in present work.

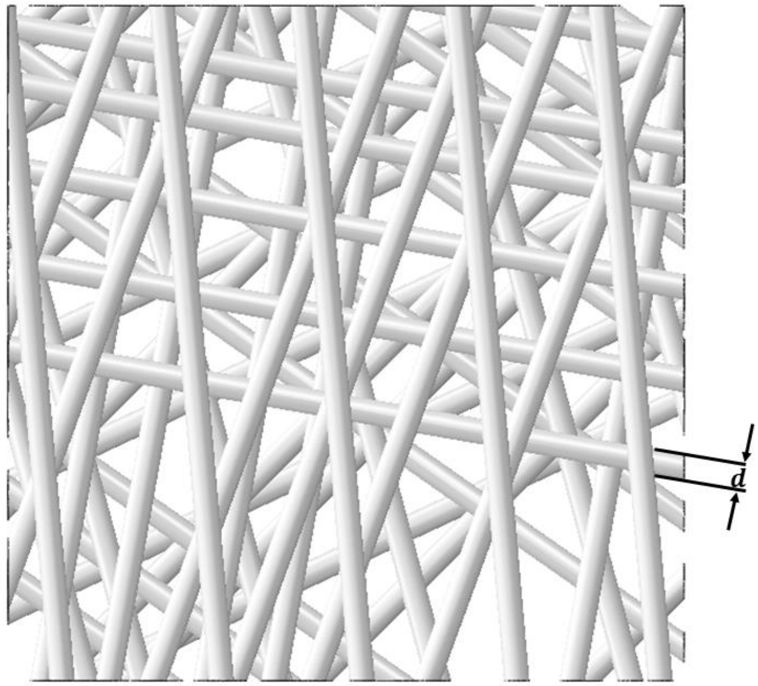

Figure 14. Schematic illustrating a porous medium (a random stacked medium) configure with randomly stacked fibers.

Although several studies have focused on developing numerical models to characterize the fluid flow behavior through woven networks or screens, [59, 71-73], might due to the limitations of computational capability or the difficulties of creating large scale models, many of these models have modeled fluid flow across small cross-sections (usually no more than a 3 x 3 open porous structure) of the woven network and over relatively shallow depths (usually no more than 6 layers). Given that the mechanics of fluid flow across a woven matrix structure tends to be fairly complex, it is unclear if the relatively small numerical models developed thus far, accurately capture the characteristics of fluid flow in woven matrix structures. Hence, the main objectives of the present study are:

(i) To develop numerical models that will capture the fluid flow characteristics through a porous medium over large physical size;

(ii) To assess the effect of defects in the lay-up of woven networks on the fluid flow characteristics;

(iii) To compare the pressure loss between woven medium and random stacked medium as gas flows through them;

(iv) To compare the results of the numerical models with experiments;

(v) To optimize the configures of a porous medium in order to reduce the pressure loss.

The structure of this chapter is organized as follows. Background information and a summary of prior work done in predicting important characteristics of flow through a porous media such as pressure drops and friction factors are presented in Section 2.2. The experimental set-up used to characterize flow through woven matrix porous media is presented in Section 2.3 The details of the numerical model developed in the present study are highlighted in Section 2.4. The results obtained from the present study are discussed in Section 2.5 and key conclusions from the present work are summarized in Section 2.6.

2.2 Background – Pressure drops and friction factors in porous media

Cauchy momentum equation (equation 25) is a vector partial differential equation describing the micro mechanical balance of viscous fluid [74], where ρ is the density of the fluid, t is the time, $\boldsymbol{u}$ is the velocity vector of fluid, p is the pressure, $\boldsymbol{I}$ is the identity matrix, $\boldsymbol{\tau}$ is the shear stress tensor, $\boldsymbol{g}$ represents the body force.

$$\frac{\partial}{\partial t}(\rho \boldsymbol{u}) + \nabla \cdot (\rho \boldsymbol{u} \times \boldsymbol{u}) = -\nabla p \boldsymbol{I} + \nabla \boldsymbol{\tau} + \rho \boldsymbol{g} \qquad \text{Eq (25)}$$

Stokes's stress constitutive equation (equation 26) defined the relationship between the shear stress, $\boldsymbol{\tau}$, dynamic viscosity μ and velocity gradient of fluid when the flowing fluid is incompressible [75].

$$\boldsymbol{\tau} = \mu(\nabla \boldsymbol{u} + \nabla \boldsymbol{u}^T) \qquad \text{Eq (26)}$$

Now, by joining equation 25 and equation 26, it's not difficult to obtain the very famous Navier-Stokes equation which controlled the behavior of incompressible Newtonian fluid as following [76]:

$$\frac{\partial \boldsymbol{u}}{\partial \mathrm{t}} + (\boldsymbol{u} \cdot \nabla)\boldsymbol{u} - \frac{\mu}{\rho}\nabla^2 \boldsymbol{u} = -\frac{1}{\rho}\nabla p + \boldsymbol{g} \qquad \text{Eq (27)}$$

In addition to equation 27, continuity equation for the incompressible fluid (equation 28) is also required to attain an analytical solution finally [75]. However, the analytical solution is only found when boundary and initial conditions are extremely simple. In other words, it's almost impossible to get an analytical solution for gas or liquid flowing through porous media.

$$\nabla \cdot \boldsymbol{u} = 0 \qquad \text{Eq (28)}$$

Therefore, plentiful experimental studies have been carried out initially. Kozeny assumed that the bed filled with fine powders is equivalent to a group of parallel and equal-sized channels and firstly developed the following equation of describing the relationship between the viscosity of the fluid, μ, the frontal velocity of fluid, u_{in}, the thickness of the porous media in the direction of fluid flow, L, the porosity of the media, β, specific surface of solid, S_v, and the pressure loss as fluid flowing through the porous media, ΔP, at low flow rates [77].

$$S_v = \left(\frac{1}{5}\frac{\Delta P}{\mu u_{in}}\frac{1}{L}\frac{\beta^3}{(1-\beta)^2}\right)^{1/2} \qquad \text{Eq (29)}$$

Following Stanton and Pannell's [78] approach towards understanding the characteristics of fluid flow through a pipe, Blake [79] analyzed the problem of fluid flow through a porous medium comprised of particulates and obtained a relationship between two dimensionless groups: $\frac{\Delta P}{\rho u_{in}^2}\frac{D_p}{L}\frac{\beta^3}{1-\beta}$ and $\frac{D_p \rho u_{in}}{\mu(1-\beta)}$, where D_p is the diameter of the solid particle within the porous media. Chilton [80] later proposed equation 30, also known as a correlation, to calculate the pressure loss, ΔP, as the fluid flowing through packed columns at high flow rate and introduced the definition of friction factor, C_f.

$$\Delta P = 2C_f''' \rho {u_{in}}^2 / D_c \qquad \text{Eq (30)}$$

where D_c is the diameter of the column and C_f''' depends on Reynolds number Re. Leva and Grummer [81] further modified equation 30 by including the effect of porosity of the media of the factor of $\frac{\beta^m}{(1-\beta)^2}$, where m is either 1 or 2 in value. Based on former work and experimental data, Ergun postulated that the pressure drop observed as the fluid flows through a porous medium was due to both kinetic and viscous effects [82] and proposed an important and comprehensive relationship as given below in Equation 31 which is suggested to work at both low and high flow rate:

$$\Delta P/L = 150\frac{(1-\beta)^2}{\beta^3}\frac{\mu\bar{u}}{D_p^2} + 1.75\frac{1-\beta}{\beta^3}\frac{G\bar{u}}{D_p} \qquad \text{Eq (31)}$$

where, $\bar{u}$ stands for the superficial velocity that is obtained by considering the mean pressure of the fluid at the entrance and the exit regions, and G is the mass flow rate. The differential form of the Ergun's Equation (equation 31) is given below in Equation 32 as:

$$dP/dL = 2A\frac{(1-\beta)^2}{\beta^3}\mu u_{in} S_v^2 + \frac{B}{8}\frac{1-\beta}{\beta^3}\rho u_{in}^2 S_v \qquad \text{Eq (32)}$$

where, A and B are coefficients that are determined experimentally and S_v represents the specific surface area of the solid particles, i.e., the ratio of the surface area exposed to the flowing fluid to the volume of the solid particles [58]. Ergun also derived an expression for the friction factor, C_f'', as the ratio of the total energy loss to kinetic energy loss which is analogous to the Darcy friction factor [82]:

$$C_f'' = \frac{150(1-\beta)}{Re''} + 1.75 \qquad \text{Eq (33)}$$

where the Reynold number, Re'', is defined as:

$$Re'' = \frac{\rho}{\mu} u_{in} D_p \qquad \text{Eq (34)}$$

Sodré and Parise [69] applied Ergun's law [82] of pressure losses for a porous medium system that is comprised of an annular bed of woven screens and proposed that the modified friction factor (not considering the boundary wall effect), C_f', could be defined as:

$$C_f' = \frac{a_1(1-\beta)}{R_e'} + a_2 \qquad \text{Eq (35)}$$

where coefficients a_1 and a_2 were identified, respectively, as 100 and 0.73. In equation 35, R_e' is the Reynolds number for porous media made up of woven screens, which is based on the wire diameter, d:

$$Re' = \frac{\rho}{\mu} u_{in} d \qquad \text{Eq (36)}$$

The pressure drop that occurs as the fluid flows through the porous media is then given in following correlation as:

$$\Delta P = \frac{C_f' \rho L u_{in}^2}{d} \frac{(1-\beta)}{\beta^3} \qquad \text{Eq (37)}$$

According to Kays and London's [54] and Gedeon's [83] research, the prediction of pressure drops in fluid flow across a porous medium could be further simplified by using another definition of the Reynolds number using the hydraulic diameter as given in equation 38:

$$Re = \frac{\rho}{\mu} u_m d_h \qquad \text{Eq (38)}$$

In equation 38, the mean flow velocity u_m is obtain by dividing the frontal velocity u_{in} by porosity β and d_h stands for the hydraulic diameter [84-86] which is defined as:

$$d_h = \frac{4\beta}{S_v(1-\beta)} \qquad \text{Eq (39)}$$

For a woven medium made up of fibers with a circular cross-section, S_v is equal to $\frac{4}{d}$. By substituting D_p with d and $\bar{u}$ with u_{in}, and rearranging equation 31, the pressure losses expected across the porous media can be obtained using equation 40 as:

$$\Delta P = C_f \frac{\rho}{2} \frac{L}{d_h} {u_m}^2 \qquad \text{Eq (40)}$$

Equation 40 has also been widely accepted and adopted in recent work in the field [59, 87]. Thus, it is evident from equation 40 that it would be easy to predict the pressure losses if the friction coefficient C_f is known *a priori*. In general, the friction factor C_f is primarily a function of the Reynolds number Re. The exact form and specific coefficients in the expression for C_f mainly depend on the porosity geometry of the porous media [58, 59, 65, 83]. Essentially, if C_f in equation 40 has the same form as in equation 35 i.e., with two parameters in the expression, it can be found that equations 37 and equation 40 will also have the same form but might be with slight differences in the coefficients.

Several forms have been identified for the friction coefficient C_f in previous studies. Jones [67] presented an expression for the friction factor C_f in the form $a_1 Re^m$. In the specific regime of laminar flow, $m = -1$, i.e., $C_f = a_1/R_e$. Bernd [88] proposed that there are two components to the pressure drops in a woven matrix medium, *form drag*, ΔP_{fd}, and *skin friction*, ΔP_{sf}, such that the total pressure drop ΔP is given as:

$$\Delta P = \Delta P_{fd} + \Delta P_{sf} \qquad \text{Eq (41)}$$

where:

$$\begin{cases} \Delta P_{fd} = C_{fd}\dfrac{\rho}{2}u_m^2 \\ \Delta P_{sf} = C_{sf}\dfrac{\rho}{2}u_m^2 \end{cases} \quad \text{Eq (42)}$$

Bernd [89] further reasoned that since ΔP_{fd} is not a boundary layer phenomenon, C_{fd} should not be a function of the Reynolds number while C_{sf} is proportional to $1/Re$. Also, Bernd [89] (and Tanaka [84]) thus suggested the following form for the friction coefficient C_f:

$$C_f = a_1/Re + a_2 \quad \text{Eq (43)}$$

Armour and Cannon [65] obtained similar correlations for the friction factor by combining models of flow past submerged spheres and capillary tube-bundles at low and high flow velocity regimes, respectively. Macdonald *et al*. [66] verified equation 43 with a large database of experimental results available in the literature. Gedeon and Wood [83] later found that equation 43 can better track observed experimental results, esp., for flows with higher Reynolds numbers, by introducing a third parameter and presented a modified version of equation 43 for the friction factor as follows:

$$C_f = a_1/Re + a_2 Re^{a_3} \quad \text{Eq (44)}$$

In general, the numerical values of the coefficients - a_1, a_2 and a_3, are affected by the geometry of the porous media (or weave style) [58, 65], wall effects [69, 90], oscillating density and oscillating pressures [67], compressibility of the fluid and the oscillating characteristics of the frontal velocity [68, 84].

Recently, several studies have invoked numerical methods to characterize the friction factor C_f, quantify the pressure losses and to obtain a mechanistic understanding of pressure loss phenomenon in flow through the porous medium [59, 70-73, 91-96]. Green *et al.* [73] researched the effects of boundary conditions and geometry of the porosity on flow characteristics in porous media. Costa *et al.* [59] focused on the wound woven configuration and identified values of a_1, a_2 and a_3, to predict the pressure loss using the correlation as equation 40. Xueliang *et al*. [71] created five gradual converging-diverging ducts to understand the flow behavior and found that a woven matrix with higher porosity and smaller thickness may result in a larger dynamic through-thickness permeability. Ponzio *et al*. [72] considered a specific screen aspect ratio and two different screen orientations (0° and 45°) with respect to the main flow direction.

However, much of the models developed thus far relied on relatively smaller model sizes. Hence, larger models are developed in the present study to obtain a better insight into the flow behavior through woven matrix porous medium together with random stacked porous medium. The details of the experimental set-up used to characterize the flow behavior through woven medium are presented in the following Section 2.3.

2.3 Experiment Set-up for Characterizing Flow through Woven Matrix Porous Media

The experiments are prepared by Hanfei Chen from the group advised by Professor Longtin, J. P. from the Department of Mechanical. The experimental set-up designed to measure the frontal flow velocity u_{in} and pressure drop ΔP across the porous media is shown in figure 15. The main portion of the test rig is a 1 inch (2.54 cm) inner diameter PVC pipe. The woven matrix porous media samples, with wire diameter as 56 μm, are cut into 2.54 cm diameter cylinders with different lengths (greater than half 1.27 cm) and placed inside the PVC test section. Nitrogen gas from pressurized cylinders is passed through a regulator (not shown) and then introduced to the PVC test section. The flow is from left to right.

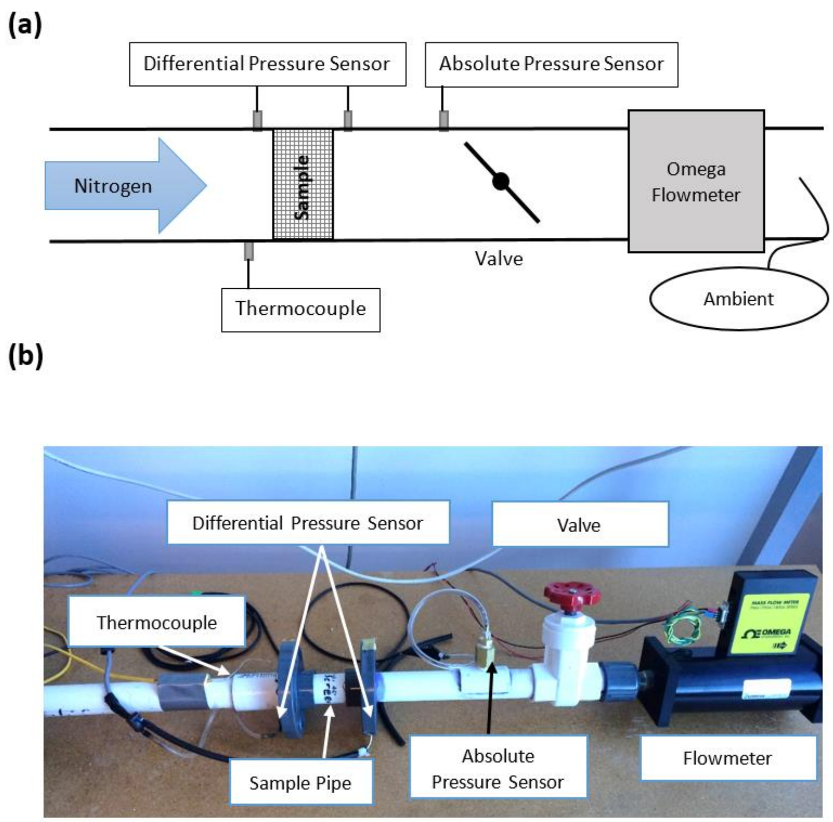

Figure 15. (a) Schematic and (b) a photograph of the experimental set-up used for measuring pressure drops in woven matrix porous media.

The experimental pressure loss, ΔP_d, across the porous media sample is measured using a high-precision differential pressure sensor (Freescale Semiconductor, MPX4250DP). A k-type thermocouple (Omega Engineering) is used to measure the nitrogen gas temperature just upstream of the sample. The absolute gas pressure, P_a, downstream of the sample is measured with an absolute pressure sensor (Freescale Semiconductor, MPX4205AP), which is required to determine the density of the gas both upstream and downstream of the sample. A PVC throttling valve is used to adjust the flow rate for different tests, and the flow itself is measured using an Omega flowmeter. The details for each sensor are listed in table 9.

Table 9. Sensor Information

Sensor	Model	Range	Accuracy
Differential pressure sensor	MPX4250DP	0 – 250 KPa	± 3.45 KPa
Absolute pressure sensor	MPX4205AP	20 – 250 KPa	± 0.075 KPa
Flowmeter	FMA1700A/1800A	0 – 500 L/min	± 7.5 L/min
Thermocouple	K-type	0 – 1000 °C	± 1°C

To minimize density effects, the absolute pressure at the middle point of the sample, P_c, is maintained at a constant value by adjusting the nitrogen flow with the tank regulator and the back pressure behind the sample with the throttling valve. The pressure at the center of the regenerator sample can be determined by:

$$P_c = P_a + \frac{\Delta P_d}{2} \quad \text{Eq (45)}$$

For example, at lower flow rates, the throttling valve will be slightly closed to ensure that the pressure at the center of the sample remains constant. If this were not done, the absolute pressure of the nitrogen gas would vary considerably as the flow rate is changed. Since the gas properties are pressure-dependent, this would introduce error into the final results. The above procedure is a simple yet effective means to minimize this error source.

A photograph of the completed test assembly is shown in figure 15. All sensor data are recorded using a Keithley Model 2000 high-resolution digital multimeter. The multimeter is connected by Ethernet to a laptop PC running ExcelLINX, which transfers the measured data to Microsoft Excel. Measurements of all sensor data are taken once per second.

2.4 Numerical Modeling

2.4.1 Rationale for modeling woven networks with square fibers

In general, considerable efforts are needed for creating numerical models of woven fiber networks with circularly shaped fibers as the curved surfaces typically require a careful design of the element mesh to capture the geometrical details of the curved surfaces in a reasonably accurate manner. On the other-hand, developing numerical models of woven networks with square fibers tend to be much simpler as the mesh design for systems with fewer curved surfaces is much less cumbersome. Thirdly, it's difficult to evaluate the accurate porosity of a random stacked model with circular fibers. Especially, for numerical models that capture physically large woven networks, the efforts needed for creating models with flat surfaces is substantially less than those needed for models with curved surfaces.

Hence, the present study is focused on developing an efficient, yet accurate method of building a numerical model of woven networks and random stacked media without curved surfaces, and checking the feasibility of utilizing such a model to understand flow behavior in physically large systems firstly. For woven matrix models, the two main sources of curved surfaces in the numerical model are the circular cross-section of the fiber itself and the bending of the fibers as the fibers cross over each other. The former can be addressed with square cross-section fibers (figure 16(a), (b)), while the latter is addressed by introducing a flat and step-type configuration in the fiber cross-over regions (figure 16(c), (d)). For random stacked media, curved surfaces are only from the exterior appearances of these fibers. That is to say, by simply replacing the circular fibers with square cross-section fibers, all curved surfaces could be eliminated easily. Consequently, establishing that equations 38-44 are applicable to both circular and square cross-section fibers, at least within the Reynolds number range of interest, is required.

Gedeon [87] observed out that if non-circular fibers are all oriented perpendicular to the axial flow direction, then the definition of hydraulic diameter and the friction factor correlations should still hold. Armour and Cannon [65] found that in the low Reynolds number regime, the friction factor, C_f, is not sensitive to the specific configuration of the woven matrix. In addition, Macdonald *et al.* [66] argued that the shape and size distribution irregularity of media particles only increased the difficulty of calculating the characteristic length, but did not change the form of the expression for C_f. Thus, it is reasonable to expect that the change of cross-sectional shape of fibers will not affect the overall flow characteristics in a significant manner.

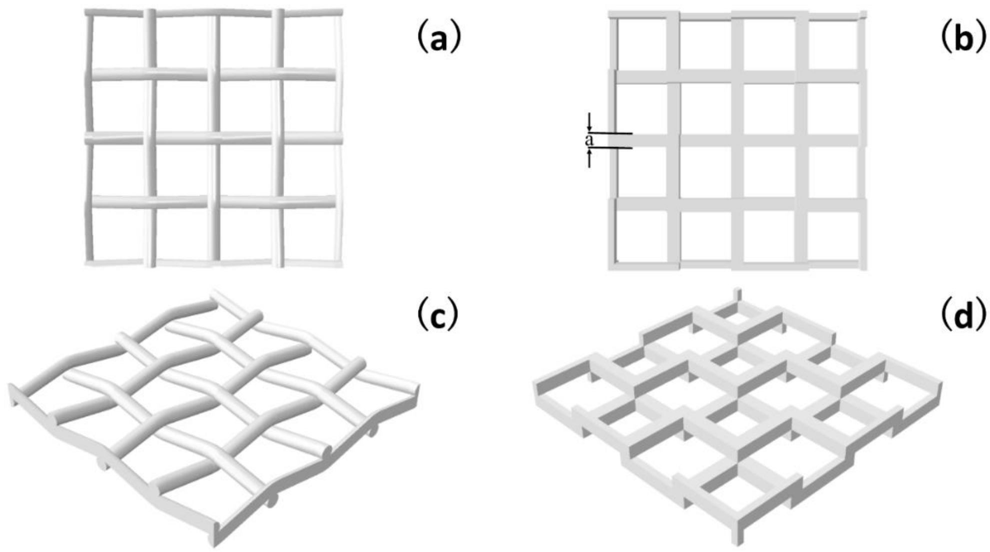

Figure 16. Schematics illustrating fibers with circular cross-sections (a) and square cross-sections (b), and a represents the thickness of square crossing sectional fiber. The woven matrix with fiber bending (c) is modeled with a woven matrix with flat fibers with a step-type configuration in the cross-over regions (d).

In principle, fibers with other cross-sectional shapes, like triangular and polygonal, are also candidates for the present study. However, due to its operational convenience, square shaped fibers are selected for this study. The most important geometric factors, d_h, associated with the fiber shape, S_v, as defined in equations 39 are equivalent for fibers with circular and square cross-sections. Hence, the Reynolds number predicted by equation 38 will be the same for flow through a woven matrix or a random stacked media with square fibers if the fiber diameter, d, is replaced with the fiber thickness, a, provided the value of porosity, β, remains unchanged.

Thus, in the present work, it is expected that flow through a woven medium with square fibers will exhibit a relationship between the Reynold number, Re, and the frontal flow velocity, u_{in}, that would be the same as in the case of flow through a woven matrix with circular fibers and the same should be true for random stacked media. By rewriting equation 38, as:

$$Re = \frac{\rho u_{in}}{\mu}\frac{d_h}{\beta} \qquad \text{Eq (46)}$$

information about the fluid ($\frac{\rho u_{in}}{\mu}$) and the woven media ($\frac{d_h}{\beta}$) can be explicitly identified. In the present work, while developing the numerical model, care has been taken to ensure that the model accurately captures the geometric parameters of the woven media, i.e., the hydraulic diameter, d_h, and the porosity, β, respectively, in a real experimental set-up (and not just the ratio $\frac{d_h}{\beta}$). To preserve the 80% porosity of the original circular-wire mesh, the open pore-size in the numerical model is increased to 224 μm over the original open-pore size of 198 μm in the circular-wire mesh (Figure 17).

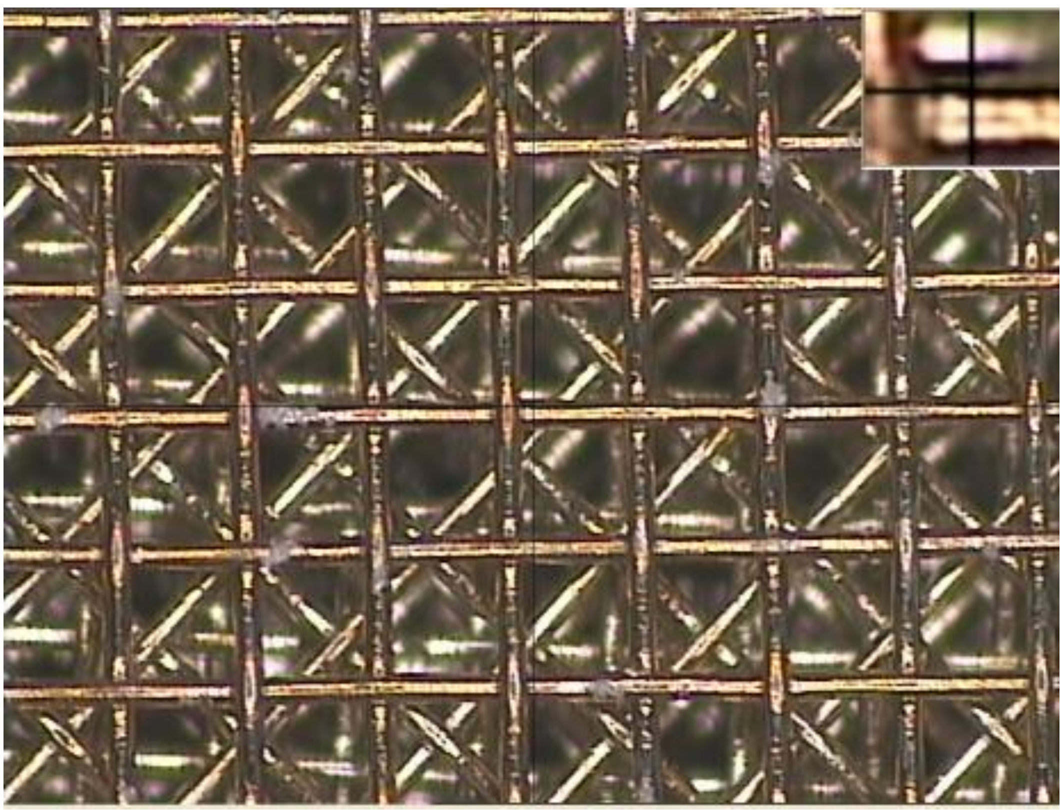

Figure 17. Optimal micrograph of a woven matrix open porous structure used in the experiments.

2.4.2 Numerical models for flow through woven matrix and random stacked media with square shaped fibers

Numerical models are developed to capture the flow characteristics through the porous media. Abaqus CFD version 6.14 was selected as the pre-processor, solver and post-processor. Dry nitrogen was used as the working fluid, as this gas is inexpensive and readily available for the experimental testing reported later.

For woven matrices, square crossing sectional fibers with six different thickness (40μm, 56μm, 60μm, 80μm, 110μm and 140μm) were woven into screens with different open size, so as to achieve four distinguished porosity, i.e., 45%, 60%, 75% and 80%. Fine woven matrices were, then, placed together to form a regenerator sample following the sequence as shown in figure 18. Alternating layers were rotated 45 degrees relative to the previous layer just as observed in experiments (figure 17), with the axis of rotation located at the geometric center.

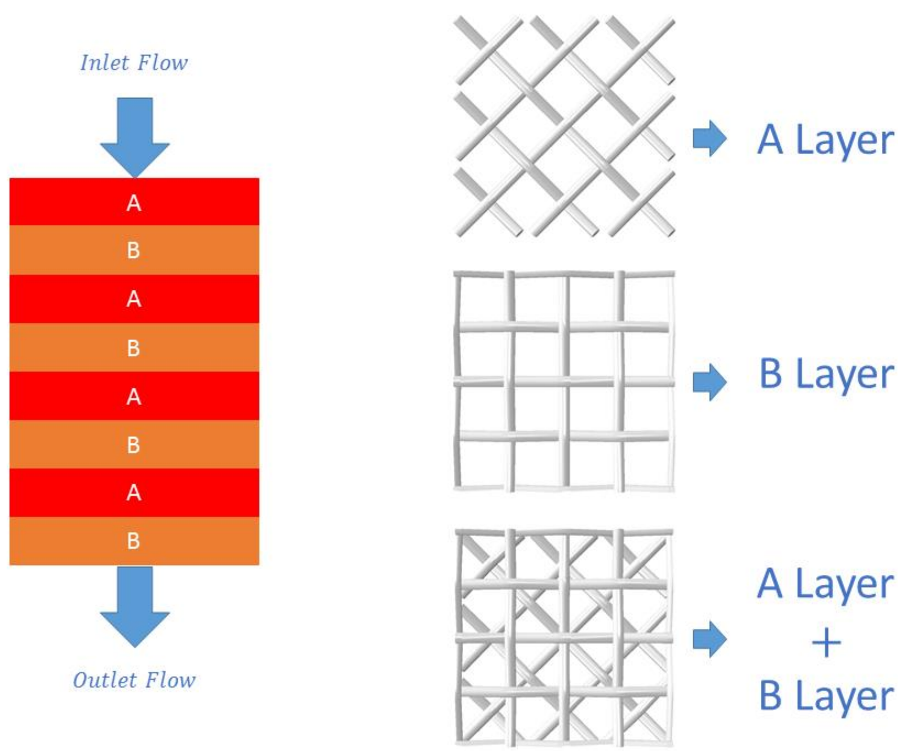

Figure 18. Schematics illustrating the spatial orientation and sequence of woven matrices.

For random stacked media, fiber with and only with the thickness a as $56\mu m$ was applied. The sample porosity was fixed at 80% while the sample thickness was either 8 times or 80 times the thickness of fibers. To be more specific, fibers, in random stacked media, were not completely distributed by random. Fibers could only extend in the plane perpendicular to the direction of flow. And at a certain fiber layer (for differentiating the matrix layer), all fibers were restricted to be parallel to each other (Figure 19). The configures of random stacked medium were generated automatically by Python programs.

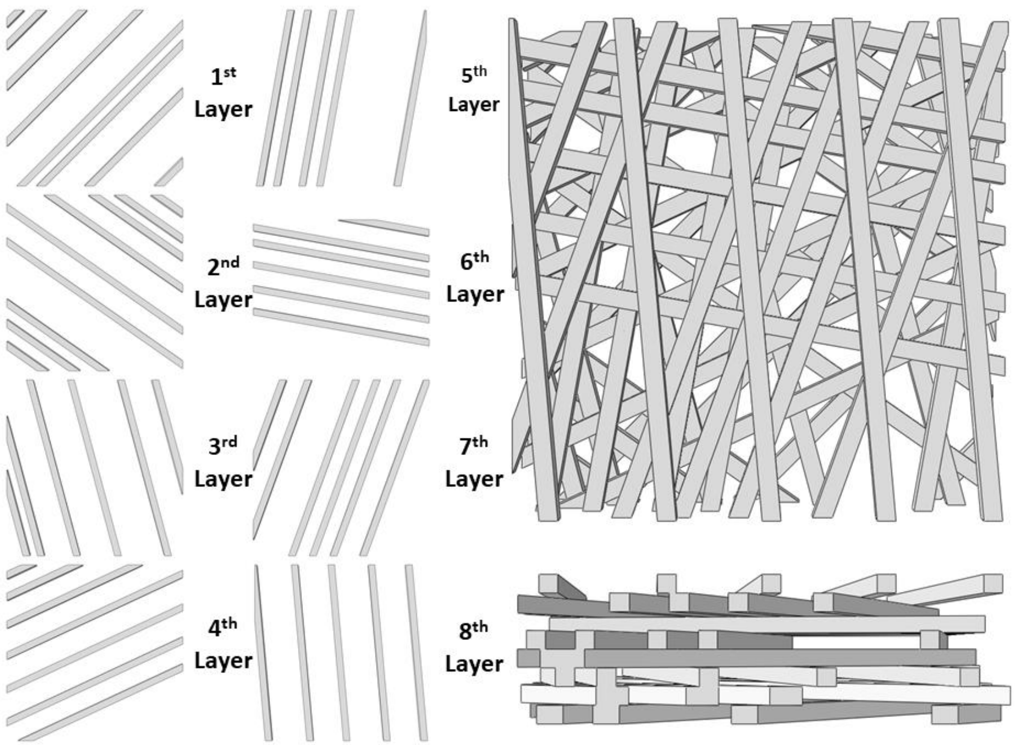

Figure 19. Schematics demonstrating a porous media contains eight layers of randomly distributed fibers.

The complete fluid space consists of three parts: upstream, midstream (shaped according to the configure of the porous media), and downstream (Figure 20). The borders between the midstream and the upstream and downstream regions are formed by the top and bottom surfaces of the porous media, respectively. The depth of the fluid in the upstream and downstream sections are set to 5 and 10 times the thickness of the midstream section, to eliminate flow-reversal effects at the inlet and the outlet boundaries [59].

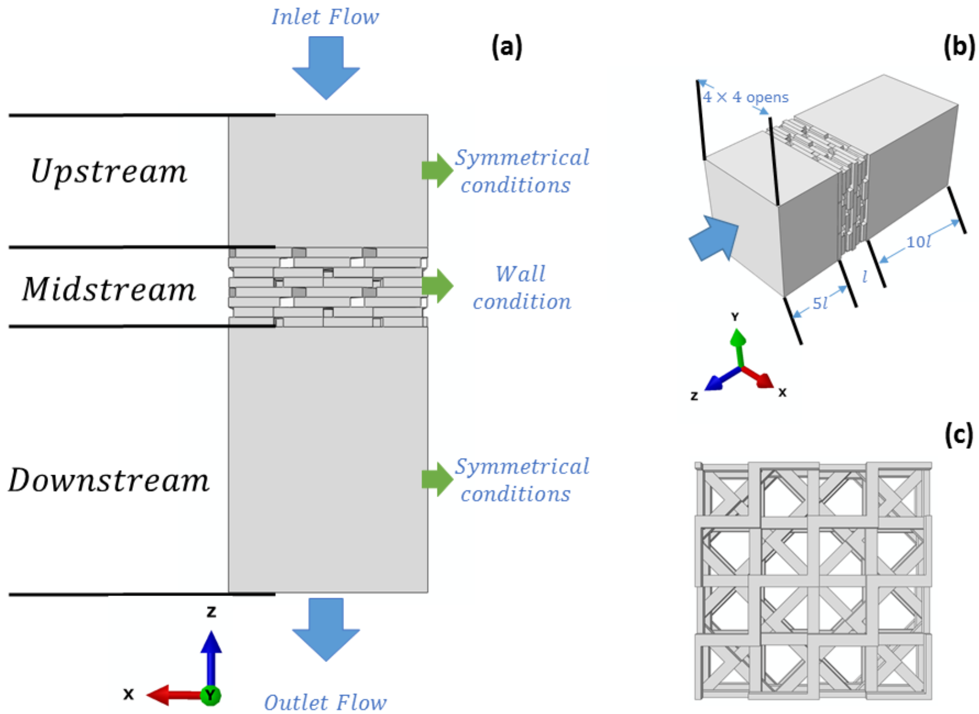

Figure 20. (a, b, c) The geometric features of a numerical model developed in the present study to capture the flow behavior through a 4 x 4 open porous section of a woven matrix structure (4-layer model).

The flow behavior through a woven matrix medium was captured by modeling the fluid part as a representative volume (mid-stream part) of the woven matrices that are comprised of a certain number of open porous section in the in-plane (XY plane) direction and a certain number of screen layers in the out-of-plane direction, i.e., through-thickness direction (Z direction). The specific size of representative volume depended on several factors: fiber thickness, a, media porosity, β, and purpose of the model. Because of the alternative high-low asymmetry of the weave steps, at least *four* layers (180 degrees rotation), i.e., 8 times the thickness of fiber, were required before the pattern repeats. A model with up to 110 matrix layers was created to study the size effects in Z direction (figure 20). The sectional size in XY plane varied from 580 µm $\times$ 580 µm to 2240 µm $\times$ 2240 µm. A range of flow velocities from 0.06 m/s to 40 m/s was modeled. The maximum Reynolds number was 262 as the maximum Mach number is 0.117.

The representative volume of the middle fluid part for the random stacked media models has physical dimensions of 1500 µm × 1500 µm in the in-plane direction and from 0.448 to 4.48

mm in the through-thickness direction. The frontal velocities, u_{in}, were set to be 1.08m/s, 2.35m/s, 4.18m/s and 8.27m/s and the corresponding values of Reynold number, *Re*, were 19.8, 43.6, 78.4 and 163.3 respectively.

Costa [59] suggested that turbulence should be included in a model when the Reynolds number is larger than 160. However, Dybbs and Edwards [97] suggested that the flow is expected to be laminar for Reynolds numbers between 10 and 175 while the range between 175 and 250 is 'separated' laminar flow. Since most of the simulation cases in the present study cover the laminar flow regime, the gas flow is taken to be a viscous, Newtonian, incompressible flow with laminar flow behavior. Thus, the incompressible Naiver-Stokes equation (equation 27) governs the behavior of nitrogen and are solved based on a hybrid finite-volume/ finite-element method. The viscosity of nitrogen was taken to be constant at 1.74×10^{-5} Pa · s, while its density was allowed to vary according to the ideal gas law based on the absolute pressure at the middle point of the experimental sample, P_c, but still stay unchangeable during the simulation process. The boundary conditions invoked in the numerical models are summarized below (figure 20):

1. At the inlet: velocity boundary, $u_x = u_y = 0; u_z = u_{in}$;
2. At the outlet: pressure boundary, $P_{out} = 1\ bar$ or P_c (if data available);
3. At the side faces: symmetric boundary conditions are used with the normal velocity and the velocity gradient with each side face being set to zero;
4. At fiber surface: no-slip wall boundary conditions are used for the fluid-fiber interface.

The linear convergence limit was 10^{-5} and the convergence-checking frequency was set to two iterations which are default settings in Abaqus. The present study is focused on steady inlet flows. The characteristics associated with oscillating flow will be discussed in a future study.

Tetrahedral elements were used to model the fluid in the present study. Figure 21 presents the details of the mesh generated to capture the fluid part of the simulation. The fluid part of the model was filled with unstructured, but regular mesh. The total number of elements varies from 0.6 M to 16 M, mainly depending on the number of fiber layers modeled.

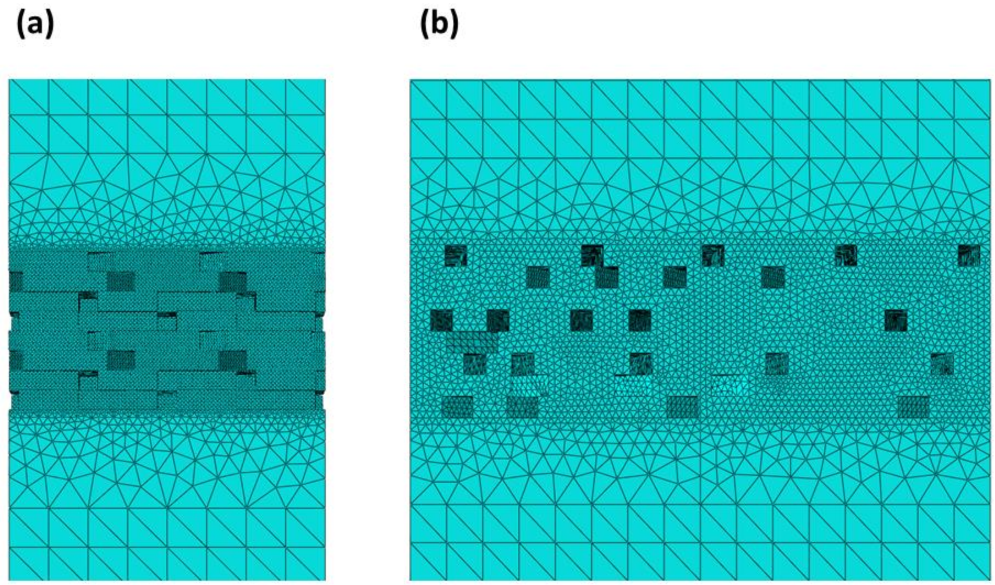

Figure 21. Schematics illustrating mesh details used to represent the fluid part of the model: (a) a 4-matrix-layer with 4 x 4 opens woven matrix model; (b) an 8-fiber-layer random stacked medium model.

In order to assess the trade-off between accuracy of the numerical model and the size of it, the effect of changing the (fluid) element size from 18μm (about 1/3rd of the fiber thickness) to 6μm (about 1/9th of the fiber thickness) on the pressure drops obtained in the simulations (with a four-layered woven matrix model, fiber thickness, a, as 56μm) was carried out over a range of inlet flow velocities from 1.08 m/s, to 12.26 m/s, i.e., from Reynolds number of 19.8 to 163.3. As indicated in Figure 22, the pressure drops predicted by the models with larger elements are about 6% lower than that predicted by the models with smaller elements. However, there is a ten-fold decrease in the size of the model created with the larger elements, thus enabling the development of numerical models that can capture physically large systems at lower computational cost without compromising accuracy in a significant manner. This trend is observed to be valid for flows over a wide range of Reynolds numbers. Thus, element size of about 1/3rd of the fiber thickness or diameter were used for all following models would be discussed later.

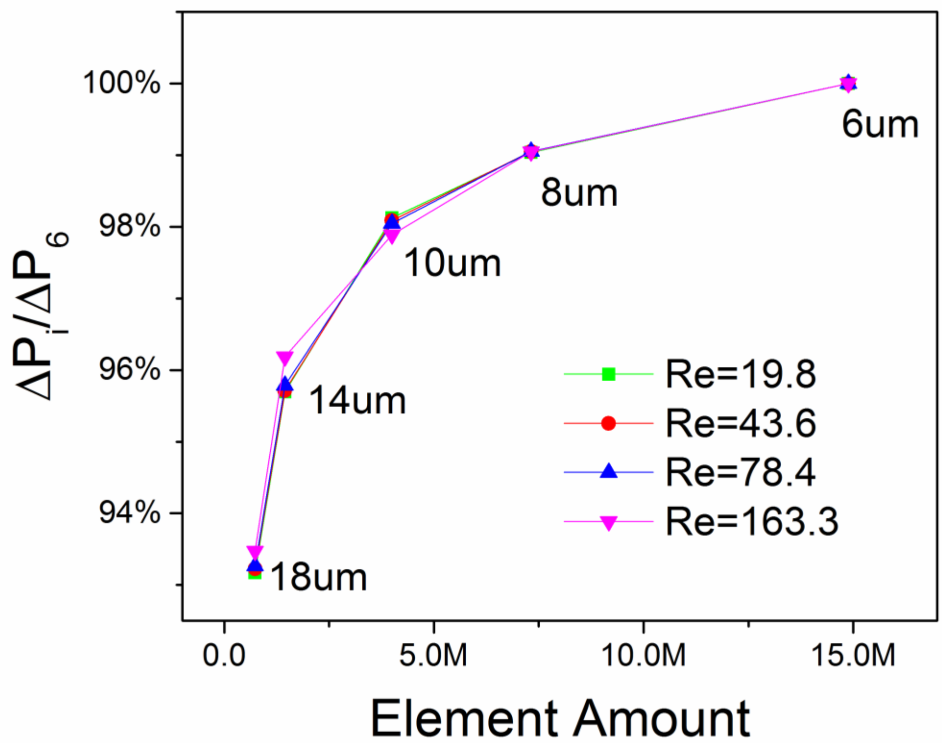

Figure 22. The pressure drops obtained in the numerical model simulations of a 4 layered, 4 x 4 open porous section of a woven matrix where the fluid element size is varied from 6 microns to 18 microns indicate that the pressure drops decrease as the element size decreases. The pressure drop obtained in a model with element size ‘i’ (ΔP_i) is normalized by the pressure drop observed in the model with the element size of 6 microns (ΔP_6).

Since the numerical model developed in the present work is based on the incompressibility assumption, the density, ρ, of the gaseous fluid that flows through the porous medium is considered as a constant. Hence, from equation 32, it can be deduced that the pressure drops expected from the flow of the fluid through the porous medium, should be proportional to the size of the porous media in the direction of fluid flow. Thus, the pressure drops obtained from the model simulations, ΔP_{mo}, for a given thickness of the stacked woven matrices or the random stacked fiber layers, t_{mo}, could be scaled linearly with mid-part thickness for comparison of the pressure drops measured in the experiments, ΔP_{re} using samples with a thickness of t_{re} as:

$$\Delta P_{re} = \Delta P_{mo} \frac{t_{re}}{t_{mo}} \qquad \text{Eq (47)}$$

The corresponding expressions for the friction factors C_f' and C_f are as follows:

$$C_f' = \frac{\Delta P_{mo} a}{\rho t_{mo} u_{in}^2} \frac{\beta^3}{1-\beta} \quad \text{Eq (48)}$$

and

$$C_f = \frac{2\Delta P_{mo}}{\rho} \frac{d_h}{t_{mo}} \frac{1}{u_m^2} \quad \text{Eq (49)}$$

2.5 Discussion

2.5.1 Comparison of simulation results between circular fiber and square fiber models

To assess whether the flow characteristics captured in models with square fibers are accurate, a series of numerical simulations were also carried out on models with circular fibers with identical weave patterns, matrix thickness, porosity and frontal velocity conditions as on models with square fibers. In these simulations, the diameter of circular fibers was also set to be equal to the thickness of square fibers, i.e., 56 μm.

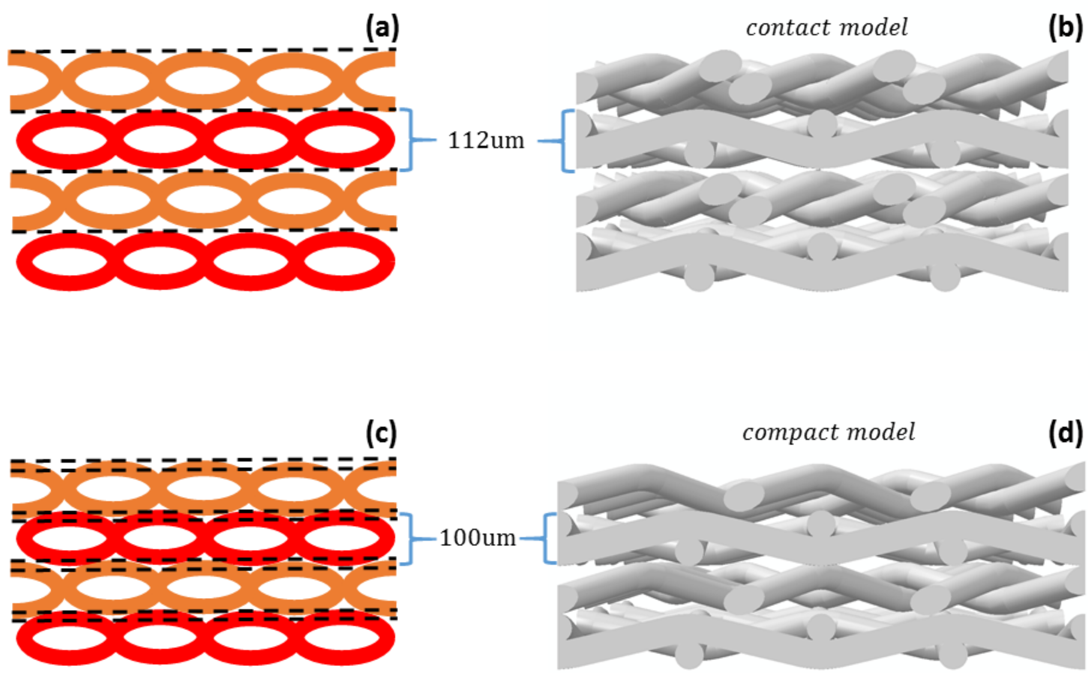

Figure 23. Schematics illustrating two kinds of 4-layer porous media with 4 x 4 open woven matrix comprised by circular fibers: (a) and (b) contact model; (c) and (d) compact model.

During the process of creating woven media models with the circular cross-section fibers, there were two strategies on how to deal with the junction between any two matrices, which is rarely deliberated by others. The first is just as shown in figure 23(a) and (b), where top matrix just contacts bottom layer at certain points, hereafter referred to contact model. According to the calculation[88], with fixed fiber diameter as 56 μm, the open size need to be modified to 168 μm to make sure the porosity of the midstream part still as 80%. It's worth noting that, under such restrictions, the matrix thickness is exactly equal to twice the diameter of fibers, i.e., 112 μm which is greater than experimentally measured value, i.e., about 100 μm. The second is to compress the mid-stream part at two ends so as to reduce the layer thickness to exact 100 μm, which means the bottom boundary of upper layer will enter the top boundary of lower layer and *vice versa*, which is displayed in figure 23(c) and (d), namely compact model. It would not be difficult to find that open size now is equal to 198 μm, consistent with practical measurement on a real sample.

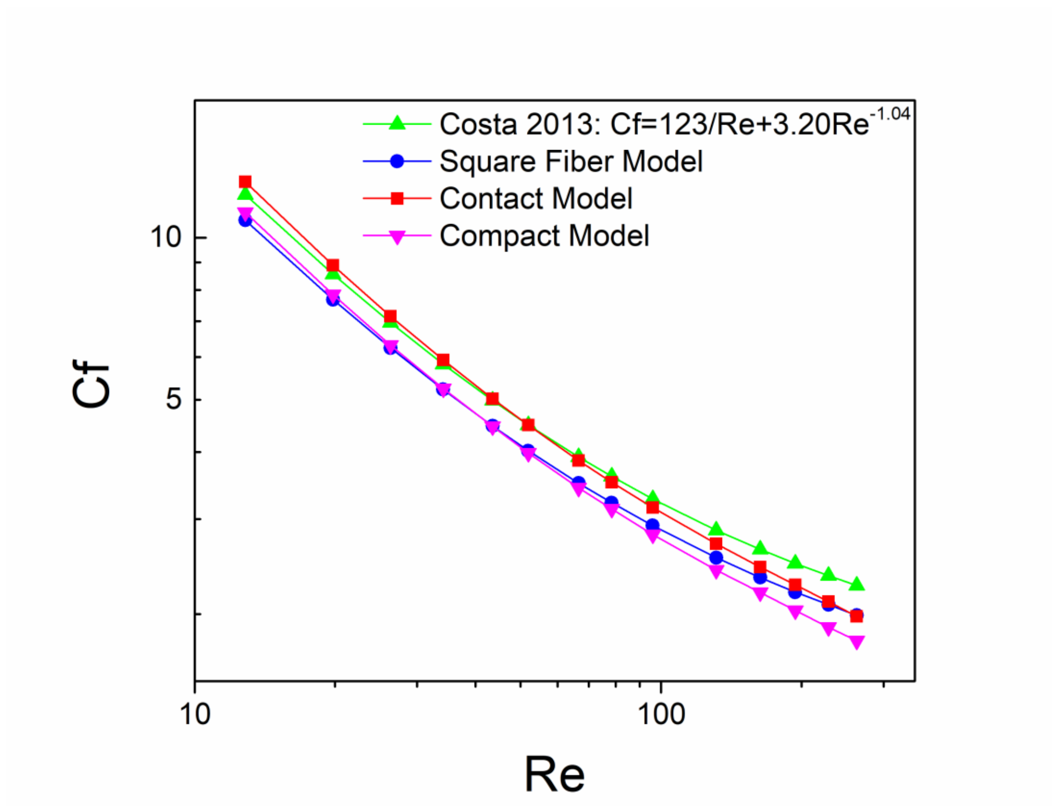

Figure 24. The characteristic relationship between the friction factor C_f and the Reynold's number Re as predicted by the 4-layer numerical model simulations of a 4 x 4 open porous section of a woven matrix with square fibers and circular fibers compared to results by Costa [59].

As indicated in Figure 24, it is evident that the relationship between the friction factor and the Reynolds number observed in models with square fibers is within 10% of that obtained with circular fibers. At lower Reynolds numbers, the results obtained from the simulations with square fibers are almost the same as those obtained from compact models, while at higher Reynolds numbers, results tend to approach those from contact models. As well, the modeling simulations (which feature a fiber lay-up that follows a regular 0^0, 45^0, 90^0 rotational sequence in the through-thickness direction) agree reasonably well with the predictions of Costa's correlations [59] (which are most accurate for structures with laterally displaced stacked layers).

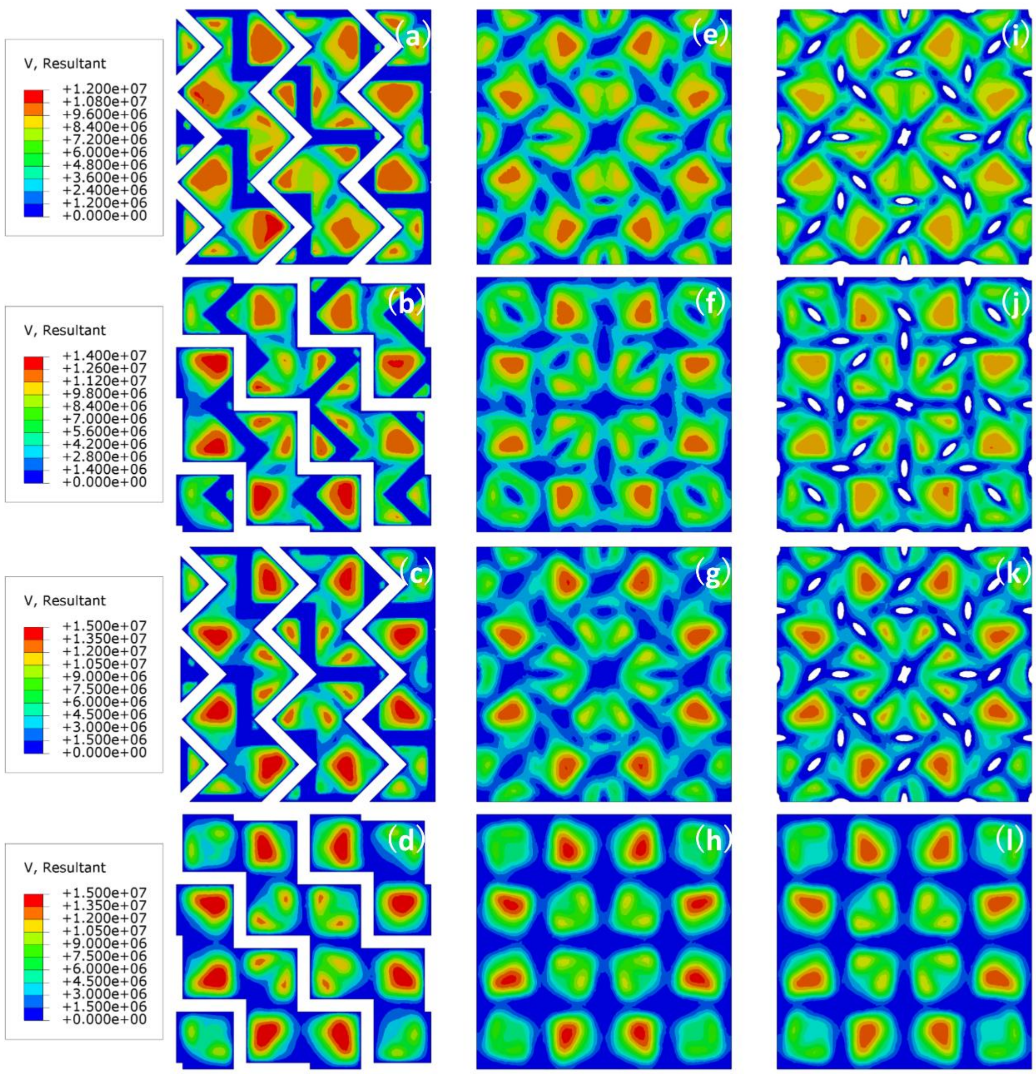

Figure 25. Plots exhibiting resultant velocity maps of all three models (woven matrix media model, contact model and compact model) at each layer.

Figure 25 exhibited resultant velocity maps of all three models (woven matrix media model, contact model and compact model) at the bottom of each layer, i.e. from the 1st layer to the 4th layer. Inlet flow velocity, u_{in}, is set to be 4.18m/s, Re as 78. The woven matrix media model with square fibers successfully reproduced most flow features throughout the whole fluid part as in models with circular fibers. In other words, matching between simulation results of two circular fiber models and the square fiber model is not a coincide. Overall, it can be concluded that numerical models with square fibers accurately capture the flow characteristics through porous media with circular fibers. Therefore, all numerical models following will rely on square crossing sectional fibers with confidence.

There is another observed phenomenon need to be pointed out before going to next section. The detailed velocities distribution maps of X, Y and Z directions, for the two circular fiber models, are demonstrated in figure 26 as well. Inlet flow velocity, u_{in}, at inlet boundary is set to be 2.35m/s, i.e. Re is equal to 44 this time. The displayed plane is the middle XY plane of middle stream part, i.e., the bottom plane of the 2nd layer or top plane of the 3rd layer. Clearly, the in-plane velocities distribution, i.e. velocities in X and Y directions, of contact model are more intensive comparing compact model. In the meantime, the out-of-plane velocity plots look pretty much the same for both models which explained why compact models tend to slightly underestimate the pressure loss when compared to contact models.

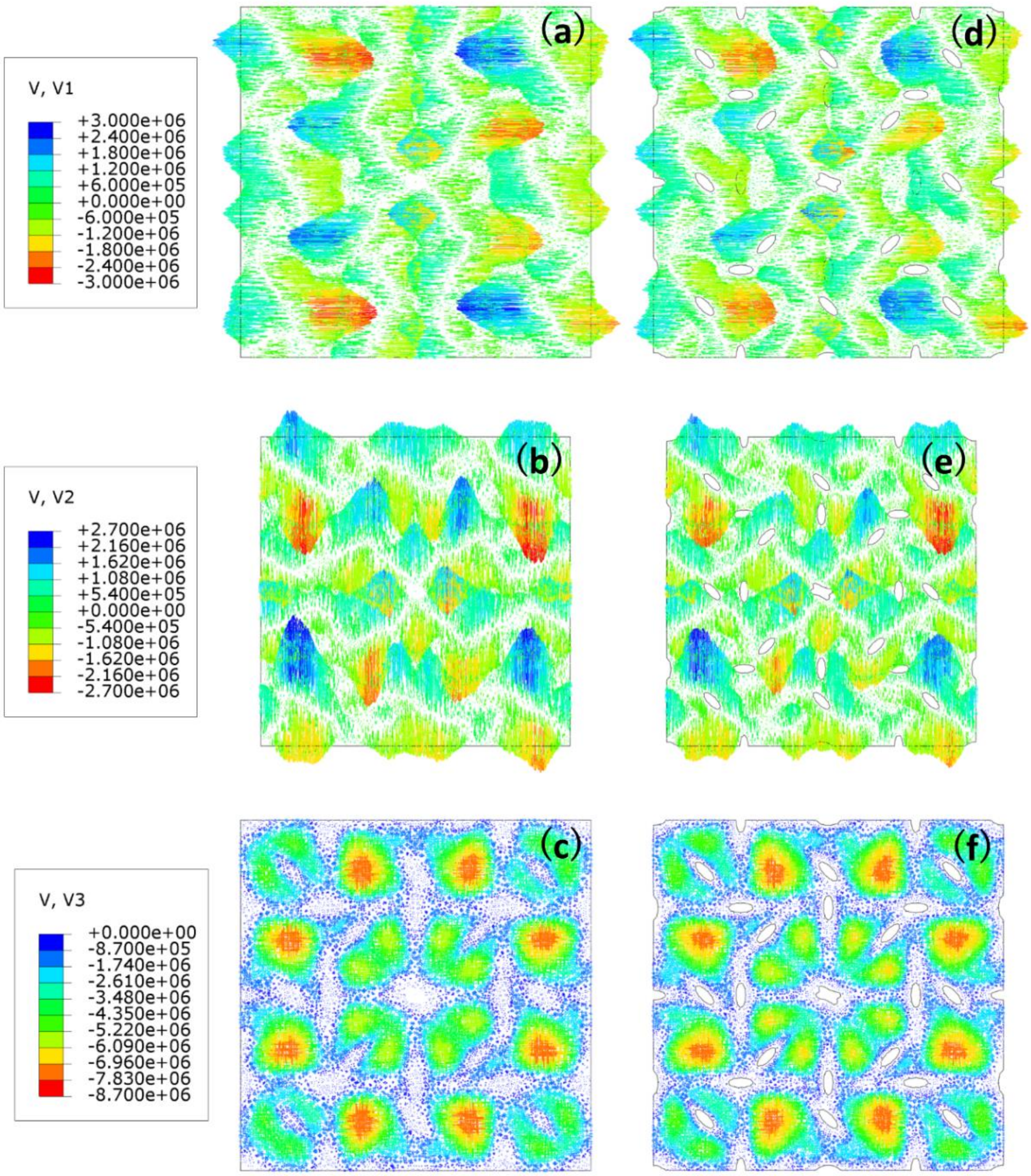

Figure 26. Plots exhibiting velocity distribution maps in all three directions of contact and compact models: (a)-(c) the contact model and (d)-(f) the compact model.

2.5.2 Large numerical models for assessing size effects

As demonstrated in Section 2.5.1, results obtained from the numerical models developed in the present study which had a representative volume that comprised of a 4 x 4 open porous section in the in-plane direction and four layers of the woven matrix in the through-thickness direction compare well with Costa's results. To assess the sensitivity of the pressure drops predicted by the numerical model developed in the present study to the model size, a systematic study was carried out by varying the model size in the in-plane direction and in the through-thickness direction based on the setting from section 2.5.1.

2.5.2.1 Sensitivity to the model size in the in-plane direction

As presented in Figure 27, the model size was increased in the in-plane direction from a 2 x 2 open porous section to a 10 x 10 open porous section, while the size in the out-of-plane direction kept unchanged, and a comparison of the pressure drops predicted by the corresponding numerical simulations was made.

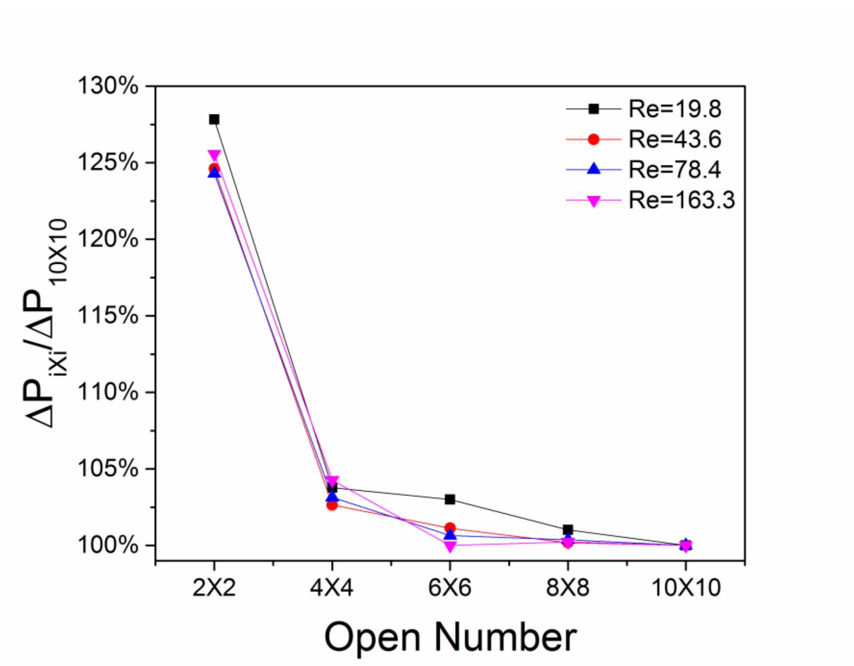

Figure 27. The pressure drops obtained in the numerical model simulations of a 4-layer woven structure where the model size is increased from a 2 x 2 to a 10 x 10 open porous section. The pressure loss obtained in a model with open porous section 'i x i' (ΔP_{iXi}) is normalized by the pressure loss observed in the model with an open porous section of 10 x 10 (ΔP_{10x10}).

In all cases the mid-stream part thickness was maintained constant at four layers. It is observed that changes in the model size, in the in-plane direction have only a very limited influence on the simulation results, especially, for models that have an open structure that is 4×4 or greater, which is also consistent with Green and Zhishuo's [73] observation. The difference in the results obtained in the model with a 4×4 open porous section and those obtained for a model with a 10×10 open porous section is less than 4%. Hence, it is evident that the model that features a 4×4 open porous section adequately captures the characteristics of flow through a woven matrix structure, while minimizing computational cost.

The significantly larger pressure loss observed in the 2 x 2 open porous structure is most likely due to boundary effects. Figure 28 illustrates the velocity distribution across the models for the 2×2, 4×4, 6×6 and 8×8 cases. It can be seen that the velocity distribution observed in the 2×2 open porous structure is different from that observed in other models. For example, the models with 4×4 and 8×8 open porous structures have lower speeds along diagonal directions, but higher speeds at the side borders which may contribute to the lower pressure drops observed in the larger models. Furthermore, it can be readily observed that the velocity patterns observed in the models with a 4 x 4 structure is also a part of the velocity patterns observed in the larger models with 6 x 6 and 8 x 8 open porous structures. Hence, it can be concluded that the models with a 4 x 4 open porous structure adequately capture the flow behavior of porous media with woven matrix structures.

The results observed in the present study are also consistent with the assessment of Mehta and Hawley [90] that when the ratio between the in-plane size of the woven matrix and the fiber diameter increase, boundary become less important and even negligible. In the models developed in the present study, the ratio between the woven matrix size and the fiber size is about 20 for the 4×4 open porous model and about 40 for the 8×8 open porous model. Thus, the boundary effects are expected to be reduced as the model size is increased.

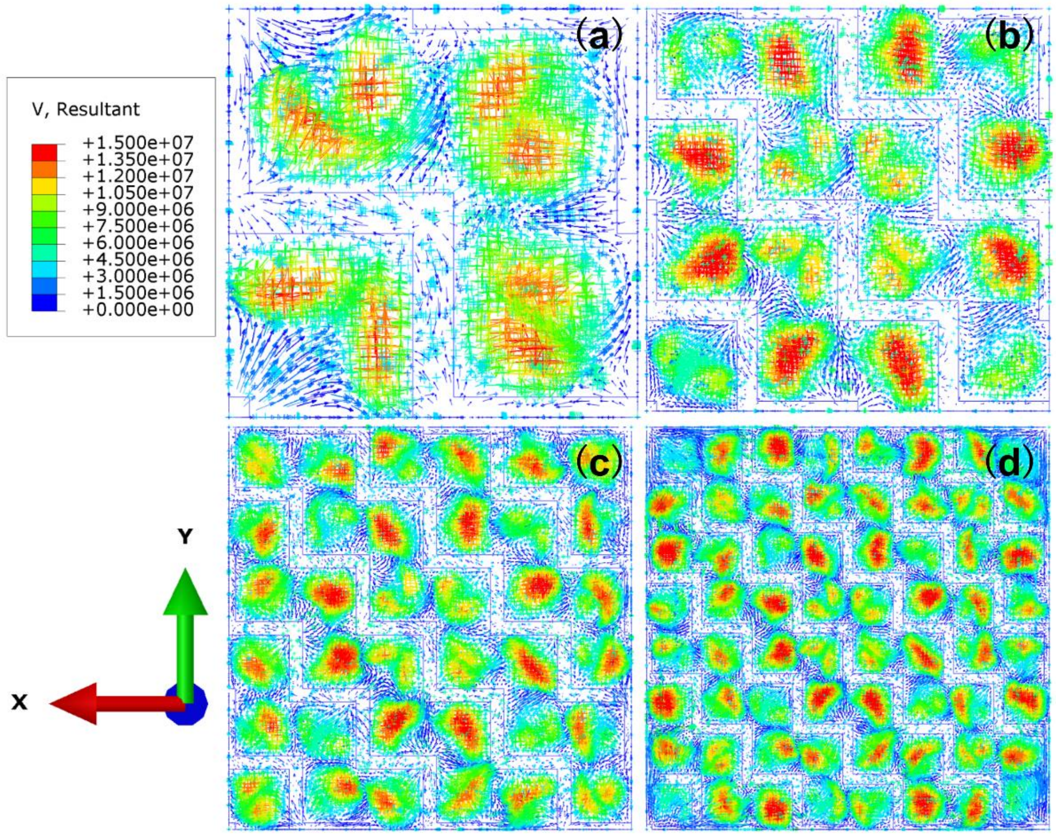

Figure 28. The resultant velocity distributions observed at the bottom of midstream part in the finite element models with (a) 2 x 2; (b) 4 x 4; (c) 6 x 6; and (d) 8 x 8, open porous sections.

2.5.2.2 Sensitivity to the model size in the through-thickness direction

The effect of the model size of out-of-plane direction on the pressure drop was also explored. The thickness of the porous media was progressively increased to assess effects of model thickness on the prediction of pressure losses while size at in-plane directions was fixed.

As shown in Figure 29(a), for a given Reynolds number, i.e., inlet flow velocity, the pressure drops per unit length observed in the thin models are consistently greater than those observed in simulations of thicker models. This trend is more distinct in Figure 29(b) where the pressure drop per unit length obtained in a model with 'i' layers, $(\Delta P/L)_i$, is normalized by the pressure drop observed in the model with 110 layers $(\Delta P/L)_{110}$ for several frontal velocities. When the model thickness is increased to 100 layers, the pressure drop value approaches that of the reference (110 layer) value.

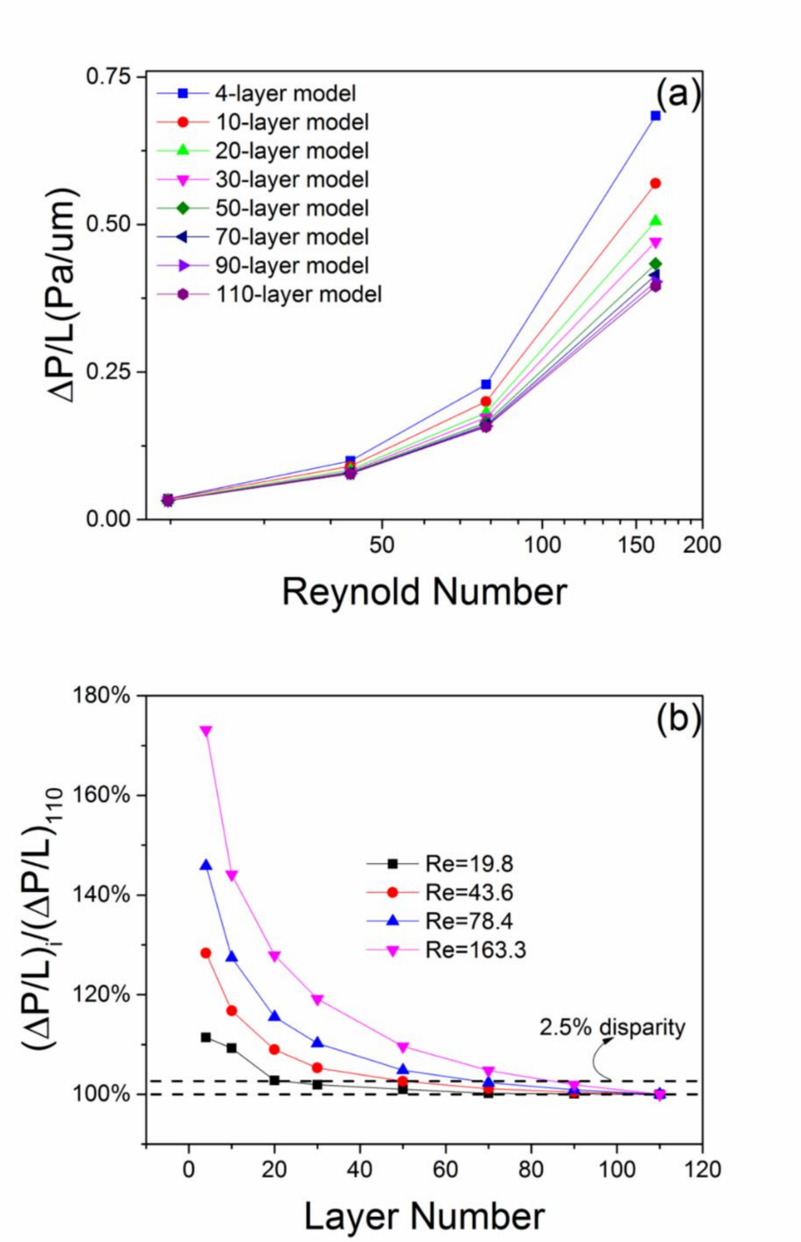

Figure 29. The pressure drops obtained in the finite element model simulations of a 4 x 4 open section of a woven structure, where the model size in the through-thickness direction is increased from 4 layers to 110 layers. The pressure drop per unit length obtained in a model with 'i' layers $(\Delta P/L)_i$ is normalized by the pressure drop observed in the model with 110 layers $(\Delta P/L)_{110}$.

Thus, it is evident that a numerical model with just a few layers of the woven matrix will not accurately capture the pressure drops observed in real systems where the number of layers is significantly more, especially, for flows with higher inlet velocities and higher Reynolds numbers.

This observation is attributed to the fact that boundary effects at the inlet and the outlet are captured at a disproportionately higher level in the case of thin models.

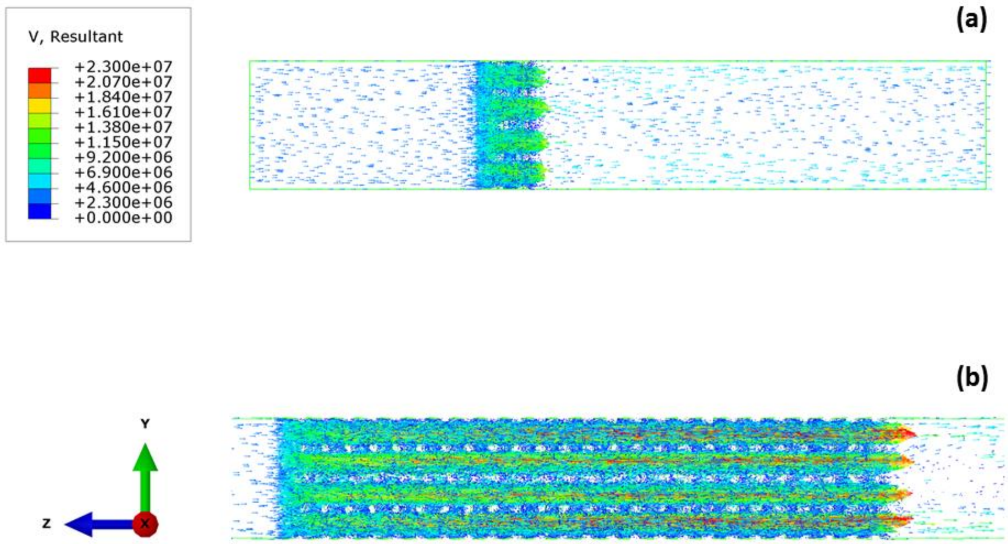

Figure 30. The through-thickness flow velocity distributions observed in the numerical models of a 4 x 4 open porous section of a woven matrix with (a) 4 layers and (b) 50 layers in the through-thickness direction indicating that the outlet flow fields are different in the two cases.

Figures 30 and 31 present the resultant velocity distributions of two models for which the Reynolds number are identical, i.e., 78.4. Figure 30 shows the axial velocity through the mid-plane of the matrix. The top distribution the top figure contains four layers of the woven matrix and the bottom figure contains 50 layers. In Figure 31, the cross-sectional velocity profiles are shown. Figure 31(a) shows the exit velocity at the fourth layer for a 4-layer matrix. Figures 31(b) - (f) show the cross-sectional velocity at layers 4, 10, 20, 30 and 50, respectively. While the velocity distribution in the fourth layer looks similar in both the models, the flow pattern continues to develop and reaches a steady state only around the 30th layer. Thus, the flow patterns observed at the respective outlets (fourth layer for the thin model and the 50th layer for the thick model) display significant differences. The velocity distribution in the 30th layer and 50th layer is similar indicating that the flow pattern starts to converge from about the 30th layer, which is consistent with the results for the pressure drops presented in Figure 29.

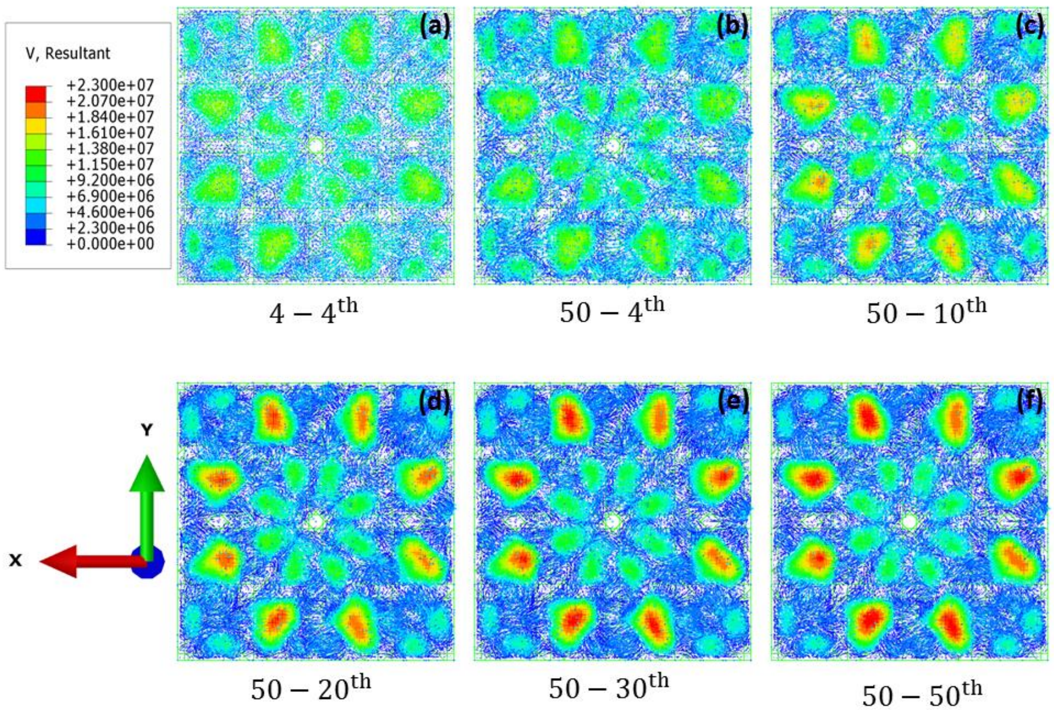

Figure 31. The flow velocity distributions observed in the numerical models of a 4 x 4 open porous section of a woven matrix in the thin models in 4th layer (a) and the thick models in the 4th (b), 10th (c), 20th (d), 30th (e) and 50th (f) layers.

By tracking the average pressure along the through-thickness direction of the fluid as it flows through the woven network porous media (Figure 32(a)) with large thickness in out-of-plane direction, it is evident that the fluid pressure drops at a medium flow rate as it flows through the first few layers (Figure 32(b)) and as the flow pattern reaches a steady state, the pressure drop reaches a steady state as well.

Thus, in order to obtain accurate estimates of the pressure drops in flow through woven matrices, it is important to conduct a sensitivity study and use models that are sufficiently thick such that the flow patterns are fully developed in the through-thickness direction

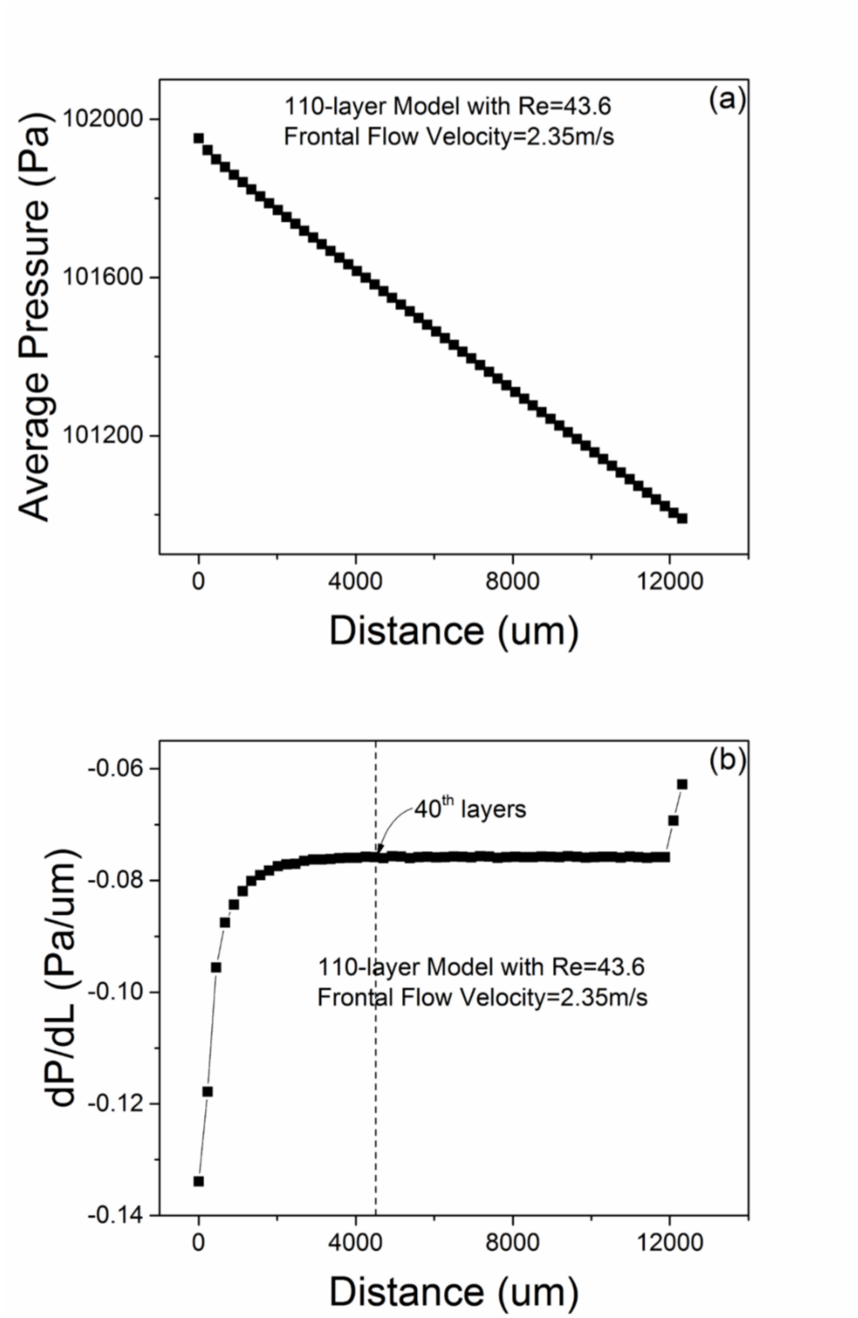

Figure 32. (a) The variation of fluid pressure as the fluid flows through a woven matrix porous medium observed in finite element modeling of a porous medium with 110 layers. (b) The rate of change in pressure as the fluid flows through the porous medium. (L is the through thickness distance in the porous medium.)

2.5.2.3 dP/dL in large size numerical models

In previous sections, it has been clearly demonstrated that the change of pressure drop rate at different thickness of models would help to understand the flow behavior as the fluid flows through the porous medium. Therefore, in this section, more outcomes will be displayed from this point of view.

According to Ergun's analysis (equation 32), the pressure loss when incompressible gas flowing through porous media should be proportional to the sample thickness. In other words, the value of dP/dL needs to be constant throughout the whole model which can be seen at high layer number of figure 33.

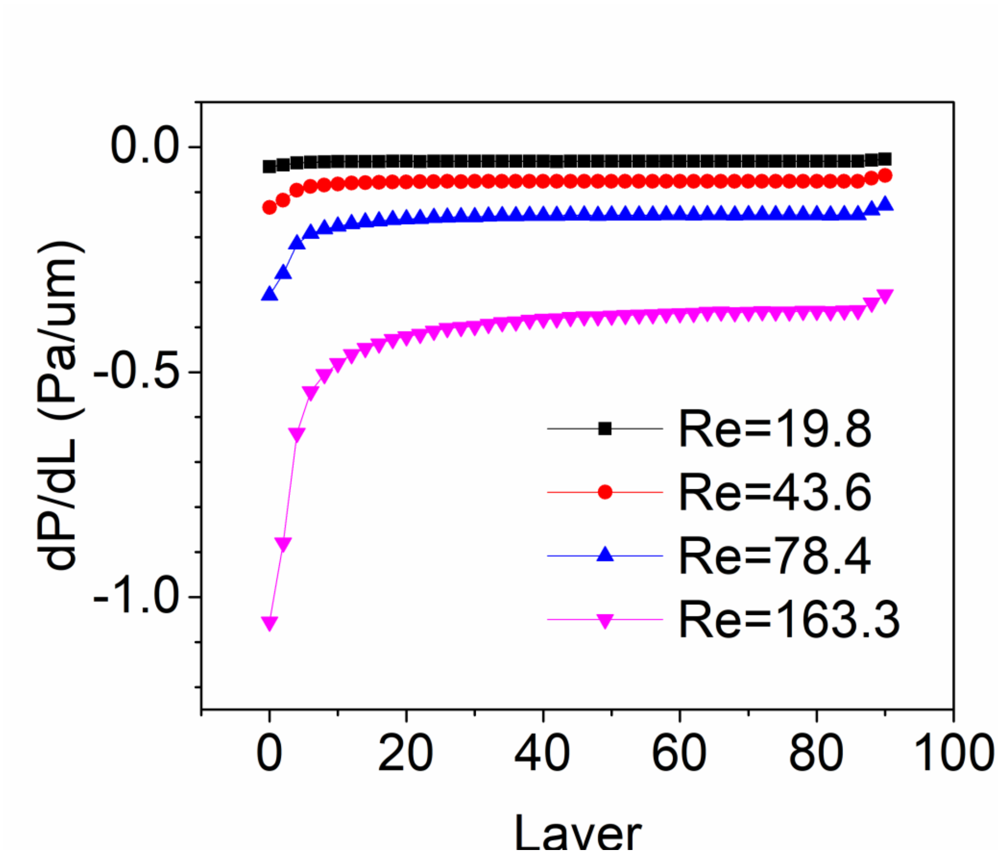

Figure 33. The rate of change in pressure as the fluid flows through the porous medium with different values of Reynold number.

Ergun equation is based on the mean flow velocity whose value is exactly a "constant" when fluid density fixed, i.e., fluid cannot be compressed. However, the implication of the “constant”, i.e., distribution of velocity could be varied via distance. Therefore, deviation happened at beginning layers for perfectly stacked woven screens. Higher the Reynold number, means higher inlet gas velocity, more layers are affected, by more intensive degree. However, even when Re as large 163.3, the model finally reached a status consist with Ergun’s prediction when the velocity distribution become stable and no more change with the increasing of screens layer.

The dramatic changing of dP/dL at top and bottom of calculating models might due to the entrance and exit effects. It looks like these two effects are constrained in the very first layers at two ends.

2.5.3 Comparison of simulation results with existing correlations and experiment data

The characteristic relationship observed between the friction factor C_f' and the Reynolds number Re' is shown in Figure 34(a). While Sodré and Parise [69] predict the correct trends (with an average error of about 25%), the 4-layer model simulations match the experimental results very well (with an average error of 6%) over the range of Reynolds numbers tested. All models with larger thicknesses in the flow direction underestimate the pressure loss to varying extents.

Simulation results are also compared to the two-parameter [84] and three-parameter [83] correlations for the friction factor as shown in Figure 34(b), indicating the relationship between friction factor in C_f and Reynolds number in Re. The results predicted by Tanaka's two-parameter correlation has almost the same error levels as those predicted by Sodré and Parise's while the average error of directly applying Gedeon and Wood's three parameters correlation is about 10%. Thus, the three-parameter correlation is observed to provide a better match than the two-parameter correlation for the range of Reynolds numbers explored.

One possible reason for the observed differences between the simulation results in the present study and those predicted by the friction factor correlations reported in the literature [69, 83, 84] could be due to the differences in the geometry of the woven matrix considered. The woven matrix media model considered in the present study, which captures the real system used in experiments, features a fiber lay-up that follows a 0^0, 45^0 90^0 rotational sequence in the through-thickness direction, which is not captured in the correlations reported in the literature.

The observed, larger than average deviation, in the friction factor, between the simulated results and experiments, at very low Reynolds numbers regime, might be due to the inaccurate measurement of pressure differences, in the experimental set-up, according to Green and Zhishuo [73], where the pressures were about only about 300 Pa, while there is a relatively better match at higher Reynolds numbers where the pressures were about 15,000 Pa.

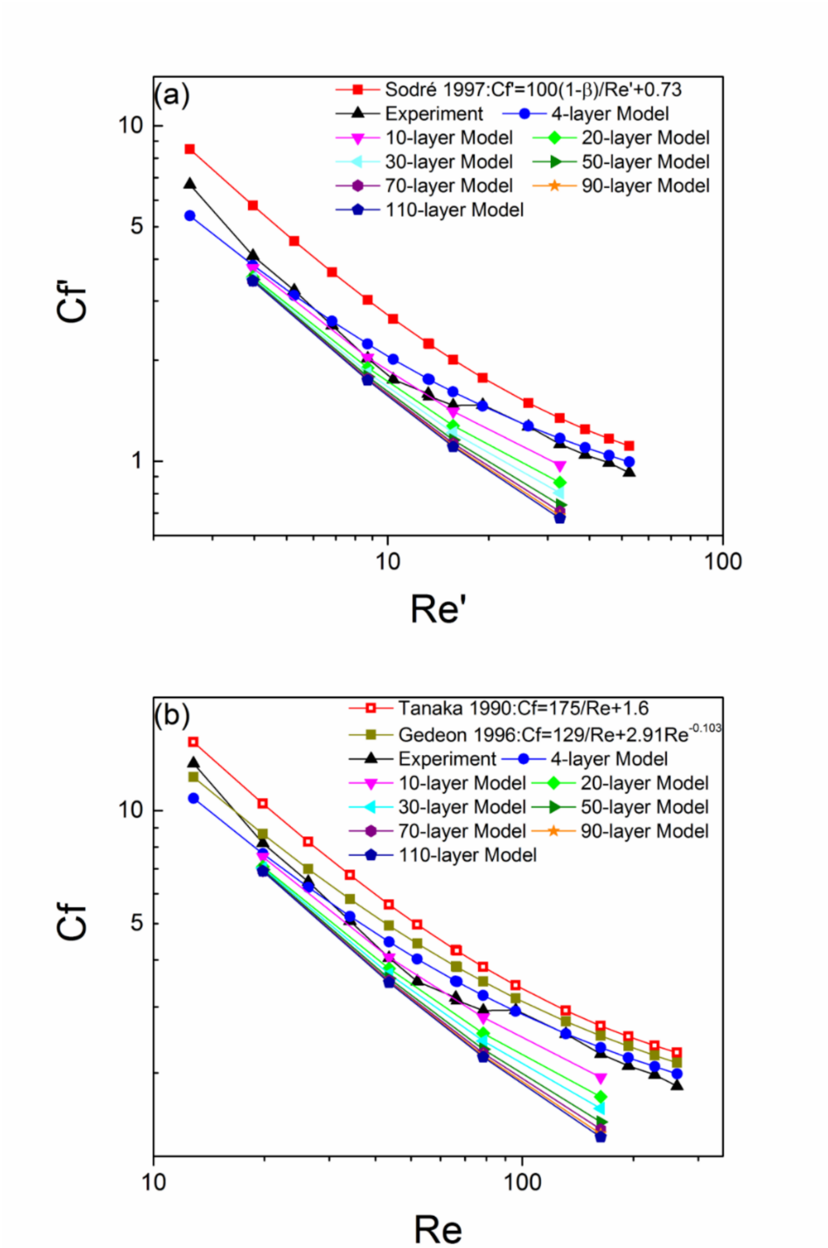

Figure 34. The characteristic relationship between the friction factor C_f' or C_f and the Reynold's number Re' or Re as predicted by Sodré and Parise [69] or a two-parameter model [84] and a three-parameter model [83] for the friction factor compared to finite element model simulations and experiments.

Overall, the simulations of the 4-layer woven media models developed in the present study provide a numerically better match to experimental results. However, as discussed in Section 5.2.2, models with larger through-thicknesses are conceptually expected to provide more accurate results in capturing the flow and pressure drop characteristics. This apparent paradox can be rationalized as follows.

The numerical models of thick systems where many layers were considered, inherently assumed that the layers are perfectly stacked on top of each other such that all the centers of each layer are all aligned with no lateral displacement in any layer. While theoretically it is possible to create such a perfect matrix, in reality it very likely that a geometrically defective misaligned layer whose center is laterally displaced relative to the other layers, may be created while the woven structure is fabricated (Figure 35). Hence, it is important to assess the influence of such defects on the overall flow behavior through the woven matrix models.

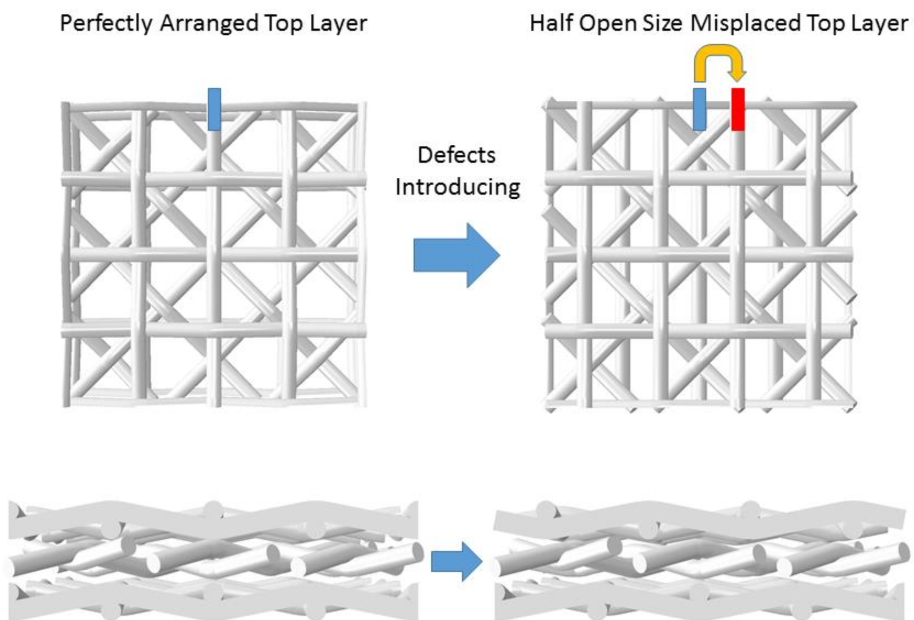

Figure 35. Schematics illustrating the introduction of a misaligned (defective) top layer by laterally displacing the top layer by a distance that is equal to half the open pore size.

2.5.4 Effect of defects on flow behavior in porous media with woven structures

A systematic study of the effects of defect density and defect intensity on the flow behavior though porous media with woven matrices was carried out. The detailed setting from section 2.5.3, i.e., $d = 56\ \mu\text{m}, w = 280\ \mu\text{m}, \beta = 80\%$ would be prolonged in this section.

2.5.4.1 Effect of defect density

As shown in Figure 36 in a numerical model with 40 layers, a misaligned defective layer is introduced every 4, 5, 8, 10 or 20 layers. Each defective layer is dislocated from its perfect position by half the open-pore size, i.e., 140 µm.

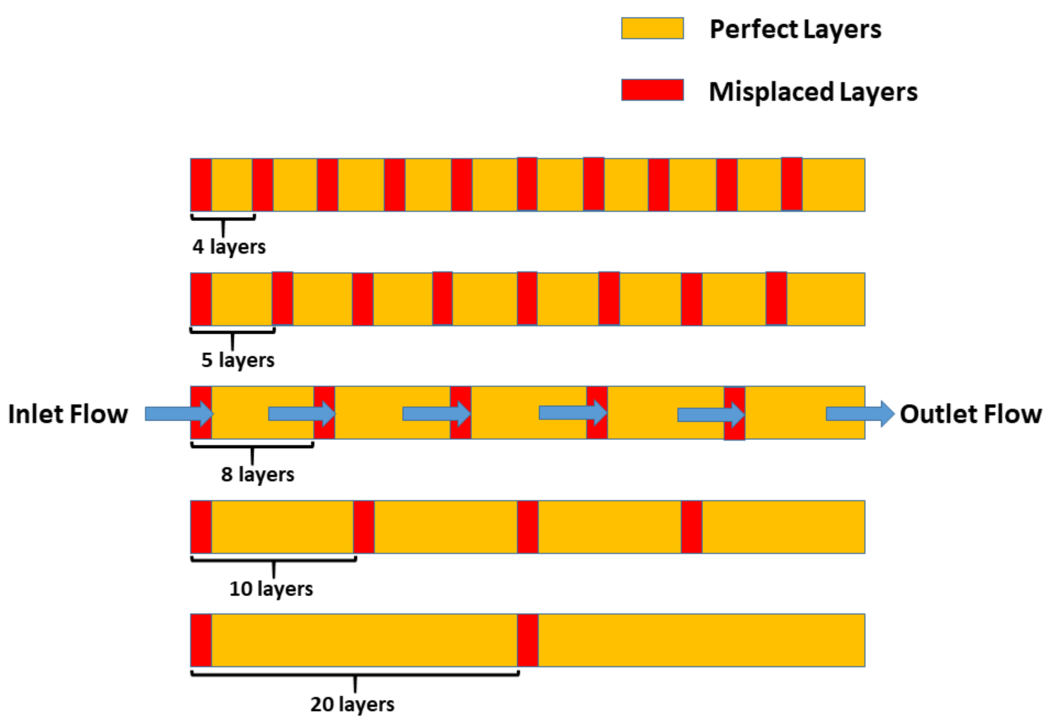

Figure 36. Schematics illustrating the introduction of a misaligned defective layer every 4, 5, 8, 10 or 20 layers in a model with 40 layers.

From the results presented in Figure 37, it can be found that as the density of the defective layers increases, the pressure drops predicted by the model increases, as each defective layer disrupts the steady flow pattern and impedes the easy flow of fluid. For flow conditions where the Reynolds number (Re) is small, the pressure loss difference between models with the most and least defect densities is less than 15%, while for flows with large Reynolds numbers (Re), the pressure loss difference increases to about 35%. Moreover, the results from the 40-layer thickness woven matrix model with defective layer every 8 layers match the experimental records best, especially at higher Reynolds number, which is rarely seen in small size models.

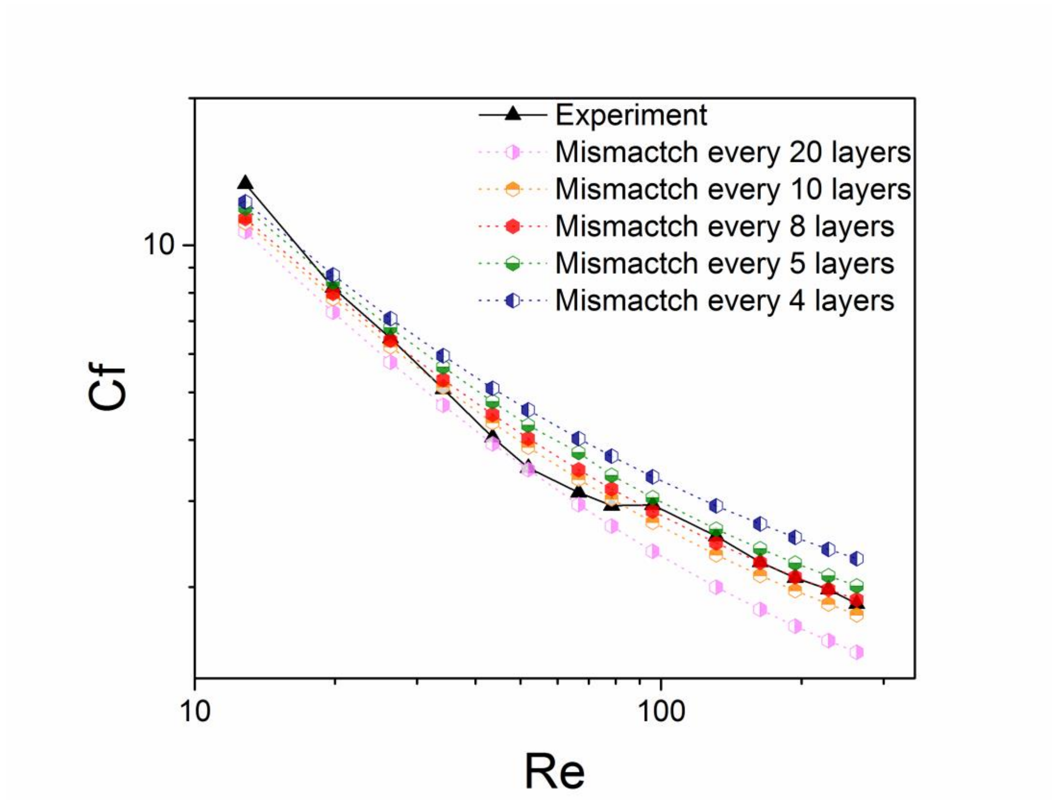

Figure 37. The characteristic relationship between the friction factor C_f and the Reynold's number Re as predicted by the 40-layer thickness numerical model simulations of a 4 x 4 open porous section of a woven matrix with misaligned defective layers and observed in experiments.

2.5.4.2 Effect of defect intensity

In order to ascertain the effect of the extent of misalignment in the defective layers on the flow behavior in porous media with a woven matrix structure, four representative defect configurations whose sizes scale with the length-scale of the open porous structure (1/8th, 2/8th, 3/8th and 4/8th of the open porous size, i.e., 35 µm, 70 µm, 105 µm, and 140 µm), were introduced into a numerical model that had a defect every eight layers (Figures 38 and 39). (In order to eliminate boundary effects, the locations of the defective regions were chosen such that a defective layer was not present at the end of the midstream section of the model (Figure 39).)

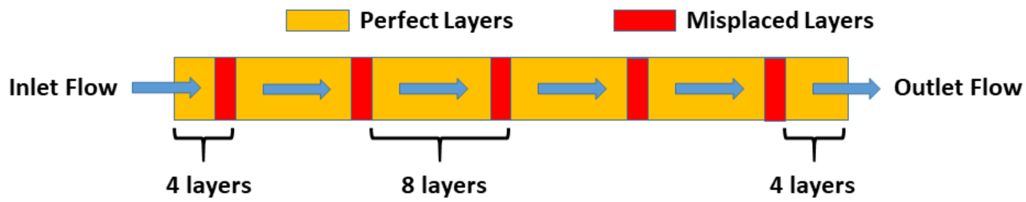

Figure 38. Schematic illustrating the introduction of defective layers every 8 layers in a model with 40 layers.

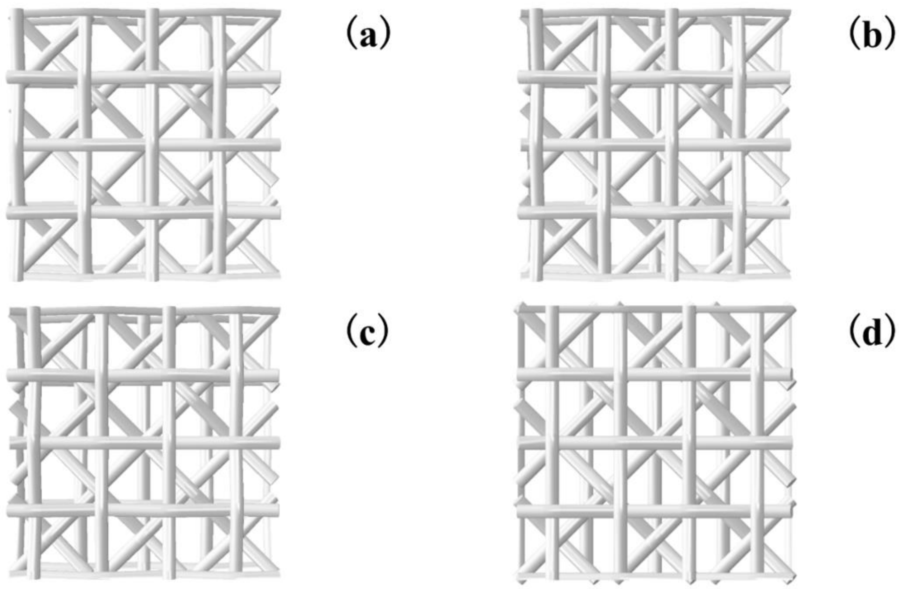

Figure 39. Schematics illustrating the introduction of defective layers with different extents of misalignments (i.e., lateral displacements of 35 µm (a), 70 µm (b), 105 µm (c), and 140 µm (d) relative to the perfectly aligned position of the layers), in a model with 40 layers.

As illustrated in Figure 40, the pressure drops, in general, increase with the extent of misalignment in the defective layers. The maximum deviation, of about 20%, is observed for flows where the Reynolds number (Re) is high (262), between models of which have the smallest (35 µm) and the largest (140 µm) misalignment. However, the difference in the pressure drops observed for models where the defective layers had misalignments of 140 µm and 105 µm is quite small, which two match the experimental consequences mostly.

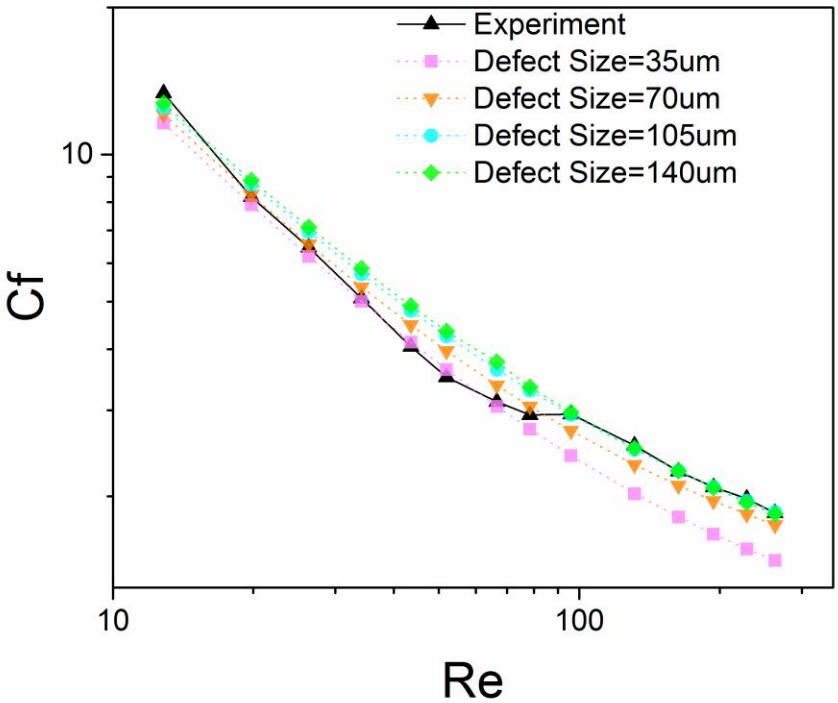

Figure 40. The characteristic relationship between the friction factor C_f and the Reynold's number Re as predicted by the numerical model simulations of a 40-layer thickness 4 x 4 open porous section of a woven matrix with defective layers which have different extents of misalignments every eight layers and observed in experiments.

Thus, it is evident that the extent of misalignment (i.e., defect intensity) and the frequency of defects (i.e., defect density) in the perfect arrangement of layers in the through thickness direction affect the flow behavior and in general, increase the pressure drops observed in flow through porous media with woven matrix structures. Therefore, in order to model the flow characteristics in woven porous media accurately, appropriate defects in their lay-up structures need to be considered as well. Ergun's analysis works well for most practical sample might thanks to the contribution of randomly dispersed defects which, therefore, resulting in a statistically stable velocity distribution throughout the whole model.

In summary, the finite element simulations on thin models with just four woven matrix layers predict larger pressure drops because they capture the inlet and outlet boundary effects in a disproportionate manner, while simulations of larger models with defective layer structures also predict large pressure drops because of the consideration of the defects in the lay-up. Hence, even though a good match observed between the simulations using thin models and experiments, it is physically more appropriate to make a comparison of the experimental results with the predictions of simulations with larger models which incorporate defective layers.

2.5.6 A method to increase application scope of a correlation: modification of d_h

From the previous discussion, it is clear models with same Reynold number, Re, but different fiber thickness, a, exhibit similar characteristics as fluid flow through woven matrix media, while models with same Reynold number, Re, but different porosity, β, show significant dissimilarity. The same phenomenon was also observed in Costa's [59, 64] work, where friction factor, C_f, for woven matrix media models with divergent porosity values are evidently different from each other and therefore, could be fitted by separated curves, which were also based on numerical methods. Gedeon [83] tried to explain such dependence on porosity, β, of friction factor, C_f, and capture all experimental data just using one single equation, which is an advanced version of equation 44 after including the term of β^{a_4}:

$$C_f = (a_1/Re + a_2Re^{a_3})\ \beta^{a_4} \qquad \text{Eq (50)}$$

Yet, equation 50 seems not work well for its original intentions. Here, in present work, 114 woven matrix models were created to further study how Re, β and a can affect the expression of C_f, i.e., in an independent way or in a comprehensive way. Although in section 2.5.3, a conclusion was proposed that small size models, especially thin models are not suitable for making a prediction of pressure loss as fluid flow through porous media, they can still be applied for unearthing some important rules, since boundary effect and size effect are hoped to be the same for all models at a certain value of Re. The out-of-plane dimension of the midstream part for these models was fixed at 4 times the thickness of screens, t, i.e., 8 time the fiber thickness, a. The in-plane size of the midstream part was delicately designed to make the ratio between the woven matrix size and the fiber size equivalent to or greater than 20. Under such ratio, it's believed boundary effects could be ignored for all models in this section, according to the discussions from section 2.5.2.1. To be more specific, the in-plane sectional size would be 6×6, 8×8, 12×12 open pores for models with porosity as 45%, 60% and 75%, respectively.

2.5.6.1 Setting of 114 models

These models were obtained by weaving square fibers (with five different thickness: $40\mu m$, $60\mu m$, $80\mu m$, $110\mu m$ and $140\mu m$) into the woven pattern as shown in figure 16. Three equal spaced porosity value, 45%, 60% and 75% were gained by controlling the open size of models. The frontal velocities of fluid were increased from 0.125m/s to as high as 40m/s, while corresponding values of Reynold's number varied from 2 to about 250. The detailed records of all 114 simulation models were compacted into figure 41.

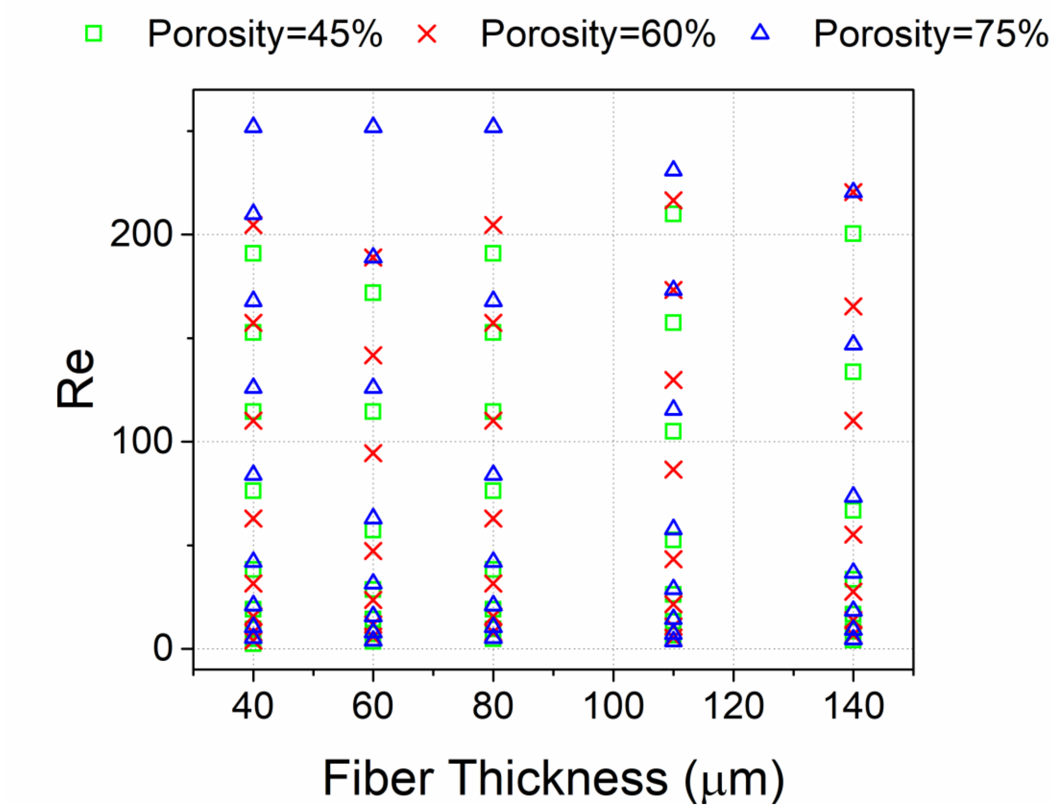

Figure 41. Plot includes all 114 models with different fiber thickness and Reynold number.

According to equation 43 and equation 44, friction factor, C_f, changes more dramatically at low Reynold number. Therefore, more models are concentrated at this region, just as displayed in figure 41, in order to capture the correct tendency for C_f.

2.5.6.2 Raw simulation results analysis

Simulation outcomes of total 114 models were first divided into smaller groups according to their fiber thickness and friction factor, C_f, calculated through equation 40, then were displayed in figure 42(a) - (e).

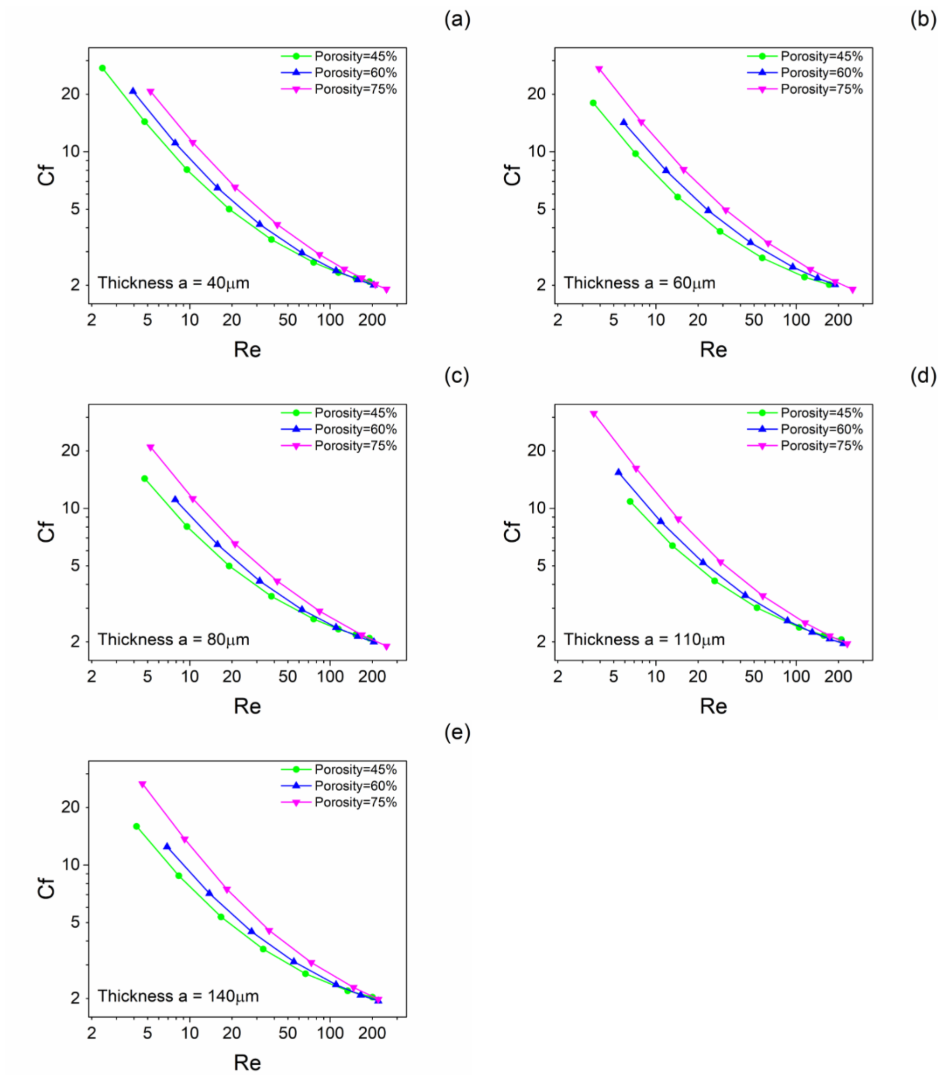

Figure 42. Plots illustrating the characteristic relationship between the friction factor C_f and the Reynold's number Re as predicted by 4-layer numerical models with dissimilar fiber thickness and divergent porosity.

In the first place, regardless the value of fiber thickness, a, curves standing for the relationship between C_f and Re of models with divergent porosities undoubtedly apart from each other. Second, when Reynold's number, Re, is less than 50, the friction factor, C_f, of a model with higher porosity is much greater than those of models with lower porosity, which is consistent with Costa's observation [64]. Moreover, curves standing for models with divergent porosity tend to converge at a higher Reynold number. And as Re continues to increase, curves for lower porosity models would even make a crossover of those for higher porosity models, which means the corresponding values of friction factor C_f of lower porosity models become greater than those of higher porosity models. At the right end of the curve for models with porosity equal to 45%, there is a clear tendency for it to become horizontal, which could be a signal as flow behavior transfer from laminar to turbulent. Nevertheless, such signal is not strong for other two curves. Third, curves represent a specific porosity value for models with dissimilar fiber thickness seem to occupy the same position in all figures. In other words, the relationship between friction factor, C_f, and Reynold number, Re, looks like only dependent on the variable of porosity, β.

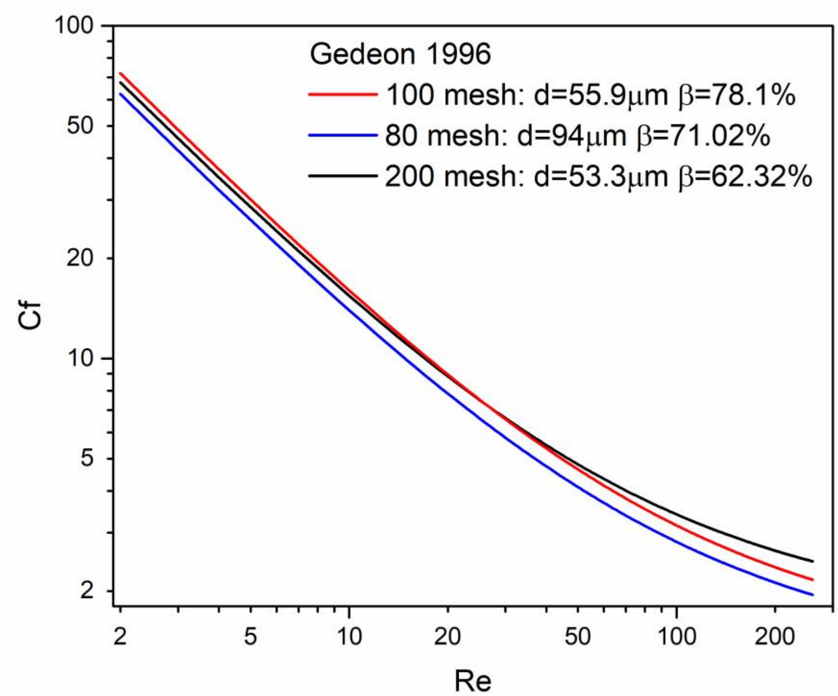

Figure 43. Plot illustrating the characteristic relationship between the friction factor C_f and the Reynold number Re based on Gedeon's research [83] on regenerators comprised of woven screens.

Above observations should not appear theoretically as stated by equation 35, 43 and 44, in which Re is the only declared mutable factor for C_f. However, same phenomena were also verified experimentally by Gedeon [83] as displayed in figure 43. In figure 43, the red line represents the relationship between the friction factor, C_f, and the Reynolds number, Re, for the generator of porosity equal to 78.1% and made up by circular wires with its diameter equal to 55.9 μm, i.e., 100 mesh per inch. The red line is obtained by fitting the three-parameter equation (equation 44) for friction factor, C_f, and a_1, a_2 and a_3 equal to 138.9, 2.567 and -0.0816, respectively. a_1, a_2 and a_3 have the value of 120.1, 2.369 and -0.0836, correspondingly, for the blue line and 129.3, 2.99 and -0.0758, respectively, for the black line. It is clear that the red line, standing for the highest porosity media, is at the top of the plot, and crossed by the black line, standing for the lowest porosity media when Re is raised to about 25. This value is somehow smaller than the observation in the present work. The other inconsistency between present work and Gedeon's results is that the black line, represents a low porosity regenerator of 62.32%, is above the blue line, represents a medium porosity regenerator of 71.02%, even at low Reynold number. Both discrepancies can be explained as the values of a_1, a_2 and a_3 from Gedeon's work were obtained by fitting the pressure loss, ΔP, with Reynold number, Re, which was able to be as big as 6,000 in experiments. Since the Re region of interesting in present work is only a very small part of it, and is at one end of it, some deviations are reasonable and acceptable. In general, 114 simulations successfully captured the basic rules between C_f and Re, β and a.

2.5.6.3 Modification of expressions for d_h and Re

As stated by above discussions, it looks like the best way of accurately describing the relationship between friction factor, C_f, and Reynold number, Re, is to create expressions case by case, i.e., to create an individual expression for a woven matrix model with a specific porosity value. Or, by sacrificing accuracy for simplicity, an overall expression could be obtained by fitting all data together, just as what has been tried by Gedeon [83]. However, it's well known, in the region of laminar flow, an alike flow system with the same value of Reynold number, Re, which is based on the characteristic length of the system, should give out consistent results. Therefore, a thought floated that might not all the key issues were about the equation form, but about the definitions in it.

In equation 39, S_v is only depended on the crossing sectional shape (S_v is $4/d$ for circular fiber and $4/a$ for square crossing sectional fiber), and have nothing to do with porosity β. This is basically correct when β is very high, e.g. 80% or 90%. However, the effect of overlapped area between any two fibers cannot be ignored anymore while β is low. Overlapped area does evidently exist in square fiber models, as displayed in figure 44, and real stacked woven screens samples which have been compressed at both ends.

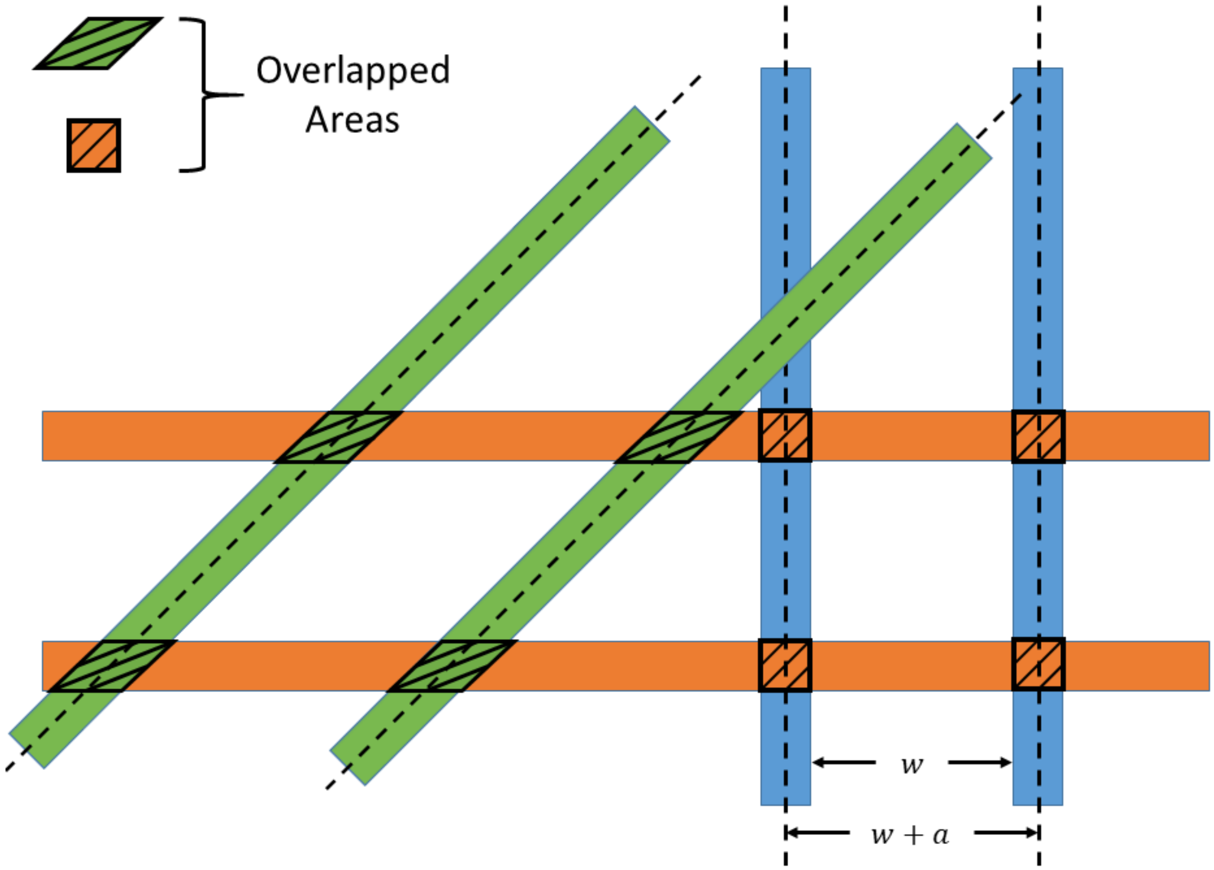

Figure 44. Schematic illustrating the overlap area between any two square crossing sectional fibers which would greatly impact the calcualtion of specific surface of solid, S_v.

Based on the definition of specific surface of solid, S_v, and associated with the schematic for overlap area between any two square fibers as above, i.e., between green and orange fibers or between orange and blue fibers, an equation for calculating the modified value of S_v^* for a square crossing sectional fiber is given as:

$$S_v^* = \frac{4}{a} - \frac{2}{(w+a)} = \frac{4}{a}\left(1 - \frac{a}{2w+2a}\right) \qquad \text{Eq (51)}$$

where, the superscript '*' is applied to distinguish between original specific surface (in equation 39) and the one after modification. Moreover, as open size, w, is function of fiber thickness, a, and model porosity, β, equation 51 is rewritten like below:

$$S_v^* = \frac{4}{a}(1 - \frac{1-\beta}{2}) = \frac{2(1+\beta)}{a} \qquad \text{Eq (52)}$$

In equation 52, when porosity β is very high, the value of $\frac{a}{2w+2a}$ could be ignored, equation 52 approach the value of $4/a$. For example, if β is 90%, then $\frac{a}{2w+2a}$ equals to 0.05. The Difference between equation 52 and the value of $4/a$ is only 5 percent. However, if the value of porosity β is very low, e.g. 45%, then $\frac{a}{2w+2a}$ is as large as 0.275. Deviation magnitude between equation 52 and the expression of $4/a$ could be as large as 27.5%. The overestimation of the specific surface of solid, S_v, would have a direct influence on the calculation of hydraulic diameter, d_h and therefore result in an underestimating of Reynold number, Re. To be exact, lower the model porosity value, larger the extent of undervaluing of Reynold number. As models with dissimilar porosity would have different discrepancy extent, curves in figure 42 apart from each other now can be well explained.

Hence, in order to obtain an accurate expression for relating friction factor, C_f to Reynold number, Re, and make precise prediction of pressure drop ΔP as fluid flow through porous media, it's necessary to redefine hydraulic diameter, d_h, first as:

$$d_h^* = \frac{4\beta}{S_v^*(1-\beta)} \qquad \text{Eq (53)}$$

then Reynold number, Re, as

$$Re^* = \frac{\rho}{\mu} u_m d_h^* \qquad \text{Eq (54)}$$

2.5.6.4 Simulation results analysis based on modified

The friction factor of all 114 simulation, together with the correlations from Gedeon's [83] work were recounted, by applying the modified value of hydraulic diameter, d_h^*, through equation as below, and the new relationship between C_f^* and Re^* were shown in figure 45 and figure 46:

$$C_f^* = \frac{2\Delta P d_h^*}{\rho L u_m^2} \tag{55}$$

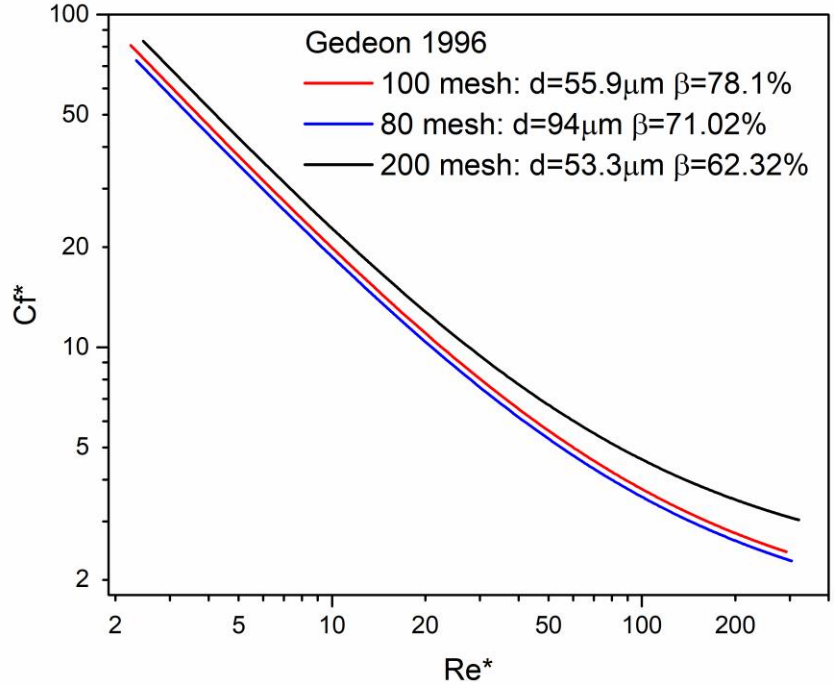

Figure 45. Plot illustrating the characteristic relationship between the modified friction factor C_f^* and the modified Reynold number Re^* based on Gedeon's research [83] on regenerators comprised of woven screens.

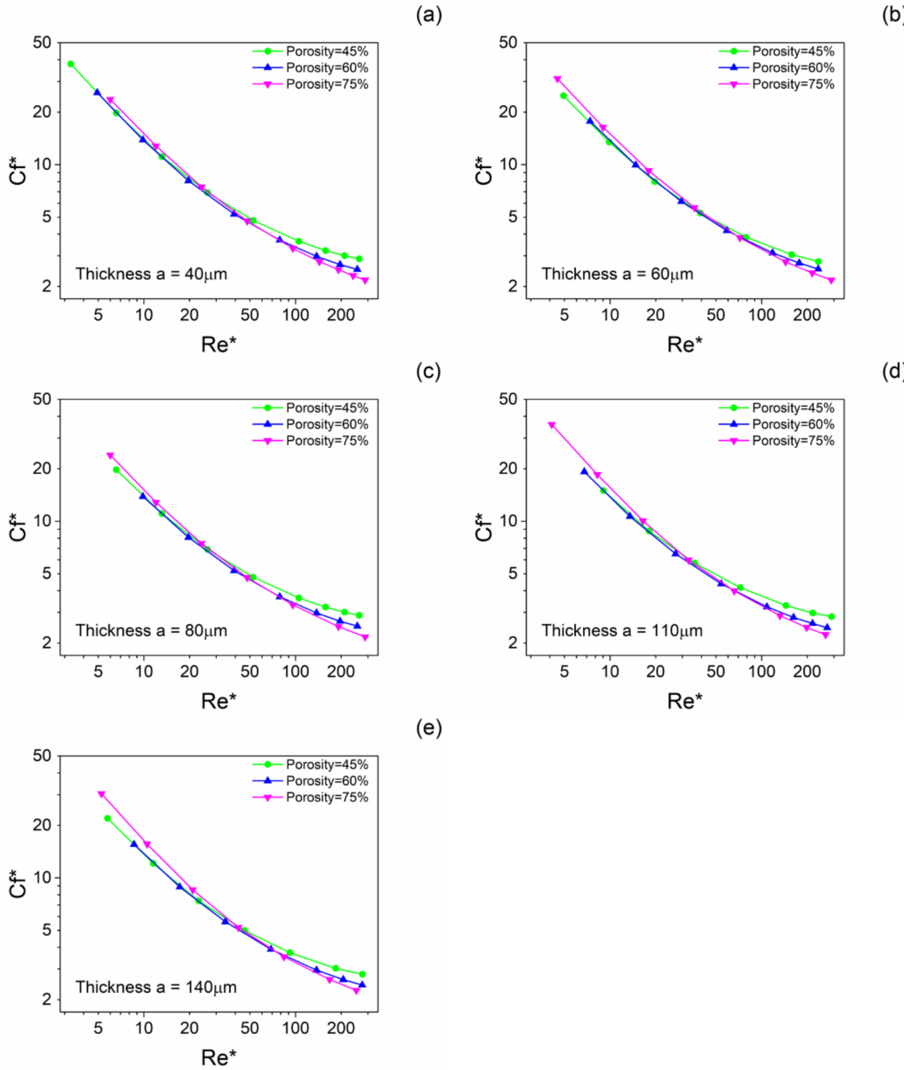

Figure 46. Plots illustrating the characteristic relationship between the modified friction factor C_f^* and the modified Reynold number Re^* as predicted by 4-layer numerical models with dissimilar fiber thickness and divergent porosity.

Although in Gedeon's work [83], crossing section of fibers is circular, equation 52 is still applied for the purpose of simplification as the similarity between square fiber and circular fiber, which has been mentioned before. Obviously, in figure 45, curves represent regenerators with 78.1% and 71.02% porosity become closer when compared to figure 43. But the situation that black line (62.32%) turn to be the top curve in the whole region of Re^* was not expected. Such phenomenon can be explained as in Gedeon's work, Re^* could be as large 7500, therefore the value of all parameters (a_1, a_2 and a_3) obtained through fitting C_f^* with Re^* might not fully captured the characteristic rules in this small and marginal section.

In figure 46, the tendency of converging for three curves, represent divergent porosity (45%, 60% and 75%), is not only apparent but also precise. When Re^* gradually increases, curves represent different porosity start to fork off the convergent results in sequence, from low porosity to high porosity. Such phenomenon indicated a possibility that the critical value of Re^*, at which flow behavior transferred from distinct laminar to distinct turbulent, might vary for different models, i.e., depend on the value of model porosity. Generally speaking, the low value of β means high density of sudden boundary change in a woven structure which could become a great improvement to the formation of turbulence, as fluid flow through porous media. On the contrary, models with high porosity would hinder the process of turbulence development. Another possible explanation for crossover between curves is due to the failure of the assumption of laminar flow under high inlet velocity in simulations. Even so, the variance among the values of Re^*, at which, crossover had been detected, still can provide the conclusion that porosity, β, of woven matrix model would determinate at what time flow behavior would transfer from distinct laminar to distinct turbulent. For example, the critical value of Re^* equals to 35 and 80 for models with the porosity of 45% and 60% respectively, as its value become about 200 for models with the porosity of 75% or higher.

The remaining deviation of curves for high porosity, i.e., 75%, at very small Re^* is probably due to the computational accuracy of finite element method. For example, as the thickness of square fibers is as large as 140um, the model pressure loss, ΔP_{mo}, of a 4-layer woven matrix model with porosity β equals to 75%, is only 1.1 Pa and 2.3 Pa when Re^* is 5 and 10, respectively. At the same time, the absolute pressure value for the whole model is over 1×10^5. Such problem might be solved by using a precise model with large size in the direction of flow. Otherwise, a treatment of excluding results with the pressure drop less than 10 Pa is suggested if those data would be used for creating a new correlation.

In present work, all 114 results were included into one plot as shown in figure 47. In figure 47 (a), 114 data points could have been grouped easily based on the porosity value. After the modification of hydraulic diameter, d_h, all data points now can distribute along a single curve.

First, it's very clear that fiber thickness, a has little influence on the relationship between weather C_f and Re or C_f^* and Re^*. Second, there is no necessity to create individual expressions for C_f^* case by case, if the modified Reynold number, Re^*, would be applied, at least when Re^* no more than 200. Above all, this rule meets people's expectation in this area, that Reynold number, Re^* plays a decisive role for laminar flow as long as a suitable definition is found.

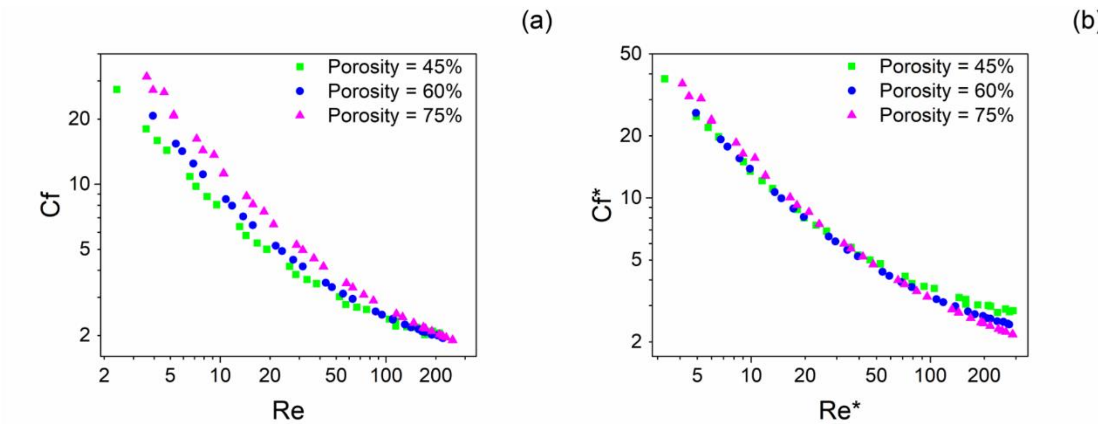

Figure 47 Plots displayed the simulation results from 114 models: (a) from the view of C_f and Re; (b) from the view of C_f^* and Re^*.

Miyabe [60] claimed that the area can be used for heat transfer between the fluid and solid, i.e., the contacted area, is considered as the total surface of fibers substrate the overlapped surface. Thus, the precise modification of specific area for circular crossing sectional fibers can be obtained through a careful derivation by following Miyabe's work. The expression of modified specific area, S_v^*, for a woven structure made up by circular fibers is as:

$$S_v^* = \frac{4}{d}\left(1 - \frac{1}{2\sqrt{(\frac{w}{d}+1)^2+1}}\right) \qquad \text{Eq (56)}$$

where $\frac{w}{d}$ is the function of porosity, β. A general equation of calculating specific area, S_v^*, is given before ending of this section:

$$S_v^* = \frac{4}{d_t}(1 - F(\beta)) \quad （0 < F < 0.5） \qquad \text{Eq (57)}$$

where F is an expression about porosity, β, can be determined by theoretical derivation or experiment test. Mehta [90] also tried to modify the calculation of hydraulic diameter earlier by including in the surface of walls and proved its effectiveness. In a large size model, compared to the effects of wall boundary, the impact from overlapped surface is at least an order of magnitude greater, which should not be ignored anymore.

In short, when Re^* is less than 200, if the woven configure is decided, there is a single expression which can depicture the relationship between friction factor and Reynold number, regardless of fiber thickness and mode porosity. When Re^* is greater than 200, a serial of equations is required to give an accurate prediction of pressure loss as fluid flow through a woven matrix model.

2.5.7 Study of feasibility as applying small-scale models on random stacked media

Gedeon [83] at the same time carried out a series of experiments to research the pressure loss as fluid flow through metal-felt matrices, which was made from circular crossing sectional fibers. In metal-felt matrices, fibers mainly lie transverse to the out-of-plane direction, also the flow direction. As in the plane, fibers were distributed with random angle and random spacing. From a practical perspective, the metal-felt matrices were of interest in the present study since the cost for processing metal-felt matrices was much cheaper than processing woven matrices. In order to simplify finite element models, all fibers were restricted in the plane perpendicular to the flow direction. So as to better understand how the degree of randomness would affect the pressure loss, 20 models were separated into two groups, i.e., model #1 to #10 belonged to group I, while model #11 to #20 belonged to group II. In group II, the angle of fiber and the spacing between two fibers were totally random, except that all fibers were required to parallel to each other for an individual layer, as shown in figure 19. As in group I, there was one more restriction to fibers angle, so as to make sure fibers could only extend in the direction $0°, 45°, 90°$ and $135°$, which were also the directions for fibers in woven matrices. Thus, hereafter, models of group II were referred to highly random models, as models of group I were referred to lowly random models.

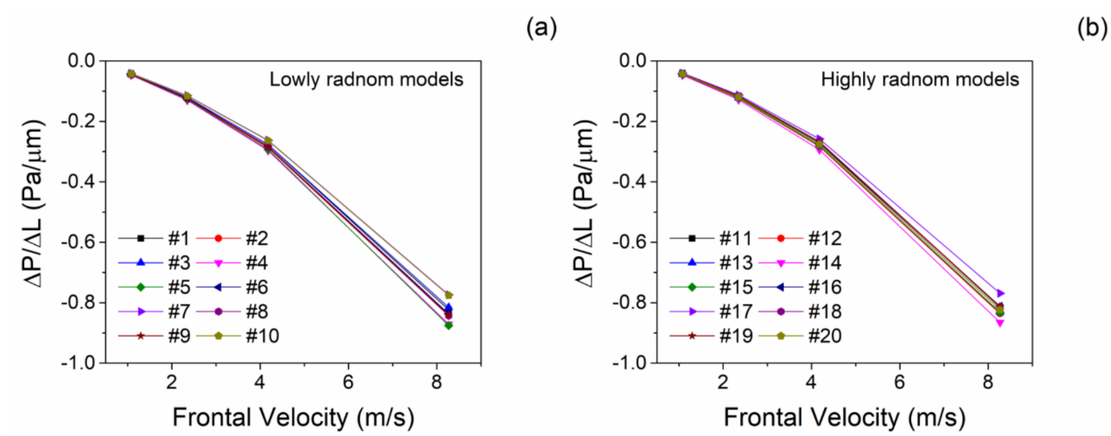

Figure 48. Plots displayed pressure loss per unit length, $\Delta P/\Delta L$, for two groups of random stacked models.

The simulation outcomes of pressure loss per unit length, $\Delta P/\Delta L$, for two groups of random stacked models are shown in figure 48. For both groups, the value of $\Delta P/\Delta L$ at different frontal velocities show dispersion to various extents. In figure 48(a), the $\Delta P/\Delta L$ obtained from model #10 is 11.5% smaller than that from model #5. In figure 48(b), the value of pressure loss per unit length for model #17 is 11.1% smaller than that from model #14. In order to have a direct impression of dispersion degrees of simulation results from 8-layer (fiber layer) random stacked models, the value of $\Delta P/\Delta L$, under different frontal velocities, are normalized to the average pressure loss per unit length of each group. The comparison among 20 models is demonstrated in figure 49.

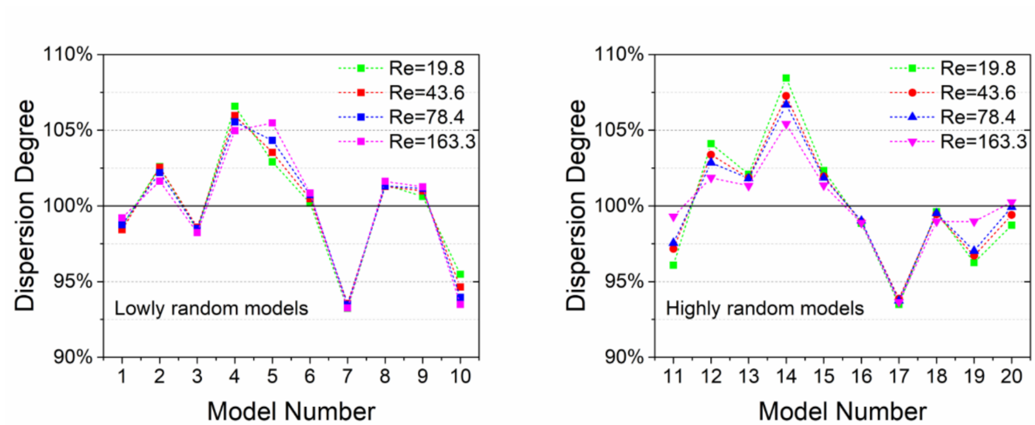

Figure 49. Plots illustrating the dispersiosn of simualtion results for two groups of random stacked models.

First, results dispersion degree for two groups looks close to each other. The largest dispersion degree in both groups is less than $\pm 10\%$. More than half results have the dispersion degree less than $\pm 2.5\%$. Nevertheless, it's still unsafe to simulate fluid flow metal-felt matrices with a thin 8-layer model. Up to 7.5% (this value might further increase since only 10 models of each group were studied) deviation might happen. Second, Reynold number, Re, has little influence on results dispersion of lowly random models, which could be seen in figure 49(a). However, after introducing the freedom of fiber angle, the phenomenon of results dispersion for models with low Re becomes greater markedly in figure 49(b). It might due to that fluid flow at low Re is more sensitive to the structure changes. For pressure drop at high Reynold number, Re, the main influence factor would be the density of sudden boundary or structure changes, which is a function of porosity, β, and have a minor connection with the angle change or spacing change.

The averaged pressure loss of either group was then substituted into equation 40 to calculate the average friction factor, C_f. The consequences were then compared to Gedeon's [83] work, experimental and simulation results of the present study as shown in figure 50.

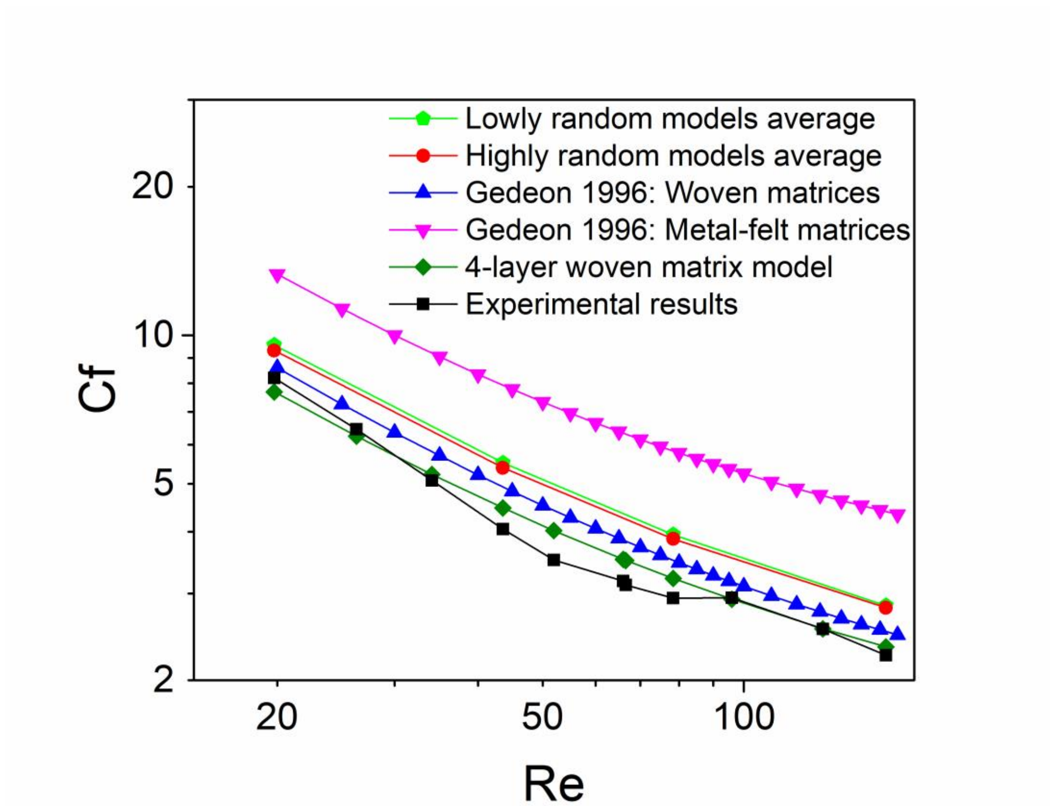

Figure 50. The average friction factor, C_f, obtained from two groups of random stacked models were compared with the consequence of Gedeon's work [83], and experimental and simulation results of present study.

In Gedeon's work, the value of friction factor, C_f, for metal-felt matrices is about 50% higher than it of woven matrices. The friction factor, C_f, obtained through simulating fluid flow through a random stacked model is 25% greater than the value got from woven matrix model, as two model have the same size of out-of-plane direction. The big deviation between simulations (8-layer random stacked model of the present study) and experiments (Gedeon experiment on metal-felt matrices) might due to the large range of Re (up to 2500) in experiments. More careful and concentrated (focus on Re region of interesting) experiments will be required. Another possible reason could be that oscillating flow was applied in Gedeon's work which might be more sensitive to a random structure.

In summary, larger size in the out-of-plane direction is preferred when simulating fluid flow through random stack models. Woven matrix structure can greatly reduce the pressure loss when compared to the random stacked structure.

2.6 Conclusion

Due to a multitude of application areas where flow characteristics through a porous medium need to be accurately predicted, there exists a strong motivation for a detailed analysis of flow behavior of fluids through a porous medium. Due to the complexity of the flow patterns in a porous medium that features a woven matrix configuration, a number prior studies have focused on developing numerical models. Due to the computational cost considerations, many of the numerical studies reported thus far have been able to model only relatively small regions of a physically large woven matrix. Little insight on the flow behavior in large model systems obtained through computational methods are at present available. Hence, present study focused on developing numerical models that capture the flow behavior of a fluid over large regions of a woven matrix open porous structure. The phenomenon of scatter of C_f values under same Re value was also studied in present work. In addition, a series of systematical simulations were carried out for small scale random stacked models. The main conclusions obtained from the present study are given below.

1. A finite element model that captures the geometric characteristics of a real woven matrix comprised of circular cross-section fibers and curvature due to fiber bending is developed with an equivalent model system comprised of fibers with square cross-section.

2. Changes in the in-plane size of the finite element model, lateral to the fluid flow direction, had relatively minor effects on the pressure drops predicted by the models. Significant boundary effects were observed only in the case of models that were very small, e.g., with 2 x 2 open porous section.

3. Changes in the thickness of the finite element model in the fluid flow direction had significant effects on the pressure drops. In simulations with very thin models, the boundary effects had a greater influence and caused the predicted pressure drops to increase proportionately. On the other hand, simulations with thick models indicated that the flows were fully developed and the boundary effects were minimized, resulting in relatively smaller pressure drops.

4. Defects in the lay-up of the woven matrix layers were also shown to have a significant

impact on the pressure drops predicted by the simulations. Higher defect densities resulted in greater pressure drops as they disrupted the steady flow of fluid in the through-thickness direction.

5. Higher defect intensities also resulted in greater pressure drops. Such tendency receded dramatically as defect size over 3/8th of the open porous size.

6. The pressure drops obtained in the finite element model simulations of thick models that contained some defective layers matched very well with experimental observations.

7. Scatter of C_f values at low Re (less than 200) can be well explained and amended by carefully recalculating specific surface of solid, S_v.

8. The value of pressure loss obtained from small scale random stacked models scattered intensively. Maxima and minima deviated from average value by $\pm$7.5%.

9. The averaged pressure loss obtained from small scale random stacked models was about 20% greater than it from small scale woven matrix model.

Future Works

Although many works have been done and many interesting conclusions have been obtained in the present study, it's still too early to say everything is going to be clear soon. More dedicated and challenging problems are waiting for explanations. In order to have a deeper understanding in both areas, there are some urgent topics for future works as:

(Computational Modeling of Indentation of Thin Films)

1. To condense the dimensionless equations with empirical formulae or theoretical derivations, so as to use them for practical purposes and on much more complex systems;

2. To extract more information from the substrate, e.g., plasticities and anisotropy, as penetration ratio is high;

3. To create dimensionless equations for "thick" film system, i.e., penetration ratio is restricted at a low level intentionally;

(Computational Modeling of Flow Through Porous Media)

4. To build a perfect woven medium with three-dimensional printing technic and verify the phenomenon of lower pressure drop in such media as fluid flowing through them;

5. To study the heat transmission in large size and perfect woven structures;

6. To extend the conclusions from the present study to the region of the compressible fluid and turbulent flow.

References

1. Oliver, W.C. and G.M. Pharr, *Nanoindentation in materials research: Past, present, and future.* Mrs Bulletin, 2010. **35**(11): p. 897-907.

2. Venkatesh, T.A., et al., *Determination of elasto-plastic properties by instrumented sharp indentation: Guidelines for property extraction.* Scripta Materialia, 2000. **42**(9): p. 833-839.

3. Lan, H. and T.A. Venkatesh, *On the uniqueness and sensitivity issues in determining the elastic and plastic properties of power-law hardening materials through sharp and spherical indentation.* Philosophical Magazine, 2007. **87**(30): p. 4671-4729.

4. Chen, X., et al., *On the uniqueness of measuring elastoplastic properties from indentation: The indistinguishable mystical materials.* Journal of the Mechanics and Physics of Solids, 2007. **55**(8): p. 1618-1660.

5. Chen, X. and J.J. Vlassak, *Numerical study on the measurement of thin film mechanical properties by means of nanoindentation.* Journal of Materials Research, 2001. **16**(10): p. 2974-2982.

6. Bhat, T.S. and T.A. Venkatesh, *Indentation of transversely isotropic power-law hardening materials: computational modelling of the forward and reverse problems.* Philosophical Magazine, 2013. **93**(36): p. 4488-4518.

7. Sneddon, I.N., *The relation between load and penetration in the axisymmetric Boussinesq problem for a punch of arbitrary profile.* International journal of engineering science, 1965. **3**(1): p. 47-57.

8. Oliver, W.C. and G.M. Pharr, *An Improved Technique for Determining Hardness and Elastic-Modulus Using Load and Displacement Sensing Indentation Experiments.* Journal of Materials Research, 1992. **7**(6): p. 1564-1583.

9. Zhao, M., et al., *A new approach to measure the elastic–plastic properties of bulk materials using spherical indentation.* Acta Materialia, 2006. **54**(1): p. 23-32.

10. Oliver, W.C. and G.M. Pharr, *Measurement of hardness and elastic modulus by instrumented indentation: Advances in understanding and refinements to methodology.* Journal of Materials Research, 2004. **19**(1): p. 3-20.

11. Bolshakov, A. and G.M. Pharr, *Influences of pileup on the measurement of mechanical properties by load and depth sensing indentation techniques.* Journal of Materials Research, 1998. **13**(4): p. 1049-1058.

12. Dao, M., et al., *Computational modeling of the forward and reverse problems in instrumented sharp indentation.* Acta Materialia, 2001. **49**(19): p. 3899-3918.

13. Cheng, Y.T. and C.M. Cheng, *Scaling approach to conical indentation in elastic-plastic solids with work hardening.* Journal of Applied Physics, 1998. **84**(3): p. 1284-1291.

14. Cheng, Y.T. and C.M. Cheng, *Relationships between hardness, elastic modulus, and the work of indentation.* Applied Physics Letters, 1998. **73**(5): p. 614-616.

15. Lan, H.Z. and T.A. Venkatesh, *On the sensitivity characteristics in the determination of the elastic and plastic properties of materials through multiple indentation.* Journal of Materials Research, 2007. **22**(4): p. 1043-1063.

16. Jeng, Y.R. and C.M. Tan, *Investigation into the nanoindentation size effect using static atomistic simulations.* Applied Physics Letters, 2006. **89**(25): p. 251901.

17. Manika, E. and J. Maniks, *Size effects in micro- and nanoscale indentation.* Acta Materialia, 2006. **54**(8): p. 2049-2056.

18. Zong, Z., et al., *Indentation size effects in the nano- and micro-hardness of fcc single crystal metals.* Materials Science and Engineering a-Structural Materials Properties Microstructure and Processing, 2006. **434**(1-2): p. 178-187.

19. Li, H., et al., *The Frictional Component of the Indentation Size Effect in Low Load Microhardness Testing.* Journal of Materials Research, 1993. **8**(5): p. 1028-1032.

20. Gao, H., et al., *Mechanism-based strain gradient plasticity - I. Theory.* Journal of the Mechanics and Physics of Solids, 1999. **47**(6): p. 1239-1263.

21. Jäger, I.L., *Surface free energy—a possible source of error in nanohardness?* Surface Science, 2004. **565**(2-3): p. 173-179.

22. Ma, Z.S., et al., *Indentation depth dependence of the mechanical strength of Ni films.* Journal of Applied Physics, 2008. **103**(4): p. 043512.

23. Chen, X., et al., *On the uniqueness of measuring elastoplastic properties from indentation: the indistinguishable mystical materials.* Journal of the Mechanics and Physics of Solids, 2007. **55**(8): p. 1618-1660.

24. Verdier §, M., et al., *Microstructure, indentation and work hardening of Cu/Ag multilayers.* Philosophical Magazine, 2006. **86**(32): p. 5009-5016.

25. Suresh, S. and A.E. Giannakopoulos, *A new method for estimating residual stresses by instrumented sharp indentation.* Acta Materialia, 1998. **46**(16): p. 5755-5767.

26. Deng, X., et al., *Deformation behavior of (Cu, Ag)–Sn intermetallics by nanoindentation.* Acta materialia, 2004. **52**(14): p. 4291-4303.

27. Deng, X., et al., *Mechanical Behavior of Multilayered Nanoscale Metal-Ceramic Composites.* Advanced Engineering Materials, 2005. **7**(12): p. 1099-1108.

28. Barshilia, H.C. and K. Rajam, *Characterization of Cu/Ni multilayer coatings by nanoindentation and atomic force microscopy.* Surface and Coatings Technology, 2002. **155**(2): p. 195-202.

29. Carvalho, N. and J.T.M. De Hosson, *Deformation mechanisms in TiN/(Ti, Al) N multilayers under depth-sensing indentation.* Acta materialia, 2006. **54**(7): p. 1857-1862.

30. Wen, S., et al., *Indentation creep behavior of nano-scale Ag/Co multilayers.* Scripta materialia, 2006. **55**(2): p. 187-190.

31. Zhao, B., B. Xu, and Z. Yue, *Indentation creep-fatigue test on aluminum alloy 2A12.* Materials Science and Engineering: A, 2010. **527**(16): p. 4519-4522.

32. Goldsby, D.L., et al., *Nanoindentation creep of quartz, with implications for rate- and state-variable friction laws relevant to earthquake mechanics.* Journal of Materials Research, 2004. **19**(1): p. 357-365.

33. Ebenstein, D.M., et al., *Nanomechanical properties of calcification, fibrous tissue, and hematoma from atherosclerotic plaques.* J Biomed Mater Res A, 2009. **91**(4): p. 1028-37.

34. Yao, H., et al., *Protection mechanisms of the iron-plated armor of a deep-sea hydrothermal vent gastropod.* Proc Natl Acad Sci U S A, 2010. **107**(3): p. 987-92.

35. Nakamura, T. and Y. Gu, *Identification of elastic–plastic anisotropic parameters using instrumented indentation and inverse analysis.* Mechanics of materials, 2007. **39**(4): p. 340-356.

36. Ma, T., et al., *Micrometer thick soft magnetic films with magnetic moments restricted strictly in plane by negative magnetocrystalline anisotropy.* Journal of Magnetism and Magnetic Materials, 2017.

37. Akkari, F.C., et al., *Ellipsometric characterization and optical anisotropy of nanostructured CuIn 3 S 5 and CuIn 5 S 8 thin films.* Materials Science in Semiconductor Processing, 2017. **71**: p. 156-160.

38. Hill, R., *A Theory of the Yielding and Plastic Flow of Anisotropic Metals.* Proceedings of the Royal Society of London Series a-Mathematical and Physical Sciences, 1948. **193**(1033): p. 281-297.

39. Cheng, Y.T. and C.M. Cheng, *Scaling, dimensional analysis, and indentation measurements.* Materials Science & Engineering R-Reports, 2004. **44**(4-5): p. 91-149.

40. Buckingham, E., *On physically similar systems, illustrations of the use of dimensional equations.* Physical Review, 1914. **4**(4): p. 345-376.

41. Chollacoop, N., M. Dao, and S. Suresh, *Depth-sensing instrumented indentation with dual sharp indenters.* Acta Materialia, 2003. **51**(13): p. 3713-3729.

42. Liao, Y., et al., *Measuring elastic–plastic properties of thin films on elastic–plastic substrates by sharp indentation.* Mechanics of Materials, 2009. **41**(3): p. 308-318.

43. Ruan, H.H., A.Y. Chen, and J. Lu, *Characterization of plastically graded nanostructured material: Part I. The theories and the inverse algorithm of nanoindentation.* Mechanics of Materials, 2010. **42**(5): p. 559-569.

44. Tunvisut, K., N.P. O'Dowd, and E.P. Busso, *Use of scaling functions to determine mechanical properties of thin coatings from microindentation tests.* International Journal of Solids and Structures, 2001. **38**(2): p. 335-351.

45. Lichinchi, M., et al., *Simulation of Berkovich nanoindentation experiments on thin films using finite element method.* Thin Solid Films, 1998. **312**(1-2): p. 240-248.

46. Bucaille, J.L., et al., *Determination of plastic properties of metals by instrumented indentation using different sharp indenters.* Acta Materialia, 2003. **51**(6): p. 1663-1678.

47. Antunes, J.M., L.F. Menezes, and J.V. Fernandes, *Influence of Vickers tip imperfection on depth sensing indentation tests.* International Journal of Solids and Structures, 2007. **44**(9): p. 2732-2747.

48. Petersen, K.E., *Silicon as a Mechanical Material.* Proceedings of the Ieee, 1982. **70**(5): p. 420-457.

49. Wortman, J. and R. Evans, *Young's modulus, shear modulus, and Poisson's ratio in silicon and germanium.* Journal of applied physics, 1965. **36**(1): p. 153-156.

50. Zhao, M., et al., *Measuring elastoplastic properties of thin films on an elastic substrate using sharp indentation.* Acta Materialia, 2007. **55**(18): p. 6260-6274.

51. Kretzschmar, R., et al., *Experimental determination of colloid deposition rates and collision efficiencies in natural porous media.* Water Resources Research, 1997. **33**(5): p. 1129-1137.

52. Grathwohl, P., *Diffusion in natural porous media: contaminant transport, sorption/desorption and dissolution kinetics*. Vol. 1. 2012: Springer Science & Business Media.

53. Nield, D.A., A. Bejan, and Nield-Bejan... *Convection in porous media*. Vol. 3. 2006: Springer.

54. Kays, W.M. and A.L. London, *Compact heat exchangers.* 1984.

55. Herzig, J.P., D.M. Leclerc, and P. Legoff, *Flow of Suspensions through Porous Media - Application to Deep Filtration.* Industrial and Engineering Chemistry, 1970. **62**(5): p. 8-&.

56. Lecoanet, H.F., J.Y. Bottero, and M.R. Wiesner, *Laboratory assessment of the mobility of nanomaterials in porous media.* Environ Sci Technol, 2004. **38**(19): p. 5164-9.

57. Minakuchi, H., et al., *Octadecylsilylated porous silica rods as separation media for reversed-phase liquid chromatography.* Analytical Chemistry, 1996. **68**(19): p. 3498-3501.

58. Ergun, S. and A.A. Orning, *Fluid flow through randomly packed columns and fluidized beds.* Industrial & Engineering Chemistry, 1949. **41**(6): p. 1179-1184.

59. Costa, S.C., et al., *Numerical study of the pressure drop phenomena in wound woven wire matrix of a Stirling regenerator.* Energy Conversion and Management, 2013. **67**: p. 57-65.

60. Miyabe, H., K. Hamaguchi, and K. Takahashi. *An approach to the design of Stirling engine regenerator matrix using packs of wire gauzes*. in *Proc., Intersoc. Energy Convers. Eng. Conf.;(United States)*. 1982. Department of Mechanical Engineering, Meiji University, 1-1-1 Higashimita Tama-ku, Kawasaki-shi.

61. Khaled, A.R.A. and K. Vafai, *The role of porous media in modeling flow and heat transfer in biological tissues.* International Journal of Heat and Mass Transfer, 2003. **46**(26): p. 4989-5003.

62. Vafai, K., *Porous media: applications in biological systems and biotechnology*. 2010: CRC Press.

63. Seki, K. and T. Miyazaki, *A mathematical model for biological clogging of uniform porous media.* Water Resources Research, 2001. **37**(12): p. 2995-2999.

64. Costa, S.-C., et al., *Experimental and numerical flow investigation of Stirling engine regenerator.* Energy, 2014. **72**: p. 800-812.

65. Armour, J.C. and J.N. Cannon, *Fluid Flow through Woven Screens.* Aiche Journal, 1968. **14**(3): p. 415-&.

66. Macdonald, I., et al., *Flow through porous media-the Ergun equation revisited.* Industrial & Engineering Chemistry Fundamentals, 1979. **18**(3): p. 199-208.

67. Jones, J.D., *Flow Losses in Stirling Engine Heat-Exchangers.* Journal of Engineering for Gas Turbines and Power-Transactions of the Asme, 1988. **110**(1): p. 58-62.

68. Simon, T.W. and J.R. Seume, *A survey of oscillating flow in Stirling engine heat exchangers.* 1988.

69. Sodré, J. and J. Parise, *Friction factor determination for flow through finite wire-mesh woven-screen matrices.* Journal of fluids engineering, 1997. **119**(4): p. 847-851.

70. Samanta, A.K., et al., *Study on the Effect of Different Woven Structures on Physical Properties of Cotton Muslin Fabric.* Journal of Natural Fibers, 2015. **12**(5): p. 444-456.

71. Xiao, X., et al., *Through-thickness permeability of woven fabric under increasing air pressure: Theoretical framework and simulation.* Textile Research Journal, 2016: p. 0040517516657062.

72. Ponzio, F.N., et al., *Experimental and computational investigation of heat transfer in channels filled by woven spacers.* International Journal of Heat and Mass Transfer, 2017. **104**: p. 163-177.

73. Green, S.I., et al., *Simulation of the flow through woven fabrics.* Computers & Fluids, 2008. **37**(9): p. 1148-1156.

74. Cengel, Y. and J. Cimbala, *Fundamentals and Application*. 2006: McGraw-Hill, USA.

75. Fung, Y.-c., *A first course in continuum mechanics.* Englewood Cliffs, NJ, Prentice-Hall, Inc., 1977. 351 p., 1977.

76. Temam, R., *Navier-stokes equations*. Vol. 2. 1984: North-Holland Amsterdam.

77. Kozeny, J., W. Striedieck, and M.R.J. Wyllie, *Concerning Capillary Conduction of Water in the Soil:(Rise, Seepage and Use in Irrigation)*. 1927: Petroleum Branch of the American Institute of Mining and Metallurgical Engineers.

78. Stanton, T.E. and J.R. Pannell, *Similarity of motion in relation to the surface friction of fluids.* Philosophical Transactions of the Royal Society of London Series a-Containing Papers of a Mathematical or Physical Character, 1914. **214**: p. 199-224.

79. Blake, F., *La perte de charge d'un fluide traversant un lit de particules.* Trans. Amer. Inst. Chem. Engrs, 1922. **14**: p. 415.

80. Chilton, T.H. and A.P. Colburn, *II—Pressure Drop in Packed Tubes1.* Industrial & Engineering Chemistry, 1931. **23**(8): p. 913-919.

81. Leva, M. and M. Grummer, *Pressure Drop through Packed Tubes .3. Prediction of Voids in Packed Tubes.* Chemical Engineering Progress, 1947. **43**(12): p. 713-718.

82. Ergun, S., *Fluid Flow through Packed Columns.* Chemical Engineering Progress, 1952. **48**(2): p. 89-94.

83. Gedeon, D. and J. Wood, *Oscillating-flow regenerator test rig: hardware and theory with derived correlations for screens and felts.* 1996.

84. Tanaka, M., I. Yamashita, and F. Chisaka, *Flow and heat transfer characteristics of the Stirling engine regenerator in an oscillating flow.* JSME international journal. Ser. 2, Fluids engineering, heat transfer, power, combustion, thermophysical properties, 1990. **33**(2): p. 283-289.

85. Costa, S., et al., *Numerical study of the heat transfer in wound woven wire matrix of a Stirling regenerator.* Energy Conversion and Management, 2014. **79**: p. 255-264.

86. Kuehl, H.-D., S. Schulz, and C. Walther, *Theoretical models and correlations for the flow friction and heat transfer characteristics of random wire regenerator materials*. 1998, Univ. of Dortmund (DE).

87. Gedeon, D., *Sage User's Guide.* Gedeon Associates, Athens, OH, 2011.

88. Thomas, B., *Evaluation of 6 different correlations for the flow friction factor of stirling engine regenerators*. 1999, SAE Technical Paper.

89. Thomas, B. and D. Pittman. *Update on the evaluation of different correlations for the flow friction factor and heat transfer of Stirling engine regenerators*. in *Energy Conversion Engineering Conference and Exhibit, 2000.(IECEC) 35th Intersociety*. 2000. IEEE.

90. Mehta, D. and M. Hawley, *Wall effect in packed columns.* Industrial & Engineering Chemistry Process Design and Development, 1969. **8**(2): p. 280-282.

91. Ibrahim, M.B., et al., *Computational modeling of a segmented-involute-foil regenerator for Stirling engines.* Journal of Thermophysics and Heat Transfer, 2009. **23**(4): p. 786-800.

92. Calis, H.P.A., et al., *CFD modelling and experimental validation of pressure drop and flow profile in a novel structured catalytic reactor packing.* Chemical Engineering Science, 2001. **56**(4): p. 1713-1720.

93. Petre, C.F., et al., *Pressure drop through structured packings: Breakdown into the contributing mechanisms by CFD modeling.* Chemical Engineering Science, 2003. **58**(1): p. 163-177.

94. Huang, Z., et al., *Numerical simulation of the flow around rows of cylinders.* Computers & Fluids, 2006. **35**(5): p. 485-491.

95. Atmakidis, T. and E.Y. Kenig, *CFD-based analysis of the wall effect on the pressure drop in packed beds with moderate tube/particle diameter ratios in the laminar flow regime.* Chemical Engineering Journal, 2009. **155**(1-2): p. 404-410.

96. Costa, S.C., et al., *The thermal non-equilibrium porous media modelling for CFD study of woven wire matrix of a Stirling regenerator.* Energy Conversion and Management, 2015. **89**: p. 473-483.

97. Dybbs, A. and R. Edwards, *A new look at porous media fluid mechanics—Darcy to turbulent*, in *Fundamentals of transport phenomena in porous media*. 1984, Springer. p. 199-256.

Appendix A

The critical values of y_{i4} and y_{i5} for grouping in present study, i.e., b_{i1} and b_{i2}, and c_{i1}, c_{i2} and c_{i3}

Θ	b_{i1}	b_{i2}	C_{i1}	C_{i2}	C_{i3}
60°	1302.5	4570	724400	532350	485275
70.3°	5906.25	18057.5	1208400	846250	825250
80°	50486.25	94876.25	2207750	1199750	1817500

Appendix B

The specific expression of y_{ijk}

$$
\begin{aligned}
y_{ijk} = {} & a_{ijk1} + a_{ijk2}x_1 + a_{ijk3}x_2 + a_{ijk4}x_3 + a_{ijk5}x_4 + a_{ijk6}x_1x_2 + a_{ijk7}x_1x_3 + a_{ijk8}x_1x_4 \\
& + a_{ijk9}x_2x_3 + a_{ijk10}x_2x_4 + a_{ijk11}x_3x_4 + a_{ijk12}x_1^2 + a_{ijk13}x_2^2 + a_{ijk14}x_3^2 \\
& + a_{ijk15}x_4^2 + a_{ijk16}x_1x_2x_3 + a_{ijk17}x_1x_2x_4 + a_{ijk18}x_2x_3x_4 + a_{ijk19}x_1^2x_2 \\
& + a_{ijk20}x_2^2x_1 + a_{ijk21}x_1^2x_3 + a_{ijk22}x_3^2x_1 + a_{ijk23}x_1^2x_4 + a_{ijk24}x_4^2x_1 \\
& + a_{ijk25}x_2^2x_3 + a_{ijk26}x_3^2x_2 + a_{ijk27}x_2^2x_4 + a_{ijk28}x_4^2x_2 + a_{ijk29}x_3^2x_4 \\
& + a_{ijk30}x_4^2x_3 + a_{ijk31}x_1^3 + a_{ijk32}x_2^3 + a_{ijk33}x_3^3 + a_{ijk34}x_4^3 + a_{ijk35}x_1x_2x_3x_4 \\
& + a_{ijk36}x_1^2x_4^2 + a_{ijk37}x_2^2x_4^2 + a_{ijk38}x_3^2x_4^2 + a_{ijk39}x_1^3x_4 + a_{ijk40}x_4^3x_1 \\
& + a_{ijk41}x_4^3x_2 + a_{ijk42}x_1x_2^{-1} + a_{ijk43}x_2x_1^{-1} + a_{ijk44}x_1x_3^{-1} + a_{ijk45}x_3x_1^{-1} \\
& + a_{ijk46}x_2x_3^{-1} + a_{ijk47}x_3x_2^{-1} + a_{ijk48}x_4x_1^{-1} + a_{ijk49}x_4x_2^{-1} + a_{ijk50}x_4x_3^{-1} \\
& + a_{ijk51}x_2x_4x_1^{-1} + a_{ijk52}x_3x_4x_1^{-1} + a_{ijk53}x_1x_3x_2^{-1} + a_{ijk54}x_3x_4x_2^{-1} \\
& + a_{ijk55}x_4^2x_1^{-1} + a_{ijk56}x_4^2x_2^{-1} + a_{ijk57}x_2x_3x_4x_1^{-1} + a_{ijk58}x_1x_3x_4x_2^{-1} \\
& + a_{ijk59}x_4^2x_2x_1^{-1} + a_{ijk60}x_4^2x_3x_1^{-1} + a_{ijk61}x_1^2x_3x_2^{-1} + a_{ijk62}x_1^2x_4x_2^{-1} \\
& + a_{ijk63}x_4^2x_1x_2^{-1} + a_{ijk64}x_4^2x_1x_3^{-1} + a_{ijk65}x_4^2x_2x_3^{-1} + a_{ijk66}x_2x_3x_1^{-2} \\
& + a_{ijk67}x_2x_4x_1^{-2} + a_{ijk68}x_1x_4x_2^{-2} + a_{ijk69}x_3x_4x_2^{-2} + a_{ijk70}x_1x_3x_2^{-2} \\
& + a_{ijk71}x_1x_4x_3^{-2} + a_{ijk72}x_4^2x_1^{-1}x_2^{-1} + a_{ijk73}x_4x_1^{-1}x_2^{-1}x_3^{-1} + a_{ijk74}x_4x_2^{-2}x_1^{-1} \\
& + a_{ijk75}x_1x_2^{-2}x_3^{-1}
\end{aligned}
$$

Values of a_{ijkl} as i=1 and k=1

l	j=1	j=2	j=3	j=4	j=5
1	28.23	35.99402	12.56647	1.32374	104.8189
2	-40.9077	-32.6324	-11.7312	0.708423	1665.616
3	7.63468	3.866561	1.99634	-0.49542	-72.545
4	-3.0944	-9.24931	-4.36252	-1.71739	-99.0788
5	29.78426	-136.197	-44.257	-20.3448	2945.061
6	-0.21917	-0.82237	-0.20339	0.140804	-404.767
7	35.34071	26.41394	9.635051	-1.54527	1335.106
8	51.36851	175.7436	58.14958	11.79565	-6140.3
9	-4.52572	-2.04475	-1.26359	0.569787	-210.871
10	2.087082	-12.1232	-5.65112	-1.23853	-423.583
11	55.27897	195.8938	64.48311	18.16965	-791.511
12	-5.46501	2.668212	-0.04625	0.916841	-1854.57
13	-0.70347	-0.22078	-0.04832	-0.03446	78.87212
14	9.233851	11.29939	4.645505	1.148927	100.3261
15	-12.394	245.0451	89.50229	-4.53348	87.66724
16	-1.58369	-0.28534	-0.11357	0.029615	73.92053
17	3.085067	-4.13019	-0.98236	-0.00752	-77.6218
18	16.35797	8.8335	3.778076	-0.03804	266.5998
19	1.066942	0.300541	0.095688	-0.058	48.18782
20	-0.01093	0.057957	0.015715	-0.00146	26.52366
21	4.453466	-1.52604	-0.05741	-0.12247	-46.2529
22	-7.61603	-4.7898	-1.91222	0.240206	-515.293
23	-39.5626	-101.202	-32.641	-11.6083	6833.593
24	529.3335	486.1176	149.9796	-10.7394	-8155.13
25	0.341427	0.16848	0.043641	-0.02194	-3.92168
26	0.616941	-0.03119	0.16161	-0.08744	51.7641
27	-1.47261	-0.10787	0.014523	0.159816	52.89483
28	-41.9395	-19.5701	0.853835	7.400561	5462.971
29	-9.22032	-47.4212	-15.6989	-4.5309	293.8602
30	35.74728	-173.873	-58.6381	-17.6124	-768.533
31	-1.00824	-0.28852	-0.00654	-0.22615	529.9474
32	0.02997	-0.00037	-0.00097	0.004633	-6.46757
33	-2.34934	-2.41878	-1.02833	-0.25363	-1.67825
34	-32.503	85.39849	26.45575	78.03599	1726.547
35	-8.27196	-1.49208	-1.14913	0.377395	-172.113
36	-184.567	-131.314	-51.727	1.379123	-1086.32
37	8.292805	5.963372	1.935167	-1.55795	-264.677
38	12.19523	90.05132	31.88809	11.33279	496.4793
39	22.81911	34.5481	12.25171	3.618047	-2130.87

40	970.0411	1522.557	568.5461	94.91025	5046.887
41	-140.678	-351.424	-135.497	41.06342	-5355.96
42	10.53858	5.326543	1.828653	0.08469	3165.68
43	-0.31691	-0.38451	-0.11779	0.052748	19.37514
44	20.14166	13.83045	5.750368	-0.81444	781.2651
45	-0.28819	-0.23104	-0.07197	0.021448	-6.00839
46	-1.50837	-1.10029	-0.76555	0.234897	-126.703
47	-0.10014	0.051452	0.016063	-0.02019	9.445314
48	-5.58392	-2.11445	-0.89122	0.409096	-277.424
49	3.295729	5.859249	1.696565	0.06288	-139.92
50	25.00267	78.4847	27.60681	8.099292	-396.917
51	-1.38719	-0.01241	0.119531	0.590716	132.4424
52	2.692792	0.554518	0.253069	-0.16105	114.0217
53	-4.49526	-3.25888	-0.95101	-0.08737	-301.71
54	-10.9922	-8.0981	-2.34397	0.043445	-462.363
55	-6.6669	-14.7467	-4.24534	0.295378	533.3494
56	-1.49719	-28.9307	-10.3794	-0.77007	-545.06
57	-6.26864	-3.31576	-1.10057	0.190218	-158.111
58	25.49023	23.93235	6.530369	-2.27537	381.1511
59	15.14217	4.259784	-0.87479	1.259734	-1391.18
60	-2.55253	-1.62555	-0.83867	0.074818	64.45783
61	-4.60883	-1.20248	-0.3125	0.650703	750.2297
62	-16.6978	-54.0811	-16.6718	-2.64468	-701.043
63	-9.94864	77.47064	30.14456	1.690289	111.4427
64	-108.477	-270.701	-89.7889	-20.3701	4565.428
65	-6.36083	39.24178	14.09528	-0.92074	-1003.83
66	0.004771	0.003884	0.000999	-0.00011	-0.35506
67	0.331522	0.103213	0.038135	-0.04719	11.06315
68	-0.9275	-0.49023	-0.05543	0.277181	45.67191
69	0.48258	0.187837	0.050691	0.018287	62.57093
70	0.217092	0.139941	0.037678	0.012317	-88.4372
71	7.876726	16.15563	4.475112	2.804682	17.47823
72	0.722164	2.488496	0.799264	-0.12852	-33.7303
73	-0.07965	-0.17531	-0.04679	-0.00605	22.04512
74	0.031984	0.013472	0.004548	-3.55E-05	-0.86483
75	-0.75203	-0.39738	-0.13306	-0.01879	-141.709

Values of a_{ijkl} as i=1 and k=2

l	j=1	j=2	j=3	j=4	j=5
1	36.86408	43.5854	13.88885	0.698291	757.1208
2	1.122146	-21.1108	-5.01303	0.92941	1936.946
3	8.237129	16.10938	0.621224	-0.85892	542.6326
4	-12.9307	-22.6645	-5.93815	-1.11227	-1434.1
5	6.808913	-99.4752	-48.0558	-19.4127	3782.904
6	-2.32757	-3.37986	-0.65859	-0.01346	-2107.2
7	-1.27131	23.02414	5.516689	-1.00733	1830.376
8	92.68097	67.79404	24.74579	-8.87789	-5801.27
9	-0.00145	-12.4398	-0.24025	0.915931	-441.728
10	-23.9077	-2.83413	-4.32022	4.655952	889.0756
11	87.22948	210.8328	84.27828	20.49507	-5956.74
12	2.422019	1.352431	0.200125	1.32676	197.3057
13	-3.8091	0.603618	0.136124	-0.14456	186.9761
14	14.39132	21.07138	5.587403	0.553288	928.3904
15	214.5595	187.1196	77.68017	13.93824	-5566.52
16	-0.5076	-1.42125	-0.3352	-0.24091	-362.389
17	-8.1473	-13.3361	-6.45604	0.25548	2674.753
18	28.99698	9.749945	2.190639	-0.76221	744.3483
19	1.930444	0.243792	0.098938	-0.24601	-249.547
20	-0.25097	1.019683	0.202941	0.15917	623.3091
21	-0.78139	0.39603	-0.06187	0.290823	501.6903
22	1.715351	-5.22229	-1.06915	0.104082	-423.319
23	-64.4817	-52.9345	-11.3003	-2.22152	-258.824
24	589.2675	487.6364	131.7514	19.03335	-1411.74
25	1.017367	0.551195	0.197523	-0.03168	26.06381
26	-1.34555	2.480126	-0.25317	-0.10814	88.91014
27	-0.8886	-1.89523	0.92278	-0.49215	-719.672
28	-133.916	2.998466	33.7118	-3.65897	17439.33
29	-20.9438	-52.6391	-20.9292	-5.51298	1667.654
30	-144.576	-167.169	-78.5495	-34.0728	193.4561
31	-1.29048	-0.32594	-0.04813	-0.31802	40.45531
32	0.591861	-0.335	-0.10021	0.017771	-68.8156
33	-3.17853	-4.73227	-1.16921	-0.10567	-197.864
34	45.67663	185.8699	90.92057	77.21417	6282.738
35	-2.05919	7.714543	1.858256	1.033978	-434.556
36	-110.33	-161.217	-47.0354	-4.15884	278.2759
37	12.6594	5.346666	-2.53705	-1.70713	-2850.95
38	59.69611	113.0206	45.40844	16.4772	-1823.15
39	23.80789	21.16259	5.341529	0.722254	-669.054

40	717.5634	1427.869	498.6612	29.5213	15604.52
41	-28.8503	-388.243	-144.204	75.14435	-18200.3
42	5.075161	0.221491	0.909754	0.39199	3229.457
43	-1.24052	-0.48297	-0.15689	0.073156	-10.0729
44	-3.43744	9.845731	2.628276	-1.15241	521.6984
45	-0.73105	-0.24287	-0.08647	0.040255	-1.58552
46	0.912897	-6.86877	-0.35866	0.553678	-346.995
47	0.62654	-0.1356	-0.02399	-0.01059	-8.12201
48	-1.40574	-10.699	-2.42531	0.271089	199.4184
49	8.567681	10.93099	2.956618	-0.11862	460.1588
50	-9.60759	66.61773	29.71416	7.804618	-1825.68
51	8.200975	-0.13996	-0.3302	-0.12668	246.1998
52	1.365429	3.315668	0.395903	0.04086	-42.6699
53	-3.57801	-1.56614	-0.80667	0.327066	-71.0718
54	-10.2922	-13.0712	-4.59266	-0.66753	122.9349
55	-35.4792	16.21102	7.720064	-0.16547	941.0548
56	-31.1932	-24.4414	-9.55596	0.788294	4011.353
57	-8.66778	-5.90469	-1.32009	0.172407	-93.0801
58	12.7444	18.89714	6.16845	0.61562	1736.494
59	8.664251	-20.8891	-13.7026	2.168546	-2436.25
60	7.482441	-17.3182	-5.39917	-0.67983	778.2772
61	0.494273	-0.83321	-0.04937	-0.36453	-574.05
62	-18.3336	-13.6309	-7.05498	1.826218	2246.269
63	38.49673	42.68334	23.72827	-10.198	-7962.38
64	-335.348	-237.476	-80.3895	-10.5881	-1662.63
65	82.45436	71.22686	17.52674	-7.67133	-2430.2
66	0.087959	0.006823	0.003372	-0.0017	0.66021
67	-0.31333	0.799874	0.237152	-0.01642	-14.7146
68	0.194336	-2.53274	-0.70136	0.168854	-146.547
69	0.535104	0.664426	0.30513	0.122209	-177.394
70	-0.04643	0.339608	0.08381	-0.07354	-75.9305
71	49.63276	30.50927	9.753522	3.23829	913.0959
72	6.501381	-0.05367	-0.45589	0.041592	-672.268
73	0.307986	-0.07473	-0.26794	-0.00336	-77.728
74	-0.27016	0.114285	0.089439	-5.47E-03	27.72625
75	-0.34941	-0.05009	-0.074	-0.01785	-193.189

Values of a_{ijkl} as i=1 and k=3

l	j=1	j=2	j=3	j=4	j=5
1	18.07127	25.02971	9.616134	4.160998	-4.03223
2	-157.907	-216.934	-79.6912	19.76385	902.4583
3	9.895936	9.030124	4.935832	0.578186	-47.7689
4	13.51133	10.3986	0.809594	-7.67301	125.7869
5	75.94297	33.53006	12.72815	-1.37914	-316.005
6	-2.39674	-4.39583	-1.52341	-1.94567	-375.451
7	112.0982	154.6691	56.58033	-9.87768	808.504
8	94.58635	88.68298	27.97284	-57.7296	-3029.85
9	-4.53811	-5.64882	-3.42161	-0.16014	-67.9081
10	-2.07836	2.122603	0.815855	-0.80869	-17.2165
11	24.60806	70.39745	25.42362	21.58584	1112.163
12	-16.9895	-32.0159	-10.5211	5.224867	-413.365
13	-0.64402	0.172031	0.079185	0.044532	32.85925
14	-5.85953	-5.60976	0.113242	4.975212	-96.2862
15	81.07676	129.1863	53.17686	-2.06514	1809.521
16	-1.31872	-1.39934	-0.51961	0.570616	46.87527
17	-0.08295	2.355686	0.812549	2.20367	119.3403
18	13.93341	17.01427	6.045673	1.064092	109.9345
19	-0.376	-0.11741	0.024357	-0.62264	39.31706
20	0.541589	0.819753	0.279408	0.204727	19.57408
21	11.48162	25.67062	9.491001	-3.20658	54.57655
22	-21.6039	-28.99	-10.8775	1.723706	-296.003
23	51.8792	169.8718	54.43747	65.5585	1716.395
24	669.7018	725.4401	271.1229	24.92623	3025.597
25	0.076059	0.036859	0.010664	-0.07234	-3.33807
26	0.724795	0.798268	0.666104	0.102748	23.00142
27	-1.33524	-2.25342	-0.77867	-0.14147	-2.91924
28	-43.0235	-83.6098	-31.3468	27.92367	-541.659
29	-18.0374	-31.5503	-11.7312	-7.41256	-546.134
30	-50.6641	-44.2117	-27.1294	-18.0849	-2952.26
31	-8.77869	-23.6279	-8.55814	-9.29682	-82.2821
32	0.040322	-0.02492	-0.01019	0.001787	-2.30945
33	1.410066	1.657418	0.06376	-1.05523	28.57041
34	-42.6355	-26.9097	-11.452	10.17504	2.847336
35	-11.4581	-20.9218	-7.48335	1.178424	-82.9801
36	-424.159	-774.718	-261.532	-226.625	-2272.66
37	4.875998	9.767018	3.59819	-2.30589	62.48544
38	37.75387	35.18873	17.10641	15.1671	1391.885
39	62.56366	105.3057	36.80196	31.94514	17.86671

40	1026.115	1394.611	436.7217	604.1047	-3166.61
41	-68.1418	-140.193	-47.6585	-35.9751	225.9109
42	2.46895	-27.6812	-10.0231	-1.25396	3025.649
43	-0.17175	-0.1159	-0.03601	0.051748	4.490649
44	85.5847	126.1852	46.22406	-10.117	854.5826
45	-0.23039	-0.22608	-0.07499	0.058099	-3.67047
46	-3.36332	-5.39798	-2.67435	-0.3019	-47.37
47	0.248788	0.673348	0.216112	-0.24016	5.110019
48	-4.86005	-5.95157	-2.08956	-0.2622	-78.0301
49	-0.04128	8.182362	3.209028	-1.268	-202.268
50	-15.7411	15.1576	3.917473	2.119562	199.9156
51	-0.90037	-1.82482	-0.62294	-0.17715	20.70215
52	2.692826	3.323522	1.182358	0.02239	57.65665
53	23.99773	41.36793	14.25765	-1.64548	469.0433
54	-10.1064	-18.3036	-6.40481	0.876116	-185.692
55	-0.06706	-4.00025	-1.42943	1.968361	43.88096
56	-20.924	-33.5036	-11.7769	1.724351	62.90646
57	-1.41518	-1.90336	-0.68495	0.032677	-24.9466
58	30.1893	72.22127	24.4012	-7.40667	-238.629
59	0.497066	1.238329	0.520047	-1.27044	-19.633
60	-2.55709	-1.03278	-0.39677	-1.15941	-17.5735
61	-43.6161	-83.0247	-29.3341	7.441716	143.6946
62	5.092311	99.8803	36.52632	-26.7797	597.5182
63	24.92125	120.2923	54.38853	11.61977	-1542.43
64	-390.102	-312.987	-104.218	-111.926	1844.554
65	22.41094	35.98604	12.24406	3.685402	-8.76916
66	0.002555	-5.77E-05	-5.43E-05	-0.00138	0.008433
67	0.082399	0.124987	0.043343	0.004995	0.219622
68	1.980883	-7.39875	-3.35066	-1.31344	162.9126
69	1.576791	2.527064	0.885242	-0.07926	45.84766
70	-4.04805	-5.65826	-1.87832	0.69341	-182.34
71	14.80963	-20.4037	-8.31403	26.42803	-637.418
72	0.960613	1.300443	0.456837	-0.13605	-8.36214
73	0.333695	0.477206	0.168678	-0.02687	13.11555
74	-0.06192	-0.10966	-0.03933	1.02E-02	-1.31802
75	0.126745	2.609027	0.9806	0.447009	-142.398

Values of a_{ijkl} as i=1 and k=4

l	j=1	j=2	j=3	j=4	j=5
1	39.82987	52.48462	19.3183	8.478699	405.1424
2	-34.9334	-73.418	-38.8422	74.70213	2150.118
3	11.30915	17.15405	8.217191	1.881927	-484.296
4	-13.3135	-19.6451	-10.4029	-12.0053	-738.332
5	49.35719	-41.3291	-3.30491	-74.4787	5549.748
6	-20.2013	-36.3983	-13.7928	-1.39927	-1026.21
7	34.6554	80.70037	38.42618	-52.4677	16.22862
8	12.03014	185.5228	48.46564	94.26647	-2043.81
9	-3.89794	-12.9244	-6.68539	1.045489	246.9179
10	-7.5997	-66.212	-19.5446	-24.7379	-315.347
11	64.71826	161.1955	50.88903	60.76207	-3129.47
12	29.34701	14.86882	6.434619	2.244969	167.5182
13	0.726471	5.161353	2.065507	-0.94209	125.4517
14	11.54332	13.13172	7.253112	7.113312	559.6755
15	145.3617	365.9742	128.7272	131.0426	-998.647
16	-1.11036	-1.16385	-0.25022	1.068445	95.10265
17	29.25984	59.12439	21.06662	-1.10704	-66.8575
18	19.96626	28.50486	8.618476	1.157484	187.6231
19	1.539681	-3.1314	-0.95797	-0.2662	119.3777
20	2.516523	6.180149	2.288268	0.192462	104.9174
21	8.081755	12.50422	4.012765	-1.34682	170.3408
22	-4.68992	-14.5089	-7.22418	11.09071	-70.3999
23	-93.4272	-115.703	-40.5614	67.30781	1115.838
24	566.4118	66.92813	68.30293	-497.717	3175.601
25	0.051883	-0.03084	-0.01439	0.086917	-14.9378
26	0.159645	2.149671	1.307304	-0.42753	-57.2585
27	-2.73848	3.5841	1.160585	2.136613	53.70083
28	56.87068	193.3241	66.65922	97.24947	-743.762
29	-24.1789	-62.4003	-21.0126	-18.7058	590.8181
30	-82.5728	-232.173	-94.5545	-65.9399	-1903.11
31	-19.8201	-3.78211	-1.8869	-7.74209	-581.078
32	-0.2006	-1.09275	-0.42581	0.079558	-17.7825
33	-2.17763	-1.83581	-1.33869	-1.19474	-142.248
34	-88.3595	-113.555	-37.5683	-55.7633	-757.023
35	-16.0941	-27.4677	-9.82361	-0.2286	-207.764
36	-298.079	-224.81	-78.5042	-173.237	-5174.76
37	-1.22712	-23.3786	-8.11769	-8.02245	247.9222
38	43.15532	109.5839	44.36843	27.9579	1301.574
39	76.56112	46.70914	16.98937	20.78243	1306.685

40	1400.261	2299.007	737.1123	1073.073	-1389.85
41	-196.135	-418.576	-147.535	-34.0096	76.77042
42	3.252918	-30.1735	-11.1654	5.449804	2684.995
43	-0.99035	-1.03679	-0.3059	-0.42218	6.984278
44	13.09606	38.12571	21.55152	-53.6102	837.9632
45	-0.81714	-0.32191	-0.07729	-0.17048	-0.2723
46	-3.41193	-9.28415	-4.52474	2.099466	49.90395
47	1.918573	0.591155	0.1226	0.482045	-15.8518
48	-7.01442	-11.2303	-4.18999	2.04797	-161.424
49	-1.1469	9.577415	3.833097	-3.01041	-331.051
50	-13.7486	18.6821	3.190477	9.685795	-1775.78
51	-0.5335	1.079569	-0.30715	3.022768	24.75432
52	2.862489	2.709803	0.937199	-0.28036	94.43346
53	-2.89756	7.884431	2.57988	-3.46642	520.3489
54	-6.97373	-2.90145	-0.672	-0.70446	-215.565
55	4.409954	5.588265	2.538581	0.006425	388.8223
56	-15.4604	-45.3444	-16.3561	2.907709	572.692
57	-3.79454	-2.13441	-0.47174	0.444081	-46.4812
58	44.97289	45.57204	14.34165	5.359798	-416.725
59	-8.08189	-22.4659	-7.53507	-8.00566	-164.346
60	-4.65382	-5.90763	-2.2603	-1.1278	-105.409
61	-14.8146	-22.0302	-7.60377	0.842923	-116.594
62	23.40391	20.49046	6.913082	-6.93147	660.528
63	-57.2219	116.4302	53.37559	-19.5073	-1163.01
64	-450.284	-553.312	-177.746	-194.501	3219.586
65	1.994232	32.65584	8.690272	-8.35108	517.0117
66	0.062591	2.82E-03	-2.86E-03	0.02269	-0.27168
67	0.404394	0.800989	0.306744	-0.13063	2.328679
68	8.290659	-0.47047	-0.78849	1.368475	-0.90013
69	0.112276	-0.05207	-0.03882	0.109751	47.08958
70	-2.0505	-1.14351	-0.27896	-0.38553	-122.398
71	83.17833	93.32475	26.68184	68.5245	-1404.24
72	0.858971	1.635329	0.549622	-0.04405	-54.6214
73	-0.04001	-0.04724	-0.02166	-0.06803	12.13317
74	0.033351	0.023718	0.009422	2.38E-03	0.33256
75	-0.89968	1.520791	0.588433	-0.15663	-94.4888

Values of a_{ijkl} as i=1 and k=5

l	j=1	j=2	j=3	j=4	j=5
1	19.84074	32.39815	11.74727	5.447394	119.5417
2	-167.469	-172.508	-58.089	-62.5306	1851.276
3	5.427721	-9.31008	-3.04996	2.198809	-86.932
4	13.21274	1.171337	-1.05009	-14.1345	-100.395
5	74.33839	185.4033	66.32599	20.4493	291.1677
6	-13.0996	-6.66109	-2.925	3.174256	-275.445
7	154.0666	227.0923	79.95193	54.43851	66.05346
8	139.5144	43.79244	7.569063	-148.364	-2128.06
9	-8.73245	-10.0384	-3.95307	-3.1255	-33.5266
10	8.997433	48.7804	18.25897	17.4811	45.86463
11	32.74686	-92.0629	-35.6309	18.9186	-243.184
12	-121.522	-310.845	-105.02	-62.7205	-492.6
13	1.525768	4.007537	1.445283	0.132726	29.84675
14	-2.42898	11.46572	5.211132	11.17041	43.4071
15	-3.55265	-88.3165	-23.218	6.342839	-316.79
16	2.648622	-1.55081	-0.50719	0.609508	1.195028
17	-17.6967	-74.2891	-24.7072	-8.49732	131.2431
18	15.34442	12.50332	4.038069	2.667391	41.81792
19	-0.55371	0.395959	0.018946	0.405622	15.43242
20	1.945257	3.405858	1.216305	0.041942	15.48407
21	10.73975	20.49193	7.433546	-0.25561	119.6481
22	-25.5188	-42.0012	-15.2578	-8.09347	-93.4632
23	251.1057	972.6941	321.0823	337.1123	274.0776
24	487.83	649.3719	249.8915	206.3852	-252.481
25	-0.0072	0.264766	0.093769	0.05025	-4.08618
26	0.913781	1.063257	0.531029	0.160203	19.48256
27	-2.70712	-6.10951	-2.11456	-2.28596	-2.74353
28	-30.9319	-116.943	-44.2685	-10.666	-224.536
29	-27.9163	11.18354	5.659582	-14.3126	-34.1592
30	-41.5501	118.9893	37.78268	-25.352	693.641
31	35.07895	35.61885	13.56671	-13.1069	135.6095
32	-0.12431	-0.36396	-0.13129	0.00837	-1.84802
33	1.561424	-2.74749	-1.33936	-1.7864	-10.9624
34	43.08213	15.92684	-1.52044	36.64037	-393.336
35	-16.89	-13.4058	-4.71699	-3.97602	30.82217
36	-217.94	-871.138	-276.139	-473.933	510.2516
37	4.999037	14.63565	5.030172	3.672417	-7.94765
38	26.83978	-27.27	-9.49235	18.0252	-44.2877
39	-42.2179	-50.3968	-20.4095	33.82031	-319.852

40	715.4577	337.684	52.4631	496.8071	-1315.2
41	-56.2672	-51.7968	-11.2658	-52.4211	318.6196
42	-43.2618	-131.745	-45.6082	3.827817	3083.335
43	0.523359	1.077947	0.372788	0.427772	3.997095
44	144.5738	190.2301	64.81265	47.2271	317.2888
45	-0.82802	-1.11751	-0.38072	-0.25927	-0.57888
46	-6.54711	-6.62343	-2.41929	-2.70398	-37.6131
47	4.204818	5.393185	1.886617	1.301147	-15.3259
48	-4.11526	-5.09513	-1.72158	0.560542	-52.5307
49	11.29168	26.37372	9.247135	-3.02715	-173.536
50	-16.3512	-25.3022	-10.6346	-6.32027	-15.9637
51	-3.56886	-6.87172	-2.32059	-2.61204	15.6699
52	3.297558	4.328771	1.437832	0.909724	39.33394
53	-15.1346	-4.28057	-2.64269	-32.0683	801.9216
54	-18.6737	-26.0179	-9.09711	-3.58061	-56.3524
55	-0.73683	-2.5807	-0.89374	-2.31392	64.76789
56	-43.868	-73.6251	-24.8932	2.881102	127.1112
57	-0.757	-0.73222	-0.26175	-0.01316	-8.46061
58	157.7653	201.8565	72.40885	61.71479	-710.523
59	3.763465	9.206854	3.148958	2.868375	-19.6992
60	-2.26786	-2.56818	-0.77837	-0.99489	-37.4938
61	-64.4857	-68.1859	-23.8777	-11.4154	-129.39
62	-57.7975	-151.014	-51.681	-4.63245	1137.691
63	172.584	638.094	237.5298	-61.1947	-517.133
64	-365.979	-24.5197	-6.69333	-81.3084	963.229
65	23.13317	21.08895	6.245276	7.059053	62.43948
66	0.002551	4.21E-03	1.53E-03	-0.00074	-0.06823
67	0.080147	0.088992	0.029264	0.016812	-0.04438
68	0.119557	-29.096	-11.7193	-2.87793	3.602539
69	1.725124	2.490168	0.877733	-0.01216	31.58673
70	-6.42603	-5.65638	-1.91152	1.838373	-201.984
71	-9.5009	-82.6123	-26.9522	-5.94437	-262.838
72	1.927897	2.850983	0.953238	0.420998	-7.21699
73	0.15208	0.122275	0.043852	-0.03693	7.278131
74	-0.11016	-0.16294	-0.05592	-1.21E-02	-0.67359
75	2.855444	10.11215	3.721186	1.986668	-114.085

Values of a_{ijkl} as i=1 and k=6

l	j=1	j=2	j=3	j=4	j=5
1	48.4471	3.289265	2.474363	11.57418	-46.6053
2	123.8078	-16.4851	-19.9127	70.86355	1076.191
3	-1.97083	-39.5595	-15.6001	12.49456	-355.44
4	-29.9215	15.46719	3.303958	-26.6595	206.165
5	-11.5416	72.16892	32.73848	-4.86812	2674.453
6	12.68362	23.90474	7.831505	-3.83952	-905.037
7	16.46896	227.4591	92.4862	-39.4699	1015.942
8	-102.885	-612.379	-221.083	-195.766	-103.898
9	-5.59734	-15.7467	-6.17919	-1.10627	34.84063
10	33.2988	256.2497	103.6123	-49.3471	362.89
11	103.4602	111.2433	24.00863	64.36499	-2169.82
12	-265.534	-587.607	-213.864	47.52657	-584.421
13	1.225871	12.76985	5.203621	-2.46993	140.8611
14	17.87416	-4.31544	0.384766	16.30405	-70.1776
15	221.2872	-1.82528	21.00567	-12.7127	-2348.19
16	-13.48	-10.9805	-3.68739	-1.24645	30.95652
17	-35.6574	-139.2	-50.555	19.56505	-152.679
18	7.518109	0.722682	0.322658	2.242278	18.48624
19	6.365367	6.563523	2.387256	-0.69798	78.42567
20	0.781167	5.083522	1.945399	-0.26046	125.529
21	6.899849	-2.01124	-0.33056	-1.80595	84.98486
22	9.678782	-33.2765	-14.7925	10.79551	-254.385
23	282.5861	1568.916	585.4667	-44.3059	656.3896
24	692.5782	999.8489	339.4673	326.2268	-1533.76
25	0.925283	1.204984	0.402776	0.179429	-1.22812
26	0.421367	1.392757	0.607447	-0.31343	-9.20404
27	-5.73789	-48.4033	-19.1852	7.198182	-91.9822
28	7.358227	-245.779	-114.386	158.5989	-977.845
29	-40.1439	-46.2892	-11.935	-28.6703	501.4929
30	-122.254	-26.73	-3.66314	-71.9008	1203.236
31	212.0197	254.5237	88.74095	-29.7051	215.6928
32	-0.21042	-1.20876	-0.4802	0.207935	-21.2808
33	-2.49844	3.166634	0.539003	-2.45398	6.604598
34	-14.0675	116.4108	12.44232	98.68894	785.4682
35	-3.0047	-0.19139	-0.3618	1.363305	-50.6047
36	63.40227	-1222.41	-463.578	-149.669	-174.682
37	11.26723	82.23344	32.3103	-15.253	224.639
38	41.18144	17.59205	4.547068	37.51346	-171.845
39	-377.561	-451.848	-158.145	66.95714	-413.153

40	874.0497	1495.829	518.7821	450.0894	-1543.83
41	-135.986	-326.213	-99.6037	-162.176	659.2775
42	-0.22197	-5.45526	-4.56787	10.46467	2865.635
43	0.429368	6.246041	2.365654	-0.42538	10.48474
44	-23.0134	152.8015	63.75495	-40.8216	1222.058
45	-1.01342	-2.07791	-0.65975	-0.03803	-10.7853
46	-3.95983	-11.4867	-4.73407	-1.60177	-9.21521
47	4.123743	7.823722	2.395952	-0.42458	-10.2518
48	-5.18239	-1.10722	-0.56132	0.26837	-8.1464
49	3.816743	1.939772	1.271621	-1.21125	-437.982
50	-19.9313	35.22723	7.525406	-4.50462	-588.68
51	-6.28571	-37.9401	-14.131	1.699657	-17.8088
52	2.528914	4.875621	1.713275	0.750364	69.9844
53	-24.287	-72.0193	-24.1357	-9.24247	259.1764
54	-5.83651	-16.6242	-5.25973	-0.4291	-19.0908
55	-4.75923	-20.4757	-6.93168	-1.24449	60.1661
56	-28.526	-21.3271	-7.57073	3.097943	645.2413
57	-0.87796	-0.21535	-0.02055	-0.31952	-10.2615
58	96.33755	199.1223	66.36466	10.94873	-242.175
59	3.459128	42.82872	16.05831	-3.65409	44.89201
60	-2.30875	-2.68084	-1.11218	-1.58307	-84.497
61	-27.8644	-15.2295	-5.75364	-1.52552	-34.6963
62	51.74896	-17.5916	-5.94312	5.266354	423.5252
63	-73.9337	7.897402	22.10302	-46.1193	-1256.88
64	-535.491	-150.2	-42.1126	-211.786	2526.912
65	-7.56158	3.7845	2.161664	3.482756	3.106267
66	0.03575	3.59E-03	-3.31E-03	-0.00542	0.198483
67	0.413656	0.632868	0.230409	0.058681	-2.33031
68	13.09682	-3.27119	-3.24912	-2.86066	-126.824
69	0.069282	0.059318	-0.00687	0.023986	16.23662
70	-4.66641	-1.45845	-0.03509	1.101372	-82.5214
71	123.0778	-20.5035	-12.3047	66.85362	-1067.71
72	1.837215	3.288998	1.148169	0.146074	-19.511
73	0.109104	-0.06322	-0.03146	-0.04274	4.038054
74	-0.04485	-0.08104	-0.02705	3.12E-05	0.602433
75	-1.30703	2.352394	1.269008	0.796669	-42.3428

Values of a_{ijkl} as i=2 and k=1

l	j=1	j=2	j=3	j=4	j=5
1	66.56627	101.6981	33.67868	5.290572	263.5964
2	-190.598	7.393353	-49.3396	0.607344	1924.034
3	53.47089	23.0294	8.498964	0.368753	81.89793
4	12.74035	-27.8902	-8.30025	-5.01055	-680.559
5	45.18042	-521.797	-37.3591	-111.563	6215.397
6	-5.15662	-2.0598	-0.59457	0.497123	-420.539
7	154.1281	-4.15222	40.22782	-7.7979	829.7971
8	315.3973	384.2145	138.2385	14.81604	-5382.26
9	-38.7555	-17.8222	-6.37882	1.051681	-259.435
10	13.33473	-40.2008	-15.6455	1.042801	-786.518
11	69.86974	697.0086	121.0843	115.3213	-3948.6
12	-12.165	3.461987	-0.411	5.463071	-1745.19
13	-1.55415	0.025529	-0.02578	-0.30344	71.14845
14	8.70773	34.89843	10.3857	3.655751	485.8344
15	23.96361	624.2946	251.8862	-31.1537	2170.215
16	-0.69132	-1.29411	-0.50215	0.475186	124.6533
17	20.78306	-2.85763	-1.43914	-3.2457	182.255
18	16.13307	32.56285	9.85576	0.099176	144.0579
19	1.384709	0.369368	0.153885	-0.14867	49.76455
20	0.264803	0.219226	0.058613	-0.0196	18.75026
21	5.179622	-4.34754	-0.33554	-1.30718	-96.3383
22	-33.9376	10.09999	-7.8498	1.176197	-381.446
23	-85.6475	-204.023	-62.153	-23.253	6207.135
24	980.4376	1763.164	506.2174	48.56657	-15243
25	0.808244	0.481854	0.160707	-0.08843	-9.33947
26	8.303521	2.906501	1.086518	-0.10643	62.0952
27	-2.26833	-1.30275	-0.20611	0.106147	83.37455
28	-121.534	-238.624	-43.6283	46.96081	6392.332
29	-19.0939	-184.2	-31.3955	-28.7704	1143.654
30	-14.1177	-300.592	-125.805	-36.2541	145.9062
31	3.028865	1.460061	0.609112	-1.76186	522.5568
32	0.046622	-0.05499	-0.01482	0.032537	-4.82179
33	-2.37525	-8.39174	-2.43371	-0.74109	-94.9504
34	126.3272	-38.5704	-24.7022	306.9854	-2448.83
35	-28.6588	-6.35962	-2.91716	1.412526	-168.062
36	-157.707	-397.512	-131.167	-71.3487	2285.079
37	21.24627	25.6907	9.169274	-4.32377	-466.009
38	59.65472	207.8429	80.5014	42.54838	786.9151
39	16.55637	68.82253	20.79457	15.32303	-2278.34

40	1257.045	3263.231	1264.942	705.0854	433.3496
41	-265.156	-1193.77	-487.407	11.09277	-3047.85
42	15.23953	10.47747	4.395029	-0.0025	6717.361
43	-1.4181	-1.49862	-0.50694	0.160488	19.80756
44	92.22183	-1.01242	21.8127	-3.42369	856.2535
45	-1.06764	-0.76362	-0.24686	0.101328	-3.77889
46	-17.7707	-9.27181	-3.4728	0.239347	-206.224
47	0.237378	0.534369	0.209261	-0.28077	1.127539
48	-7.84644	-16.7945	-5.834	1.496096	-350.262
49	11.9613	18.70488	7.123212	-1.6018	-257.067
50	101.7609	285.6179	43.60003	51.48126	-2068.67
51	-13.4533	-1.59307	-0.4295	-0.53074	322.3641
52	4.729971	6.559465	2.268866	-0.89617	174.6625
53	2.432952	-3.69622	-0.77428	-1.72227	-129.149
54	-29.6538	-22.6863	-8.31956	0.954462	-607.381
55	-38.5543	-29.9371	-9.71485	3.134159	1107.286
56	-38.7486	-102.665	-38.8092	-9.77519	-1001.87
57	-3.53033	-12.193	-3.76768	0.84628	-152.257
58	101.2306	79.83111	26.62059	-17.0986	-510.882
59	58.79701	6.370585	-3.48913	0.320662	-2039.23
60	5.959124	-12.2388	-3.73916	-2.8848	-207.074
61	-19.4131	-12.141	-4.92585	5.670814	756.1258
62	-89.0563	-107.433	-38.5308	-17.9689	-451.645
63	47.45986	412.1615	163.9448	5.013535	2024.446
64	31.63301	-715.431	-218.49	-106.891	4646.866
65	-118.908	206.7328	57.15116	5.458461	-638.13
66	0.025428	1.01E-02	3.65E-03	-0.00259	-0.36744
67	0.449433	0.687812	0.226613	-0.05463	3.38807
68	-2.5916	-8.38982	-3.0113	2.551375	8.303211
69	1.116823	0.970615	0.440887	-0.01482	128.2253
70	-1.17749	-0.09557	-0.14515	0.338941	-187.824
71	-79.7883	18.417	4.499892	12.44272	-368.436
72	4.913806	7.681183	2.591281	0.26952	-77.3036
73	-1.04727	0.500957	0.194854	-0.15401	43.69029
74	0.141008	-0.06165	-0.02691	1.59E-02	-4.16398
75	-0.70319	-0.81806	-0.3275	-0.13246	-237.211

Values of a_{ijkl} as i=2 and k=2

l	j=1	j=2	j=3	j=4	j=5
1	119.2682	122.4639	42.262	2.34039	-5.98622
2	60.57097	-103.265	-32.4321	3.023934	-4156.86
3	76.73049	16.29997	22.62491	-5.8697	1174.782
4	-91.8414	-66.3721	-24.2769	-1.67035	244.4165
5	33.58607	4.645917	-57.5223	-84.5374	5237.993
6	7.169061	-4.50428	-2.09615	0.985611	-2604.72
7	-18.0465	80.25065	26.77205	-3.80558	6721.734
8	114.8864	227.833	89.9513	-6.31236	-1462.36
9	-47.7436	-8.47953	-16.9525	5.190195	-753.819
10	-16.4192	-84.1687	-23.6432	2.259214	1086.115
11	206.9404	375.5322	170.1047	89.63116	-5276.31
12	5.585289	3.781906	2.120505	1.493655	41.35942
13	-13.9003	1.240058	0.031031	-0.22493	129.098
14	84.80828	65.7082	22.8927	0.61765	-421.851
15	-244.047	716.324	277.8906	92.27567	300.3392
16	-21.1378	-3.91653	-1.58266	0.191849	73.43496
17	-107.653	-27.3254	-11.8232	-2.99363	626.6996
18	47.1829	69.96917	19.39032	0.029486	-4.80271
19	-1.80006	1.192075	-0.20178	-0.06282	7.564053
20	4.823559	1.658739	1.032872	-0.19315	561.7323
21	0.684848	-1.76607	-0.0741	0.092534	-48.503
22	12.86314	-13.7628	-5.0286	0.127041	-1772.51
23	-62.4461	-114.207	-39.4493	-7.94823	605.8873
24	966.3743	1453.283	488.8577	-39.7415	11441.02
25	8.806881	1.866679	0.729747	-0.32922	9.125743
26	5.970941	-1.61527	3.423406	-0.95436	112.0471
27	-6.32269	-4.68104	-1.08855	0.766231	-120.4
28	-73.631	116.226	21.92894	72.70131	-11442.1
29	-55.3626	-104.46	-45.556	-25.6933	1550.309
30	488.3896	-452.908	-183.06	-132.159	-1915.79
31	2.057026	-0.81989	-0.2252	-0.69968	16.8841
32	0.394388	-0.90091	-0.28822	0.126002	-41.952
33	-19.6846	-15.9319	-5.49126	0.035747	178.4985
34	-16.6702	229.4072	119.0769	268.4895	-2030.6
35	66.00195	-2.11688	-0.6765	3.098906	-410.675
36	-246.292	-501.559	-169.34	-33.236	2257.262
37	-16.0457	36.44516	18.77307	-21.0317	1277.457
38	-93.0486	313.7953	115.5303	74.42121	1408.313
39	23.63438	56.96346	19.14499	5.090121	-327.094

40	2463.654	4718.767	1609.361	517.0335	-27323.9
41	-675.906	-2364.49	-818.6	205.0992	8770.973
42	29.84501	6.728473	2.733652	-0.08721	6193.44
43	-2.82359	-2.10666	-0.77369	0.41645	-6.40519
44	-54.0651	43.85166	12.79355	-2.7549	3757.164
45	-1.43381	-0.73432	-0.25298	0.091473	-2.19715
46	-19.2655	-8.49312	-9.09662	2.450216	-668.142
47	0.244847	-0.11973	-0.00169	-0.07685	-11.838
48	-22.5462	-30.6194	-8.73198	1.899971	41.7358
49	27.39865	18.28013	5.940247	-2.54719	-90.7245
50	3.140711	67.35295	51.71151	31.91432	-2163.78
51	11.00282	8.209723	0.066285	2.575591	-190.671
52	10.62556	10.96863	2.719208	-0.2635	46.28029
53	-21.5701	-7.65017	-2.09055	0.155201	-130.289
54	-37.3384	-26.0051	-7.5973	-0.09827	-40.6897
55	89.47518	36.06259	5.60292	5.92274	-1023.73
56	-20.0016	-68.1122	-27.828	-3.31476	-144.123
57	-21.255	-24.5866	-6.73334	1.215764	-80.3161
58	82.55718	60.75314	17.61563	-2.96724	-700.203
59	-126.875	-126.141	-35.832	-15.0496	3207.73
60	-46.7861	-35.386	-10.5564	-4.42537	-225
61	-6.67053	-1.33602	-1.24355	0.600739	107.5556
62	-51.6085	-61.3314	-23.2648	4.21105	-1343.65
63	4.655095	186.043	79.42624	-32.6324	1308.215
64	-723.251	-869.183	-271.911	-82.1516	1596.234
65	428.0929	376.9083	108.0509	-5.77827	-167.632
66	0.102739	1.55E-02	9.22E-03	-0.00532	0.281318
67	1.402037	2.064184	0.722737	-0.27858	3.786491
68	-5.45777	-6.11087	-1.64044	1.685243	-49.1488
69	0.86961	1.174441	0.314959	0.032989	25.27048
70	1.160526	0.8164	0.18682	0.011703	-125.92
71	162.4555	74.66074	22.18579	12.8434	-949.954
72	-4.66636	0.130885	0.941555	0.024817	176.5069
73	-1.04419	0.534672	0.042951	-0.1015	9.206418
74	0.236292	0.06068	0.025773	9.98E-03	-3.83087
75	-1.8817	-0.68265	-0.22343	-0.00867	-197.163

Values of a_{ijkl} as i=2 and k=3

l	j=1	j=2	j=3	j=4	j=5
1	28.36362	38.00989	13.27718	3.319324	151.2625
2	-781.932	-561.802	-224.261	-105.603	1653.619
3	30.27556	15.01958	6.322657	1.762615	-1.59243
4	60.04928	88.50135	27.67189	3.56497	-366.544
5	395.5943	-13.0445	22.52135	41.90993	941.111
6	-8.85894	-4.22009	-1.17925	-11.2724	-298.713
7	601.642	416.2318	167.3938	77.357	-164.236
8	160.4804	106.1773	47.6564	-342.397	-1509.47
9	-24.9837	-18.2773	-7.10793	-1.45017	-58.1741
10	12.27432	26.14097	9.721429	17.27675	-250.999
11	-208.913	230.5849	57.24042	72.25996	-303.812
12	-80.8638	-95.0531	-31.5144	19.15198	-452.558
13	0.011543	1.846329	0.575456	0.894402	24.39321
14	-23.5797	-55.1258	-16.7388	-3.46958	255.6616
15	-114.695	140.6762	68.40811	-100.465	2525.441
16	-7.80646	-15.0998	-5.54751	2.285082	85.17182
17	1.30597	-17.1819	-6.92067	17.57015	169.1318
18	27.21237	41.32249	13.34745	8.133574	64.40491
19	-1.85702	-1.0432	-0.22848	-2.48532	23.2507
20	2.103476	2.570749	0.879495	1.036396	12.32049
21	53.70935	108.3247	37.22416	-0.13439	-39.7832
22	-128.957	-72.4489	-30.6605	-14.0488	-98.7802
23	196.9969	121.347	20.44145	167.353	1924.343
24	1618.315	3281.473	1105.83	1226.949	-4262.38
25	0.26965	0.708344	0.285734	-0.23339	-5.90382
26	6.369099	3.336489	1.29386	0.077481	23.25601
27	-3.14805	-5.20591	-1.69242	-2.02644	13.56375
28	-189.968	-472.026	-164.922	-42.7504	734.7813
29	36.76748	-89.8676	-25.3168	-28.513	-86.8517
30	154.2662	-24.3909	-31.6574	-6.56642	-3833.71
31	-5.02407	-25.5551	-6.20529	-30.665	-17.504
32	-0.05589	-0.25883	-0.08895	-0.05514	-1.43939
33	2.525367	12.56082	3.790081	1.245554	-59.3525
34	71.60179	153.4185	40.75404	66.87542	-288.473
35	-33.1605	-52.8051	-17.6436	-7.62031	-81.9017
36	-768.873	-863.623	-234.098	-640.718	-2236.58
37	16.22186	40.40906	14.03456	0.129599	-26.6146
38	-8.49053	18.25199	13.30516	39.65477	1534.729
39	71.29848	129.9461	35.55438	97.89866	-23.1929

40	423.0773	-1683.66	-690.457	250.823	4925.173
41	-121.765	-154.254	-37.7113	-127.727	-37.8431
42	-22.7036	-129.039	-36.3902	-58.1291	7196.072
43	-0.404	-0.20063	-0.06614	0.379312	1.770017
44	434.6671	381.405	143.1538	88.12037	245.9121
45	-0.75515	-0.80206	-0.27983	0.255894	-5.45948
46	-13.3311	-13.7661	-5.0748	-4.10925	-47.6898
47	1.707805	4.452983	1.723883	-1.84924	18.91207
48	-16.3518	-22.2016	-7.34043	-4.01366	-47.706
49	8.507343	60.66037	20.72973	4.446486	-462.164
50	-46.8904	120.493	28.23627	14.15403	-615.635
51	-4.4168	-7.73708	-2.70752	-3.16517	57.11013
52	9.330991	10.75871	3.523633	1.663238	47.51993
53	86.73748	162.2158	48.18535	14.17388	286.1168
54	-34.1836	-67.592	-22.5485	-4.00268	-154.399
55	-2.20426	-23.2466	-8.18137	4.341882	85.81952
56	-84.2393	-195.723	-65.7463	-16.5791	481.3756
57	-3.59626	-5.33944	-1.72285	-0.75558	-23.2949
58	149.3369	344.0559	130.4885	-31.5065	-330.727
59	10.46605	22.53654	7.834974	1.56865	-73.2157
60	-6.10603	3.081599	1.174524	-4.41856	-9.03871
61	-187.173	-324.226	-113.127	-13.307	477.2938
62	146.4683	374.4672	135.9129	-33.819	38.73004
63	147.8411	839.1747	301.3496	297.8771	-4632.68
64	38.33855	58.66051	38.15899	-199.276	728.5345
65	39.83504	90.73224	27.41077	47.82257	-208.007
66	0.004313	-5.64E-03	-1.57E-03	-0.01214	0.131535
67	0.286316	0.47368	0.159135	0.101619	-0.99386
68	-0.81862	-43.0577	-15.2548	-29.4836	454.1127
69	6.038978	11.7958	3.962439	0.942531	59.95557
70	-16.6387	-30.4695	-10.7208	5.859674	-342.602
71	-225.903	-282.932	-98.9111	-40.7662	-158.668
72	4.528052	8.655871	2.908727	0.856827	-29.852
73	1.271537	2.362704	0.79315	0.149901	16.36006
74	-0.31835	-0.7486	-0.25365	-5.10E-02	-1.15464
75	2.269072	10.631	3.424216	6.795004	-334.548

Values of a_{ijkl} as i=2 and k=4

l	j=1	j=2	j=3	j=4	j=5
1	63.54933	94.40837	36.47133	18.66981	79.01635
2	-196.642	-315.723	-149.011	208.6868	815.1846
3	-36.3444	25.98999	17.98194	-0.53772	-186.859
4	33.78924	21.48121	-3.30942	-21.8127	84.70566
5	250.9765	-246.861	-30.0298	-95.0671	339.493
6	-20.7843	-78.8536	-29.1934	-30.0161	-1339.67
7	226.0599	294.4711	143.724	-110.3	694.9239
8	-111.807	-198.563	-132.81	-47.2478	885.1247
9	44.38347	-24.4157	-17.5369	-0.90649	130.0338
10	-120.31	-117.83	-29.607	-45.7684	-362.532
11	128.4857	701.5377	210.6497	103.6049	864.2317
12	-33.1578	-53.7029	-14.6017	23.39098	312.0661
13	-1.93407	14.83692	5.645277	2.578907	111.4777
14	-31.4746	-24.0355	-0.75161	14.40715	-180.859
15	-65.8611	378.3563	149.2125	171.4194	5085.001
16	-10.5121	0.179355	-0.45465	0.929214	323.5687
17	-12.714	45.05648	18.25757	56.17532	837.1872
18	52.27106	83.01338	31.17727	14.96918	260.9932
19	-1.18138	7.509593	2.161707	-8.5424	51.93012
20	5.9641	12.62925	4.742374	6.336416	109.4735
21	-1.27512	32.038	11.69834	1.095256	227.3373
22	-56.4621	-46.1365	-27.5161	24.07277	-278.157
23	-14.0703	-133.151	-66.9319	61.52836	-1543.93
24	1698.577	3544.374	1462.962	-419.639	-1193.95
25	0.11985	0.705785	0.323283	0.435861	-24.2083
26	-13.0397	0.049874	2.389038	-0.53312	-42.6127
27	18.9513	16.15439	3.284081	0.474821	-53.4271
28	485.4409	307.788	48.47935	264.1557	-3927.66
29	-67.5703	-241.802	-79.2974	-34.7015	-555.735
30	-135.633	-536.914	-218.963	-39.4147	-6260.25
31	14.34075	12.66548	4.748905	-8.18409	-238.465
32	-0.14409	-3.0343	-1.12735	-0.78006	-13.2235
33	11.08673	10.33655	1.852003	-2.47475	72.61649
34	142.5391	158.7801	42.54997	-85.1681	-2312.02
35	31.03443	-81.3331	-28.3711	-6.62341	-912.857
36	-412.802	-440.334	-120.086	-289.096	-241.142
37	-108.808	-54.1522	-9.53925	-39.1188	1290.452
38	120.12	252.547	102.9737	39.67869	2661.318
39	32.0453	56.2634	17.97993	30.85379	607.5422

40	1825.534	945.4077	26.69633	2222.685	-985.093
41	-1037	-1653.02	-543.285	-191.254	4380.919
42	-11.99	-123.151	-42.5558	-13.9233	6110.568
43	-1.49503	-0.38292	0.00732	-0.48612	-4.33912
44	101.7451	286.0449	115.4895	-117.401	1506.563
45	-0.27275	0.407931	0.155146	-0.26746	-14.9631
46	15.7625	-32.0647	-15.0489	3.144633	-55.5632
47	-0.26683	-1.46223	-0.51735	0.290518	16.19181
48	-27.227	-35.6049	-12.4628	1.512562	-36.9865
49	18.14222	52.09413	17.94774	-2.16669	-650.676
50	-51.5351	175.2881	38.39952	20.37056	-660.311
51	-1.86916	-15.6808	-7.46456	5.188321	167.2047
52	7.180553	4.500288	1.593348	0.44575	117.2479
53	31.91433	64.60545	20.65274	-5.83927	525.3109
54	-15.4019	-14.8964	-4.00914	-2.28108	-335.765
55	36.69831	26.84192	8.337921	2.852014	184.1147
56	-73.597	-159.053	-55.6893	-2.65664	912.7849
57	-7.61372	-4.98379	-1.19372	0.111651	-90.9199
58	18.95355	91.21082	29.8049	10.86698	-483.486
59	-54.0661	-59.557	-16.5754	-22.3487	-89.1549
60	-11.9957	-5.85748	-2.21499	-4.16681	-73.3862
61	-11.9335	-66.3467	-23.4337	-3.19321	-128.108
62	-19.9121	44.62086	16.05319	-25.8973	788.2178
63	125.4184	644.5135	258.8239	89.32673	-3382.49
64	-792.604	-855.636	-314.777	-602.606	12.19406
65	169.9448	276.4051	93.90329	-5.86725	-408.062
66	-0.02642	-1.22E-01	-4.47E-02	0.035197	1.273651
67	1.579685	2.66575	0.948187	-0.12004	-10.0382
68	5.812266	-17.8738	-7.42056	-6.76427	103.1289
69	1.278992	1.019102	0.284436	0.197692	65.97762
70	-3.75983	-2.51769	-0.67492	1.085311	-202.474
71	134.1715	-66.9452	-12.6597	182.3807	-844.273
72	0.492664	3.229711	1.255421	0.205865	-52.2118
73	0.172228	-0.02004	0.009085	-0.17123	18.1943
74	0.035346	0.008903	9.66E-05	6.65E-03	-0.81285
75	-0.33719	6.473197	2.362633	1.884306	-182.953

Values of a_{ijkl} as i=2 and k=5

l	j=1	j=2	j=3	j=4	j=5
1	-91.1466	41.88163	11.78747	-20.5501	296.962
2	284.8035	559.8033	174.4235	27.77461	2509.356
3	-35.2662	-46.5451	-13.9244	-21.1279	-56.5467
4	251.633	13.81974	8.047224	33.45825	-418.356
5	-39.8797	415.761	147.3547	123.8376	-1027.4
6	-8.30846	-49.0111	-19.6824	14.13027	-333.775
7	241.9392	320.7208	97.51562	189.3129	-922.675
8	-1232.71	-1206.79	-301.42	-1034.15	547.6515
9	-14.8628	-30.1689	-9.09392	-10.5981	38.4016
10	130.727	128.8995	28.79317	144.773	-414.835
11	118.1197	-138.785	-54.9018	-85.0006	978.9585
12	-1083.32	-1212.84	-369.514	-415.459	729.6148
13	6.303139	12.83971	4.114748	2.832261	16.41613
14	-155.854	11.10473	1.655323	-6.763	173.965
15	-152.675	-146.535	-75.978	5.00983	487.6932
16	2.324309	-10.8303	-2.87126	-5.52094	9.375278
17	-118.789	-187.326	-57.1791	-58.8807	398.4444
18	15.88279	10.64914	3.655614	0.960771	17.9773
19	0.230045	-9.81578	-3.80903	1.30357	3.741436
20	5.11285	13.37289	4.623704	1.16332	13.37416
21	9.999075	55.59926	19.16798	10.67983	50.60761
22	-28.6078	-71.9119	-21.9122	-32.2152	177.9767
23	3345.983	3650.985	1076.154	1464.251	-4390.34
24	2333.687	2841.14	843.6693	1850.879	-6707.8
25	0.561226	1.22755	0.383507	0.63272	-3.03847
26	1.64772	6.41693	1.933155	1.451509	-6.09796
27	-11.129	-7.82515	-1.31217	-10.6819	30.34675
28	-223.375	-337.296	-94.8207	-241.057	970.6622
29	-17.6198	42.06124	19.06222	28.57562	-450.596
30	244.7725	141.2181	56.36262	109.2637	-677.115
31	235.4309	269.6067	87.9781	60.46358	229.3098
32	-0.52022	-1.3495	-0.45427	-0.18777	-1.10629
33	34.77208	-4.83371	-1.43816	0.168521	-13.5241
34	-37.0751	-170.312	-48.6425	-67.8763	503.6025
35	-27.066	-15.8178	-6.46383	-3.93048	25.47744
36	-2603.06	-2263.62	-593.11	-1388.02	5429.122
37	22.57788	23.47423	5.788906	18.86089	-79.7149
38	-103.394	-79.3888	-31.7442	-48.1844	407.1825
39	-426.725	-544.587	-179.344	-106.909	-520.618

40	301.9714	-2264.17	-824.048	-525.957	3280.422
41	-35.1758	177.2715	65.60788	31.95405	-288.427
42	-43.1156	-266.997	-86.0219	-68.3958	7093.703
43	3.324733	2.820844	0.734558	2.408097	-2.25118
44	239.7981	124.9931	41.52361	114.9343	-482.606
45	-1.0672	-0.31637	-0.00307	-0.88429	-1.44381
46	-4.98189	-6.47737	-1.71768	-2.78709	-6.20757
47	10.38479	8.193655	2.163112	7.287927	-21.4178
48	-9.07087	-14.2268	-5.02933	1.285491	-29.3546
49	21.99701	96.10596	34.42229	-2.0894	-374.881
50	158.5642	-37.7395	-11.3371	2.320152	34.9147
51	-16.2151	-13.4065	-3.41505	-12.9652	46.9621
52	4.116676	0.625365	-0.11991	1.638032	42.07865
53	-90.5584	9.236947	11.40788	-135.852	200.4564
54	-42.6534	-58.3003	-18.3473	-19.981	-7.84953
55	-5.83632	-1.16029	0.473035	-9.66589	63.35701
56	-106.584	-216.474	-75.1656	-7.11467	478.298
57	-0.16466	-0.41285	-0.17687	0.165692	-3.67497
58	459.5353	543.7279	167.2488	356.273	-389.167
59	16.27025	15.68163	3.996329	15.50289	-70.7618
60	-0.64224	5.315552	2.073186	0.030435	-48.4671
61	-94.6	-146.544	-49.7567	-47.5651	-42.1576
62	-255.434	-548.177	-187.534	-36.4812	1390.153
63	421.2633	2178.774	787.2571	109.7932	-3955.02
64	-167.874	259.0884	81.18981	158.2088	-369.193
65	23.56999	-2.41084	-1.4711	0.331426	23.78449
66	-0.01968	-1.40E-02	-4.38E-03	-0.00338	-0.09453
67	0.229434	0.22634	0.072866	0.065969	-0.26047
68	-25.5316	-152.195	-52.2079	-39.0247	17.05542
69	4.850251	7.485818	2.566449	0.694149	29.40385
70	-13.8702	-12.8357	-4.98366	5.002014	-227.796
71	-132.322	-65.2568	-23.4863	-77.3621	304.1115
72	5.555799	6.997878	2.191217	2.340212	-16.8139
73	0.524578	0.24118	0.093791	-0.10203	7.221367
74	-0.36652	-0.48261	-1.58E-01	-1.12E-01	-0.09825
75	11.87842	31.0456	9.914145	15.56078	-222.427

Values of a_{ijkl} as i=2 and k=6

l	j=1	j=2	j=3	j=4	j=5
1	36.28515	-11.0843	6.109857	-14.9814	350.4956
2	-326.841	-632.017	-205.191	-132.265	3509.863
3	-21.7348	-60.8535	-21.6878	-20.1166	608.5373
4	100.3004	124.5875	22.6295	-13.2702	-1189.08
5	-76.6034	499.9122	204.6522	88.86051	2608.978
6	36.09173	30.67715	1.737552	36.0295	-1985.17
7	338.4193	912.206	300.764	217.2562	635.4033
8	468.5169	245.9778	165.1024	-1210.62	-2571.93
9	4.65077	-88.1667	-28.8615	-25.252	-695.663
10	55.39747	345.1582	101.482	342.206	-1000.16
11	146.2218	-44.0699	-38.538	81.89257	-843.956
12	-583.164	-1554.32	-524.469	-191.445	490.9358
13	3.476364	70.88302	25.65857	12.47765	182.5924
14	-68.1597	-65.0769	-7.35638	13.08597	1016.793
15	202.7619	-486.073	-162.65	-45.2706	-4280.13
16	-25.8416	-16.9042	-5.85947	-14.6129	-54.885
17	-99.3106	-569.571	-195.441	-45.8935	567.1278
18	61.36607	47.67608	14.52982	16.69075	38.40325
19	9.458142	8.816732	1.678885	5.059596	11.32516
20	9.647418	48.13281	18.70961	-3.26591	327.4737
21	41.91501	26.60384	10.34505	2.412163	30.56245
22	-31.185	-173.316	-56.8724	-31.7694	-326.552
23	357.4185	3126.526	1005.907	1296.138	-1429.67
24	973.7342	912.5732	203.4193	1315.898	-4548.2
25	5.177508	3.492883	1.164529	1.208209	6.261901
26	-10.7964	13.7258	4.496752	1.801647	189.5316
27	-19.2672	-115.55	-34.5838	-99.4346	284.8922
28	-230.892	-542.326	-177.667	-244.54	1518.413
29	-67.1271	-0.13963	8.255735	-42.6205	-268.809
30	47.73467	282.2406	85.05237	6.8467	226.0594
31	472.5557	868.3733	306.2772	-104.635	-269.726
32	-2.37271	-15.9248	-6.01166	0.80026	-51.2478
33	19.24249	16.05116	1.630684	-0.31794	-234.648
34	49.05696	367.6328	107.7478	52.31295	2113.341
35	-87.2013	-73.7476	-22.9571	3.660892	523.3445
36	665.1982	-857.695	-158.924	-2131.29	1702.446
37	66.83327	288.1529	91.37465	141.9118	-579.304
38	-0.13261	-109.676	-37.0843	18.09027	679.3265
39	-848.109	-1624.07	-577.808	244.3864	332.5435

40	926.5613	936.0841	157.2396	2111.643	-4252.72
41	-318.329	-853.144	-242.819	-644.977	880.6432
42	-4.99143	-153.938	-54.6064	30.4368	5889.415
43	2.108694	17.26342	5.602971	9.701039	-3.08509
44	264.7365	642.61	216.4063	174.2135	565.6809
45	-0.27134	-3.42128	-1.1314	-1.40123	-14.4359
46	-6.62698	-51.9003	-17.1918	-24.683	-290.128
47	-0.80778	14.02359	4.820755	3.385636	-28.4943
48	-20.6626	-18.2835	-6.62111	4.260054	37.42463
49	33.70994	40.11081	14.90981	-18.767	-552.855
50	53.86612	75.59775	9.241135	15.58304	-562.223
51	-22.6006	-105.763	-34.4184	-55.2551	58.52189
52	8.26111	10.59669	3.305904	5.839726	94.24878
53	-25.9609	-63.9554	-26.7757	-82.0618	14.76349
54	-6.21651	-31.9478	-10.872	-8.16293	-82.147
55	-4.57349	-32.3182	-9.81144	-18.489	40.93036
56	-92.6939	-130.407	-45.448	34.76539	1020.975
57	-1.55383	1.341242	0.337718	-0.45699	-22.4043
58	149.5621	403.051	146.5921	163.8135	-8.63257
59	24.39052	130.5158	42.6367	68.41628	-32.783
60	-8.80313	-4.02765	-1.1438	-6.46816	-132.663
61	-78.5364	-57.9042	-20.177	-19.4299	168.8323
62	94.57244	-109.851	-43.5663	39.47403	82.42797
63	-0.36741	626.2228	269.5954	-242.952	-1812.67
64	-533.421	391.8477	161.8612	-88.7881	5874.339
65	78.73201	86.07125	25.11338	65.12043	12.25228
66	-0.1214	-7.04E-02	-1.95E-02	-0.03788	0.416545
67	1.398844	1.888147	0.642888	0.330816	-3.97112
68	9.054928	2.552595	-2.44523	-12.2585	-536.036
69	0.701729	1.064579	0.375203	-0.30818	21.09021
70	-4.39627	-12.0002	-3.85191	4.053924	-33.7857
71	-41.8677	-330.602	-117.196	-58.089	-1322.13
72	4.172794	7.66277	2.543442	1.570501	-15.7311
73	0.452525	0.384319	0.119053	-0.14586	0.599946
74	-0.12974	-0.22271	-7.35E-02	-2.25E-02	0.404764
75	-2.62347	2.160051	1.329271	5.015072	-4.49507

Values of a_{ijkl} as i=3 and k=1

l	j=1	j=2	j=3	j=4	j=5
1	218.25	303.0773	100.8584	44.64509	-257.231
2	-52.7917	76.23853	41.58524	-195.105	4807.331
3	24.74669	-53.7252	-19.5373	21.53868	-514.531
4	157.1421	168.951	53.78774	10.745	-437.368
5	-258.509	988.3755	222.3491	340.6676	4211.01
6	-11.6952	-40.1156	-15.1724	5.966876	-309.36
7	325.9142	362.6444	122.4495	104.8477	-2894.02
8	972.8215	1536.197	548.3815	165.0483	-7905.96
9	-57.4249	-38.7372	-14.5182	-12.5222	518.9638
10	-217.902	-334.617	-103.682	32.90281	-4.1395
11	810.1781	159.2567	108.1827	83.06012	-3795.76
12	-289.647	-337.663	-119.673	-5.87794	-348.792
13	4.705723	19.94366	7.051665	-1.09941	0.08499
14	-40.8544	-58.6096	-14.5421	7.416047	81.50176
15	381.4816	289.031	280.0819	39.89343	-716.832
16	-24.0076	-34.2148	-12.4512	11.29469	116.4543
17	18.26424	-57.5105	-16.7658	-68.7145	86.82515
18	93.49547	116.4338	27.82037	-0.97056	115.7929
19	6.7933	4.533286	1.496067	2.408662	26.30263
20	1.506191	4.970431	1.918416	-1.5083	12.58271
21	49.05149	90.33387	32.20277	-53.6527	-95.0838
22	-34.0492	-34.3369	-10.5278	-20.4288	589.1172
23	365.8818	484.5593	133.3077	310.7154	6412.88
24	5650.786	7976.689	2450.826	2770.212	-9239.86
25	5.010016	4.357545	1.61489	0.02436	-8.92705
26	5.545759	1.655262	1.016114	0.932718	-146.809
27	13.06435	28.37006	10.37044	-1.76072	13.01389
28	-1183.81	-2701.89	-825.239	-622.686	2408.378
29	-264.919	-139.318	-54.3873	-0.93466	1082.549
30	-426.299	-267.387	-343.61	244.576	641.9583
31	91.36751	103.0262	36.93386	13.22653	51.25779
32	-0.87235	-2.1659	-0.77922	0.102254	1.031283
33	5.89014	10.07159	1.513826	-1.42623	33.33969
34	968.5847	408.2492	-14.5917	601.5585	-3525.97
35	-70.0672	-69.1346	-23.5673	6.928884	-134.914
36	-487.788	-16.9571	41.27175	-269.905	-806.774
37	61.35597	133.1443	40.02091	47.58405	-187.617
38	163.9864	29.61264	49.78934	25.07638	763.3233
39	-244.258	-331.757	-109.484	-71.3327	-1695.09

40	-2792.14	-15007.4	-5501.57	-546.539	7351.822
41	-512.153	1490.532	703.2819	-856.083	1895.392
42	46.44546	-99.9174	-26.5766	-34.7222	16740.18
43	-5.94149	-6.10779	-1.99735	-0.4911	11.44316
44	159.5854	197.7668	62.88335	75.83098	-1065.3
45	-6.55135	-7.39812	-2.5238	0.670159	1.531972
46	-12.5732	-8.22696	-1.91221	-7.97109	152.482
47	9.307288	21.62614	7.66782	-4.6756	-21.2326
48	-83.5276	-149.96	-47.0233	-18.9187	-23.0421
49	-5.73604	177.3101	73.68531	-11.9793	-884.989
50	506.8943	253.7736	125.2569	-23.1978	-1721.33
51	-10.6879	-22.2321	-8.06437	-14.7783	89.08929
52	29.10243	44.13888	12.37613	0.409488	100.4808
53	5.276971	119.8441	35.42992	-60.1607	140.5748
54	-31.1857	-12.0125	-8.03705	47.7766	-779.764
55	-171.755	-330.82	-115.765	-43.3838	723.8636
56	-578.637	-1417.78	-448.054	-436.812	663.0574
57	-16.0151	-19.7719	-5.07542	-6.02225	-38.6085
58	559.7436	1075.801	417.0869	-143.799	-2173.97
59	137.4734	295.6694	99.62044	42.34005	-519.191
60	12.16209	25.52999	17.51545	-29.471	-150.22
61	-177.358	-305.6	-110.227	111.6169	712.2724
62	-295.539	-526.03	-126.917	-804.77	-1789.07
63	1734.776	7305.717	2466.937	2175.105	-6183.53
64	-968.297	-59.8161	183.9409	-468.886	476.9404
65	301.5485	380.13	24.11426	252.5157	114.4765
66	0.173485	1.52E-01	5.16E-02	-0.03936	-0.02789
67	2.081299	3.562093	1.153899	0.950925	-3.73232
68	-26.1457	-188.985	-70.2823	-27.4967	217.5876
69	-4.78284	-10.0167	-3.90586	-2.90155	227.4633
70	-6.2671	-20.4069	-6.79231	12.12949	-400.748
71	-214.503	-322.054	-118.819	-68.298	38.3429
72	74.0594	151.1852	47.48064	41.74895	-134.014
73	6.778128	12.6607	3.545759	2.229545	26.11342
74	-0.78719	-2.50379	-0.72442	-4.91E-01	-3.8614
75	-0.10831	16.0464	5.155077	1.361957	-471.929

Values of a_{ijkl} as i=3 and k=2

l	j=1	j=2	j=3	j=4	j=5
1	286.2932	530.445	166.6531	38.51684	430.5148
2	-1096.07	-51.3552	-112.949	20.00701	2400.809
3	148.1235	119.1137	55.65609	3.475428	1782.218
4	126.7489	-162.853	-24.5327	-38.4976	-2217.11
5	563.4732	-760.083	-209.409	-383.381	17701.37
6	-32.9997	-84.4536	-29.3839	10.3092	-2700.43
7	872.9705	182.1376	140.4726	-62.781	1907.648
8	1076.406	1697.956	502.3687	38.77606	-10842.7
9	-25.0257	-121.562	-51.9473	13.13538	-1134.61
10	158.0291	-382.09	-72.0672	-186.629	-1140.91
11	95.15232	2280.69	738.9587	551.0778	-13295.7
12	118.0992	24.78266	4.813531	15.69072	-799.848
13	-83.237	17.00532	4.315526	-4.73321	67.8578
14	-32.7444	206.9363	45.79321	33.41202	1331.75
15	578.1324	3544.186	1574.51	1637.818	-1400
16	-62.441	-38.084	-15.8054	19.28002	341.4637
17	23.363	-403.695	-134.847	-42.0147	827.914
18	54.43178	202.5611	64.66949	8.499899	-988.185
19	-13.1947	-11.8362	-3.03765	-4.04236	68.10479
20	26.58493	34.26436	12.084	-3.85028	460.674
21	10.0323	-18.3122	-2.36608	-11.5988	-99.1029
22	-174.287	11.54189	-16.5516	6.630192	-599.924
23	-477.099	-105.646	-7.2245	106.1284	9192.042
24	4863.979	9314.153	3834.548	-2514.62	-32643.4
25	34.8361	21.52625	7.896838	-6.4107	-20.3515
26	-21.7215	6.003039	4.848872	-0.29819	189.0376
27	-38.0727	42.39394	7.449276	10.82593	1186.452
28	-554.226	-1684.74	-951.578	3794.181	20268.39
29	46.73216	-601.377	-186.737	-107.704	3651.903
30	462.5063	-1379.44	-758.032	-177	-10832.3
31	-13.9408	19.50795	6.042342	-2.79795	275.4519
32	8.140945	-11.3164	-3.57508	2.392327	-1.89721
33	10.23277	-52.3222	-11.4062	-7.76795	-251.286
34	-987.476	-3173.5	-1570.49	827.5935	-13709.9
35	-67.1169	-8.92526	-7.92017	2.13245	-69.8971
36	-949.985	-1820.27	-676.989	-98.1465	12357.9
37	26.69159	528.2737	214.6947	-256.388	-9733.77
38	-70.6701	681.9571	243.9935	233.4099	4657.402
39	138.2029	104.3515	29.76793	1.545415	-3422.05

40	5534.531	13420.59	3364.378	12549.57	-65977.1
41	-3358.19	-15426.7	-4737.73	-8793.6	74128.22
42	99.2132	25.10454	11.58001	-6.94231	15073.93
43	-23.2649	-22.0955	-7.81569	2.537928	41.41763
44	356.2758	19.91573	48.87001	-16.9867	1721.812
45	-7.12592	-6.2502	-2.16698	1.367712	8.137522
46	19.92511	-43.5182	-20.6078	-1.36509	-1037.8
47	3.224682	5.61836	2.124147	-2.34383	-35.5899
48	-24.1405	-124.173	-37.349	10.56467	-365.636
49	35.72	97.6085	35.02665	-8.81151	-95.188
50	140.5902	822.868	245.612	147.6605	-7727.26
51	-141.847	-123.696	-50.6239	57.3245	792.1327
52	1.842556	21.78025	5.101034	2.242917	212.1518
53	-23.5553	-15.8232	-7.28413	-0.45541	159.6351
54	-80.1913	-53.757	-16.2864	-47.5209	-1258.5
55	18.46678	-119.392	-74.0626	95.95609	3240.848
56	-212.253	-574.355	-175.115	-146.327	-669.603
57	-16.7663	-91.6087	-32.4802	-10.5229	-102.075
58	282.845	411.7926	169.6225	-6.18184	-690.788
59	-167.391	-189.303	-21.8162	-734.79	-5838.68
60	-48.7222	-56.4492	-7.98184	-27.1197	256.9391
61	-70.7638	-55.2691	-20.0099	17.87759	165.4736
62	-120.616	-647.297	-228.165	-90.2809	-1076.18
63	528.9031	2950.016	1085.019	100.953	9779.486
64	-1126.46	-3582.4	-1227.99	-1152.45	5978.749
65	352.9063	1937.142	586.8217	179.6073	-3175.87
66	0.666407	3.86E-01	1.47E-01	-0.15989	-1.17498
67	8.692291	16.15565	5.556477	-2.5561	-22.2991
68	-10.3747	-39.0423	-16.9355	2.876602	-397.034
69	2.407267	-1.49894	-0.83288	5.963574	184.6632
70	-2.06546	-0.25498	-0.11417	0.833093	-238.306
71	-104.323	134.1542	47.79632	107.0194	-465.648
72	14.68279	43.15271	15.78948	-0.83418	-364.777
73	-5.83938	0.269501	-0.04666	0.055402	51.76334
74	0.564276	0.146343	0.040339	-1.83E-01	-4.41737
75	-4.41408	-1.87758	-0.65838	0.136536	-315.53

Values of a_{ijkl} as i=3 and k=3

l	j=1	j=2	j=3	j=4	j=5
1	256.6162	463.2325	153.9968	105.0543	-792.788
2	40.588	1556.698	558.4326	151.5778	-2318.11
3	-12.0307	-124.496	-41.6259	-24.7641	41.09128
4	46.91667	-140.17	-53.6138	-3.63083	347.8436
5	160.1489	157.2549	41.93267	-8.07298	-65.2596
6	-80.1329	-138.049	-45.2889	-23.2822	-166.455
7	686.5398	-211.274	-113.608	126.0022	1127.582
8	3159.19	6452.573	2141.889	1789.243	-13157.4
9	-39.8301	35.43012	13.85889	-1.50465	77.06305
10	-295.762	-757.134	-253.819	-132.88	1021.815
11	-223.312	-534.902	-165.838	-16.9638	789.6319
12	-1356.86	-1663.5	-539.304	-420.462	2411.829
13	14.49986	28.8837	9.2965	5.995358	-34.0445
14	-36.0218	17.66327	10.39495	3.060883	-245.563
15	-161.846	333.0862	125.823	270.269	-349.917
16	-21.9587	-35.9949	-11.336	-15.8847	133.8275
17	-181.222	-229.958	-75.5267	-83.1707	774.0592
18	49.81008	61.70283	20.39771	6.122823	-18.5547
19	1.956655	16.45078	5.913173	3.358711	-36.4352
20	13.53996	20.26123	6.562035	5.591674	-13.2129
21	177.2531	285.0325	90.18969	73.11291	-453.615
22	-156.441	-8.69675	9.078679	-24.0134	-228.78
23	1730.113	-77.4598	-55.6933	92.88388	1702.783
24	-4358.34	-11220.1	-3731.33	-2420.77	16997.63
25	-0.8409	-5.10038	-1.69752	-0.01347	5.466827
26	14.26024	8.166181	1.967289	2.177501	-52.7728
27	19.97171	51.86126	17.38864	9.807774	-78.9398
28	220.5381	899.7828	306.5778	109.7223	-892.564
29	-28.5631	27.31454	5.889659	-24.0466	-125.609
30	373.5908	637.8955	201.8087	-175.899	-1092.38
31	523.128	790.9577	259.1567	182.6661	-1124.35
32	-1.35594	-2.45525	-0.79265	-0.63997	3.341018
33	6.356264	-5.77723	-2.7278	-0.96403	83.34026
34	11.84376	367.6545	130.8268	10.1418	-629.432
35	-53.2112	-18.266	-5.39539	-13.147	-101.337
36	1781.926	5607.152	1855.722	1247.332	-10048
37	-15.7295	-57.9026	-19.5308	-5.51657	51.48461
38	-30.5154	-164.61	-52.266	36.71561	544.5323
39	-1130.52	-1684.67	-550.079	-383.615	2201.229

40	-2081.12	-2783.77	-779.702	-1387.7	9332.187
41	179.4047	289.1881	83.44323	159.3816	-1022.19
42	-462.408	-804.27	-210.638	-447.5	18460.9
43	-4.08277	-8.48174	-2.82256	-1.81588	13.76694
44	472.6321	-233.508	-101.522	-10.9267	1605.582
45	-5.74185	-11.057	-3.6444	-1.75632	10.73372
46	-23.8553	4.935572	2.337915	3.775559	11.45841
47	40.21388	136.1523	45.646	22.8069	-188.615
48	-65.3521	-90.8318	-28.9604	-21.7801	146.7051
49	224.5951	79.67034	18.16736	117.335	-830.061
50	42.45943	1.173628	-0.60373	17.72925	-210.385
51	32.79662	88.96359	29.55171	13.82795	-111.422
52	21.43217	26.20236	8.200424	0.590246	-2.31389
53	504.1079	1150.751	367.0016	35.27511	-788.868
54	72.81179	216.638	72.83541	64.30192	-489.354
55	70.38893	119.2864	38.65117	15.4145	-114.365
56	-723.932	-1327.78	-434.945	-376.257	2798.873
57	-3.07067	-3.61755	-1.13587	0.061252	-0.49707
58	480.1145	755.9097	245.9201	632.6732	-3204.59
59	-46.6701	-134.424	-44.8298	-20.6138	159.5645
60	-23.7092	-21.0463	-6.49282	3.161974	-16.4231
61	-468.341	-715.592	-228.177	-207.152	1280.498
62	-7.0401	2064.879	693.1952	327.951	-3263.16
63	4847.55	2454.355	628.9487	1655.126	-6627.98
64	981.6209	1254.897	369.4115	482.3844	-2764.54
65	25.7293	-66.3244	-20.4973	-54.0011	343.1691
66	0.140875	3.16E-01	1.05E-01	0.044203	-0.29932
67	0.328846	-0.15598	-0.06344	0.193872	-1.04648
68	-38.827	2306.071	808.3894	237.9857	-3354.55
69	-35.2111	-86.7885	-29.033	-29.7097	244.9435
70	-176.619	-631.175	-211.652	-78.9218	258.9839
71	-417.888	-14.5196	8.410208	-45.8855	-532.362
72	11.36503	19.19053	6.317366	6.655038	-52.5853
73	1.015014	3.738867	1.230175	-0.2038	2.230453
74	0.71663	0.852648	0.286055	4.94E-01	-2.93284
75	-4.50904	-42.7491	-18.5414	-7.25421	-403.836

Values of a_{ijkl} as i=3 and k=4

l	j=1	j=2	j=3	j=4	j=5
1	130.7408	205.6688	63.60501	59.10683	-146.279
2	66.20939	-2710.64	-726.578	-184.023	-205.462
3	-334.606	0.094728	-4.50159	25.40892	-400.713
4	411.3077	440.7219	145.651	-15.4511	-509.598
5	-968.971	705.7318	194.8802	221.5443	4357.873
6	-93.6842	-183.254	-49.9811	-47.7512	-1319.12
7	68.25424	2431.622	692.7048	228.1446	1044.361
8	22.11455	-21.9955	4.802865	-1261.11	3431.496
9	238.9509	-195.852	-63.3681	-41.5888	439.1533
10	-60.9416	665.8487	250.0875	306.8986	-3566.5
11	1668.64	291.809	112.0324	204.404	-3644.6
12	-506.417	-658.156	-227.801	68.66266	-579.849
13	31.5657	101.3058	30.84944	12.42782	88.46077
14	-283.002	-237.014	-76.5199	19.53904	259.758
15	14.80728	1190.025	364.0817	2.139081	-4043.15
16	-42.0052	-105.231	-37.8452	-12.3235	582.4437
17	216.451	326.0933	98.74309	58.24749	665.8342
18	267.0724	209.4846	63.64586	11.66653	-68.041
19	-17.3585	-49.6963	-15.2023	-18.2489	340.1619
20	20.03036	43.62907	12.85593	11.60541	50.66537
21	113.5176	278.5556	91.1526	3.873903	51.41966
22	73.74016	-497.612	-134.32	-48.7299	-474.39
23	-350.187	-3495.57	-1233.44	-684.2	11760.67
24	8538.205	19404.93	6709.648	7276.09	-47548.1
25	-1.20005	7.645839	3.75494	-0.06933	-40.103
26	-67.4858	47.73283	14.66451	10.73952	-118.914
27	-45.1514	-156.31	-54.9973	-45.2784	697.1597
28	-1541.39	-5713.48	-2070.44	-872.945	15372.62
29	-551.956	-95.1426	-41.2275	-39.4908	702.9475
30	-101.375	-455.827	-108.667	170.8926	-2420.56
31	451.6526	967.9085	332.23	126.6862	-2329.18
32	-4.63515	-17.0692	-5.38209	-1.90101	-12.0364
33	70.74892	45.94641	14.60151	-5.55172	-46.0811
34	874.3758	2351.03	807.4652	-292.357	-1790.49
35	-179.004	-278.208	-93.7908	31.59733	-1218.85
36	1920.05	10629.73	3762.606	723.0519	-31428.4
37	237.4797	993.3464	362.9107	82.88244	-1939.54
38	147.1831	-223.414	-88.2813	-12.5797	2453.098
39	-1130.85	-2600.35	-891.436	-305.154	6605.413

40	-5022.37	-32473.6	-11592.6	-3727.34	66710.11
41	-2589.65	-1616.35	-286.332	-1048.43	-969.542
42	-69.2442	-250.178	-60.299	-156.986	14949.86
43	-6.10694	-1.42754	-0.22542	2.451425	-3.09714
44	450.4199	2006.876	563.0474	152.2295	2085.156
45	-5.36113	-6.44843	-1.94848	0.704313	4.296171
46	89.99407	-125.706	-34.9101	-30.2172	73.30468
47	11.68051	22.80749	7.154055	-1.53576	-81.7947
48	-127.295	-167.816	-53.4945	-24.2827	-15.667
49	45.42026	261.9329	86.61698	30.92975	-1197.99
50	775.594	339.3305	151.6973	48.17912	-1550.85
51	-6.17965	-75.7551	-35.4452	-35.5025	417.9945
52	53.3391	51.12946	14.93157	7.461431	105.4645
53	135.4208	177.0778	58.73625	26.63667	730.716
54	-97.0185	-134.185	-34.7548	-25.0411	-65.1891
55	64.67963	-143.662	-58.4397	24.85274	811.476
56	-345.333	-957.277	-330.641	-68.0853	2259.944
57	-58.2471	-75.1912	-19.5828	-10.5515	-20.396
58	444.2433	1342.957	431.7463	91.70507	-3107.85
59	-39.9455	276.4444	115.3702	3.674087	-993.597
60	-17.2859	64.79581	22.2395	-18.4211	-244.396
61	-192.564	-415.903	-138.068	-25.7601	412.1888
62	81.00381	296.3504	113.0416	-114.615	1432.34
63	407.993	2697.591	945.9167	963.085	-8239.23
64	864.2456	4410.033	1344.741	-579.207	3807.267
65	682.6015	171.1483	-19.2605	218.705	-2051.89
66	0.143234	-1.36E-02	-2.13E-02	-0.12074	0.282264
67	5.484153	9.584523	3.280085	1.691773	-16.8224
68	48.65529	-2.65015	0.947305	-38.1792	-82.0862
69	7.301707	8.622702	2.158534	2.388438	64.66247
70	-26.733	-45.9368	-15.461	1.840558	-221.301
71	-866.125	-1897.95	-547.732	3.247849	-1632.67
72	7.03555	35.14847	13.27183	0.336557	-120.377
73	4.800761	7.042649	2.166646	0.457988	14.24306
74	-0.23531	-0.97686	-0.32533	-4.71E-02	1.227495
75	-4.52768	6.968797	2.301609	6.908468	-265.907

Values of a_{ijkl} as i=3 and k=5

l	j=1	j=2	j=3	j=4	j=5
1	222.2768	435.0211	141.369	52.96851	-725.973
2	-562.126	-207.655	-102.547	-302.499	-257.684
3	99.26563	174.9375	67.34943	68.2906	-82.9429
4	74.24806	-38.4995	-13.6539	55.24309	606.305
5	983.6725	630.2193	157.5492	246.9502	-3884.84
6	-134.663	-334.714	-109.458	-81.8393	-625.058
7	1011.209	19.11491	-2.00874	258.5951	2433.061
8	4627.735	14771.48	5032.474	2502.027	-21007
9	-161.492	-63.0284	-19.158	-68.9178	-233.465
10	-574.308	-2511.5	-865.996	-330.239	3547.615
11	-671.347	-637.097	-167.2	-16.1695	1835.998
12	-1301.97	-859.375	-264.989	-201.383	196.1417
13	34.2489	26.91994	6.666177	8.024872	104.4562
14	34.4743	63.42538	18.79425	-6.93846	-493.802
15	-739.438	129.6537	84.46612	-1.96844	682.204
16	-61.7705	-12.9491	-1.32604	2.582131	-12.1765
17	-645.617	-415.793	-117.792	-151.44	964.5782
18	176.0915	120.3016	35.89223	51.80738	-231.218
19	-23.9011	-48.6671	-15.4928	-18.162	67.81376
20	81.5539	103.5859	32.3894	32.16815	-10.7137
21	207.6758	303.4923	95.94376	93.58941	-284.774
22	-169.184	-18.3399	-4.74014	-44.4383	-597.553
23	121.0953	-5221.61	-1754.22	-1188.11	13144.36
24	-1200.41	-17308.2	-6187.43	239.172	3149.372
25	12.06069	10.97797	3.404984	6.193232	-34.7874
26	25.93312	15.16445	4.675156	11.73185	87.71116
27	68.01041	370.569	126.5323	65.24156	-642.982
28	-165.987	2191.5	815.1445	-246.974	-696.168
29	68.98291	152.4831	42.24417	18.9078	-863.917
30	581.8633	-36.22	-56.1098	-205.039	1668.774
31	758.0643	1309.604	425.5961	298.0612	-2130.73
32	-12.4646	-19.3162	-6.04352	-5.69948	14.03742
33	-15.7511	-29.1551	-8.68955	-2.84312	151.3445
34	714.9871	288.6299	93.42444	100.5071	-1634.28
35	-186.719	-289.574	-96.684	-137.67	590.8913
36	4274.919	13895.94	4566.899	3128.981	-27110.5
37	40.27203	-369.258	-130.253	-25.7594	553.2382
38	-132.209	-60.9142	-9.7331	-32.8219	504.784
39	-1443.33	-2665.97	-865.652	-586.308	4127.735

40	-4526.53	-5998.95	-1499.42	-4742.16	31475.19
41	40.27587	1237.169	368.6553	660.2086	-4442.41
42	-257.905	-146.113	21.29111	-379.18	16060.68
43	-2.72555	-37.204	-12.8407	-4.23784	57.18577
44	643.9719	-227.266	-81.3855	99.8151	3081.279
45	-5.11902	6.813714	2.50181	0.283883	-15.5675
46	-50.3249	40.94519	13.34099	-4.80323	-342.22
47	4.857448	-32.513	-11.1429	1.755152	5.015922
48	-49.564	-96.5439	-31.4462	-13.4294	70.66957
49	84.38457	372.84	123.4843	80.30981	-1222.15
50	-149.536	-267.165	-81.0533	-21.0031	1689.716
51	-1.06876	202.8083	70.32979	11.18133	-214.903
52	32.36853	-5.70646	-2.94775	-6.06	135.2429
53	180.8686	754.1269	235.7179	33.4874	-615.633
54	-44.9939	-8.24177	-2.33531	-12.725	21.34565
55	-1.01374	71.33082	23.9819	-11.777	30.57447
56	-320.629	-795.555	-261.082	-187.477	2117.294
57	0.777537	0.10838	-0.20943	0.957544	-13.4495
58	523.5839	-119.756	-41.0826	401.8076	-644.764
59	6.456549	-249.583	-86.4984	-7.28357	218.9559
60	-24.5837	18.93035	7.331877	15.85494	-199.476
61	-388.002	-456.222	-143.271	-177.485	640.674
62	-294.505	-214.65	-64.786	-95.7588	1246.708
63	2587.941	6884.874	2186.827	2004.276	-15571.1
64	399.9112	-72.3881	-85.3204	-133.336	6651.123
65	226.846	-61.4829	-27.5459	-7.75553	37.54057
66	-0.09914	-1.72E-01	-5.73E-02	-0.01081	-0.26582
67	1.380651	1.600583	0.51189	0.528714	-2.23224
68	-153.7	-303.644	-92.7819	-110.034	206.378
69	8.271952	14.71245	4.851862	2.797616	2.249926
70	-24.0828	-48.5725	-16.5708	-5.64739	-192.329
71	-471.073	100.1316	53.70238	-31.343	-2739.83
72	12.99458	12.38207	3.873968	5.704016	-39.0264
73	2.195322	3.148127	1.040078	0.470717	3.669553
74	-0.71306	-0.97	-0.31401	-3.06E-01	1.810905
75	35.16493	16.62524	2.232005	26.64922	-321.656

Values of a_{ijkl} as i=3 and k=6

l	j=1	j=2	j=3	j=4	j=5
1	295.0208	415.5822	153.7631	-35.0702	57.08297
2	-1306.78	-3012.67	-949.566	-985.844	4264.388
3	78.60355	351.1901	109.0579	118.08	44.40504
4	-73.0342	174.1173	17.4897	38.1489	-2014.76
5	1980.111	1724.671	608.9249	1193.795	4865.141
6	98.57575	266.2051	81.4566	-48.7209	-1775.63
7	1143.218	1904.234	579.224	1086.326	-595.38
8	2828.139	9766.869	3263.693	-2728.91	-3252.62
9	-59.3734	-332.717	-96.4245	-225.883	479.4748
10	-728.979	-1637.1	-534.088	713.3469	-2923.05
11	-503.958	-461.702	-175.806	-248.69	-3222.77
12	-1305.99	-1465.16	-442.849	-332.835	-489.329
13	21.35793	43.68381	10.71445	43.65318	-218.261
14	92.26312	-89.5178	-2.39518	22.46928	1432.387
15	-1640.6	-1704.4	-504.138	-1120.21	-1014.35
16	12.61647	3.503251	3.209872	-7.09768	-143.546
17	-1112.64	-1976.21	-621.118	-334.408	3970.29
18	498.8135	465.124	136.8629	247.8655	-768.224
19	97.58753	180.246	55.99548	27.51191	279.2139
20	41.08898	42.13288	13.84037	39.49591	-90.2194
21	164.0418	331.5845	106.0416	80.06464	-0.03726
22	-190.336	-421.782	-127.659	-209.51	147.9391
23	1707.704	-1823.97	-757.231	315.0778	13947.3
24	4818.974	3403.083	1193.739	11621.25	-57628.3
25	-5.94013	7.887949	2.28265	6.617147	85.3186
26	-13.1347	76.32933	22.34438	36.27484	-194.528
27	123.7578	595.7824	212.7256	-52.1595	128.3416
28	-1475.36	-3881.25	-1331.33	-3176.25	18456.76
29	-66.9374	57.34469	28.20476	9.97124	420.5312
30	300.2521	7.842626	-87.0063	345.3163	-410.998
31	307.8706	768.248	256.4051	77.97361	-2254.19
32	-12.1391	-39.7182	-12.7649	-12.4205	82.23912
33	-19.6625	10.15445	-3.30709	-6.55172	-299.853
34	592.0423	374.0739	102.078	42.6731	-1005.14
35	-454.158	-733.63	-239.147	-202.373	580.6569
36	-561.654	7586.542	2711.451	-93.9156	-30180.1
37	358.8378	128.1079	5.047393	300.4977	-1244.65
38	32.09708	-106.23	-10.9795	-135.471	1345.774
39	-451.475	-1584.06	-531.972	-99.6537	4569.922

40	-2423.57	-20382.5	-7105.68	-9780.91	86098.04
41	-857.844	5591.722	2102.573	1270.88	-17272.2
42	-241.679	-408.238	-83.6309	-331.802	15412.99
43	10.92104	-28.2924	-10.7549	24.50628	59.58249
44	1057.313	1431.399	427.8497	917.0895	239.8886
45	-19.6998	-20.1616	-5.95269	-7.24964	53.07756
46	-84.7091	-143.79	-40.5836	-133.814	24.84329
47	51.54035	60.40987	18.26097	23.84253	-231.963
48	-48.3508	-118.208	-39.8931	-2.26656	101.6701
49	-95.9905	139.5608	51.28153	-47.7094	-1017.54
50	-237.323	-9.69843	-40.2454	-23.192	-2080.49
51	-162.796	50.17782	24.9674	-177.67	-167.851
52	49.30644	19.69908	4.383268	12.89847	80.95124
53	153.5906	494.9164	158.2765	-60.7918	-235.317
54	-69.1633	-72.5459	-20.6584	-28.9212	56.81897
55	-34.3586	49.48454	20.82711	-58.895	36.02258
56	-3.68746	-468.673	-162.115	49.08297	2346.056
57	-12.7924	-16.0525	-4.93887	1.468222	-13.1458
58	371.643	236.0849	67.57551	461.3836	-1374.02
59	277.8733	38.7194	-0.04995	250.6502	190.345
60	-19.5701	43.97451	15.97693	1.934103	-227.625
61	-188.855	-296.257	-96.1745	-117.085	315.2062
62	2.513111	43.84181	14.4557	64.84794	1962.695
63	1006.217	4854.465	1629.612	1037.728	-11590.4
64	-65.5563	1473.823	385.2499	587.3212	3281.789
65	846.2421	298.7504	60.23684	486.2506	-1087.7
66	1.130004	2.06E+00	6.59E-01	0.176271	-5.92821
67	1.808594	2.012121	0.667238	1.601805	-1.04017
68	31.07702	24.9518	8.490489	-62.7042	-656.015
69	0.591916	2.071061	0.714534	-1.08235	28.26171
70	-34.7246	-70.2912	-23.4174	0.7341	8.326148
71	-688.422	-985.397	-276.944	-608.247	-417.991
72	6.820427	5.290224	1.399855	5.458983	-41.8803
73	2.413397	4.132303	1.352063	0.215362	0.141965
74	-0.01003	0.024617	0.014275	-5.53E-02	1.028359
75	2.626346	-28.088	-10.7327	25.86615	-121.259

Appendix C

The input properties of 100 test samples

sample #	E_f (GPa)	σ_f (MPa)	E_s (GPa)	σ_{fL}/σ_{fT}	n
1	125	300	75	1.15	0.05
2	125	300	175	1.15	0.05
3	125	300	75	1.35	0.05
4	125	300	175	1.35	0.05
5	125	300	75	1.15	0.25
6	125	300	175	1.15	0.25
7	125	300	75	1.35	0.25
8	125	300	175	1.35	0.25
9	125	300	75	1.15	0.35
10	125	300	175	1.15	0.35
11	125	300	75	1.35	0.35
12	125	300	175	1.35	0.35
13	125	300	75	1.15	0.45
14	125	300	175	1.15	0.45
15	125	300	75	1.35	0.45
16	125	300	175	1.35	0.45
17	225	300	75	1.15	0.05
18	225	300	175	1.15	0.05
19	225	300	75	1.35	0.05
20	225	300	175	1.35	0.05
21	225	300	75	1.15	0.25
22	225	300	175	1.15	0.25
23	225	300	75	1.35	0.25
24	225	300	175	1.35	0.25
25	225	300	75	1.15	0.35
26	225	300	175	1.15	0.35
27	225	300	75	1.35	0.35
28	225	300	175	1.35	0.35
29	225	300	75	1.15	0.45
30	225	300	175	1.15	0.45
31	225	300	75	1.35	0.45
32	225	300	175	1.35	0.45
33	125	700	75	1.15	0.05
34	125	700	175	1.35	0.05

35	125	700	75	1.15	0.25
36	125	700	175	1.15	0.25
37	125	700	75	1.35	0.25
38	125	700	175	1.35	0.25
39	125	700	75	1.15	0.35
40	125	700	175	1.15	0.35
41	125	700	75	1.35	0.35
42	125	700	175	1.35	0.35
43	125	700	75	1.15	0.45
44	125	700	175	1.15	0.45
45	125	700	75	1.35	0.45
46	125	700	175	1.35	0.45
47	225	700	175	1.35	0.05
48	225	700	75	1.15	0.25
49	225	700	175	1.15	0.25
50	225	700	75	1.35	0.25
51	225	700	175	1.35	0.25
52	225	700	75	1.15	0.35
53	225	700	175	1.15	0.35
54	225	700	75	1.35	0.35
55	225	700	175	1.35	0.35
56	225	700	75	1.15	0.45
57	225	700	175	1.15	0.45
58	225	700	75	1.35	0.45
59	225	700	175	1.35	0.45
60	100	200	100	1	0.45
61	50	200	50	1	0.35
62	125	500	125	1.25	0.25
63	100	600	100	1.1	0.35
64	100	600	100	1.1	0.45
65	150	400	150	1.2	0.35
66	150	400	150	1.2	0.45
67	200	1000	200	1.3	0.35
68	200	1000	200	1.3	0.45
69	250	800	250	1.4	0.35
70	250	800	250	1.4	0.45
71	50	200	150	1.3	0.2
72	100	200	100	1	0.3
73	150	200	50	1.2	0
74	150	200	200	1.1	0.1
75	200	200	200	1.4	0.5
76	250	200	250	1.5	0.4

77	50	400	50	1.2	0.4
78	100	400	100	1	0.5
79	150	400	150	1.1	0.1
80	150	400	200	1.3	0
81	200	400	200	1.4	0.2
82	250	400	250	1.5	0.3
83	50	600	200	1.1	0.3
84	100	600	250	1.4	0
85	150	600	100	1	0.5
86	150	600	50	1.3	0.1
87	200	600	150	1.2	0.2
88	250	600	150	1.5	0.4
89	50	800	200	1.3	0.1
90	100	800	50	1	0.3
91	150	800	100	1.1	0
92	150	800	250	1.4	0.2
93	200	800	150	1.2	0.5
94	250	800	200	1.5	0.4
95	50	1000	200	1.3	0.1
96	100	1000	50	1	0.3
97	150	1000	100	1.1	0.2
98	150	1000	150	1.2	0
99	200	1000	250	1.5	0.4
100	250	1000	200	1.4	0.5

Appendix D

The output properties of all 100 test samples through the reverse analysis

sample #	E_f (GPa)	σ_f (MPa)	E_s (GPa)	σ_{fL}/σ_{fT}	n
1	122	310	75	1.06	0.05
2	126	298	175	1.03	0.06
3	121	308	75	1.14	0.06
4	125	309	175	1.21	0.05
5	130	314	74	0.94	0.25
6	129	288	174	1.10	0.26
7	123	305	75	1.30	0.25
8	127	299	174	1.42	0.25
9	129	269	74	1.37	0.35
10	124	313	175	1.05	0.35
11	122	312	75	1.46	0.34
12	126	303	175	1.32	0.35
13	125	294	75	1.28	0.44
14	127	288	175	1.07	0.46
15	125	312	75	1.38	0.44
16	125	290	175	1.26	0.46
17	222	302	75	1.09	0.05
18	230	292	175	1.26	0.05
19	241	301	75	1.45	0.04
20	233	280	175	1.50	0.06
21	212	311	76	1.25	0.25
22	224	289	175	1.30	0.25
23	218	328	75	1.28	0.25
24	226	296	175	1.45	0.25
25	222	338	75	1.33	0.32
26	223	306	175	1.16	0.35
27	230	286	75	1.79	0.33
28	223	306	176	1.26	0.35
29	223	305	75	1.05	0.46
30	225	300	175	1.26	0.44
31	230	296	75	1.20	0.46
32	223	315	175	1.41	0.44
33	108	712	76	1.68	0.01
34	130	691	174	1.14	0.07

35	121	722	75	1.25	0.24
36	122	734	176	1.10	0.24
37	128	663	75	1.58	0.24
38	125	702	175	1.28	0.25
39	127	700	75	0.97	0.37
40	125	692	176	1.24	0.34
41	125	755	75	1.19	0.35
42	130	653	173	1.45	0.35
43	134	609	75	0.89	0.50
44	127	671	175	1.11	0.46
45	131	518	75	1.17	0.51
46	126	691	175	1.33	0.45
47	237	693	173	1.18	0.06
48	240	607	74	1.44	0.25
49	223	721	175	1.13	0.25
50	229	681	75	1.48	0.24
51	225	718	175	1.14	0.26
52	225	753	75	1.02	0.35
53	222	708	175	1.22	0.34
54	219	820	75	1.15	0.34
55	227	683	175	1.34	0.35
56	223	588	75	1.40	0.45
57	229	686	175	1.06	0.46
58	221	627	75	1.48	0.46
59	227	712	175	1.23	0.46
60	101	193	100	1.12	0.44
61	49	241	49	0.98	0.30
62	125	507	125	1.20	0.25
63	93	705	101	1.12	0.32
64	99	649	100	1.02	0.45
65	150	411	150	1.11	0.35
66	153	377	149	1.23	0.45
67	199	984	201	1.25	0.36
68	199	956	200	1.32	0.46
69	251	800	250	1.31	0.36
70	249	834	250	1.40	0.44
71	51	196	149	1.34	0.20
72	99	212	100	0.93	0.30
73	137	201	50	1.03	0.01
74	149	206	200	1.03	0.10
75	207	179	199	1.05	0.53
76	248	204	250	1.54	0.40

77	46	517	51	1.08	0.37
78	102	364	100	1.03	0.51
79	147	409	151	0.97	0.10
80	148	418	200	1.10	0.00
81	199	400	200	1.46	0.20
82	247	409	251	1.44	0.30
83	50	597	199	1.06	0.30
84	99	607	251	1.33	0.00
85	154	462	100	1.07	0.53
86	153	617	50	1.11	0.10
87	200	595	150	1.16	0.20
88	255	576	149	1.53	0.40
89	51	802	198	1.14	0.11
90	102	665	50	1.31	0.30
91	160	782	100	1.11	0.01
92	150	804	250	1.48	0.19
93	200	824	150	1.18	0.50
94	258	752	199	1.33	0.42
95	50	1055	199	1.14	0.10
96	119	723	49	0.81	0.39
97	152	1031	100	0.95	0.20
98	156	993	149	1.14	0.01
99	202	982	250	1.46	0.41
100	257	994	199	1.47	0.49